UNIVERSITY OF CALIFORNIA
Santa Barbara

Understanding Relationships Between Morphology and Charge Transfer States in Organic Photovoltaics

A Dissertation submitted in partial satisfaction
of the requirements for the degree of

Doctor of Philosophy

in

Materials

by

Christopher D. Liman

Committee in Charge:

Professor Michael Chabinyc, Chair

Professor Craig Hawker

Professor Glenn Fredrickson

Professor Chris Van de Walle

September 2014

The Dissertation of
Christopher D. Liman is approved:

Professor Craig Hawker

Professor Glenn Fredrickson

Professor Chris Van de Walle

Professor Michael Chabinyc, Committee Chair

July 2014

Understanding Relationships Between Morphology and Charge Transfer States in Organic Photovoltaics

by

Christopher D. Liman

Acknowledgements

I would like to thank my family and friends for their constant support, and especially my parents. Also I would like to thank my advisor Prof. Michael Chabinyc for the wonderful academic guidance, as well as Profs. Craig Hawker, Glenn Fredrickson, Chris Van de Walle, Edward Kramer, and Fred Wudl. I would like to thank everyone in the Chabinyc group for valuable support, feedback, and discussions, and the administrative and technical staff of the Materials department, CNSI and MRL.

Also I would like to acknowledge the Mitsubishi Chemicals Center for Advanced Materials and the DoD Defense Threat Reduction Agency for funding. Additionally I acknowledge the use of several facilities: the MRL Central Facilities, a member of the NSF-funded Materials Research Facilities Network which is supported by the MRSEC Program of the NSF under Award DMR-1121053; the Stanford Synchrotron Radiation Lightsource, a national user facility operated by Stanford University on behalf of the U.S. Department of Energy, Office of Science, Office of Basic Energy Sciences under Contract No. DE-AC02-76SF00515; and the Advanced Light Source which is supported by the Director, Office of Science, Office of Basic Energy Sciences, of the U.S. Department of Energy under Contract No. DE-AC02-05CH11231. I would like to thank the authors of the following software – for analyzing GIWAXS data: Stefan Mannsfeld (SSRL) and R, Joseph Kline (NIST); GIWAXS simulation software: Dag W. Breiby; and GISAXS analysis software: Jan Ilavsky.

Some chapters are based on the following papers and work done by the following co-authors, whom I would like to thank for their guidance and collaboration.

- **C. D. Liman**, S. Choi, D. W. Breiby, J. E. Cochran, M. F. Toney, E. J. Kramer, M. L. Chabinyc, "2-D GIWAXS Reveals Transient Crystal Phase in Solution-Processed Thermally Converted Tetrabenzoporphyrin", *Journal of Physical Chemistry B* **2013**, *117*, 14557-14567.
- X. Wang, **C. D. Liman**, N. D. Treat, M. L. Chabinyc, D. G. Cahill, "Ultralow thermal conductivity of fullerene derivatives", *Physical Review B* **2013**, *88*, 075310.
- S.-H. Choi, **C. D. Liman**, S. Krämer, M. L. Chabinyc, E. J. Kramer, "Crystalline polymorphs of [6,6]-phenyl-C61-butyric acid n-butyl ester (PCBNB)", *Journal of Physical Chemistry B* **2012**, *116*, 13568-13574.
- S.-Y. Ku*, **C. D. Liman*** (*co-first authors), J. E. Cochran, M. F. Toney, M. L. Chabinyc, C. J. Hawker, "Solution-processed nanostructured benzoporphyrin with polycarbonate binder for photovoltaics", *Advanced Materials* **2011**, *23*, 2289-93.
- S.-Y. Ku, **C. D. Liman**, D. J. Burke, N. D. Treat, J. E. Cochran, E. Amir, L. A. Perez, M. L. Chabinyc, C. J. Hawker, "A Facile Synthesis of Low-Band-Gap Donor-Acceptor Copolymers Based on Dithieno-[3,2-b:2',3'-d]-thiophene", *Macromolecules* **2011**, *44*, 9533-9538.
- **C. D. Liman**, S. Bubel, M. L. Chabinyc, "UV-induced ionic photoconductivity in ZnO photodiodes and transistors".
- **C. D. Liman**, N. Eisenmenger, R. Harris, M. L. Chabinyc, "Controlling interface and charge transfer states in small molecule organic solar cells with pure domains".

Curriculum Vitæ

Christopher D. Liman

Education

2009-2014	Doctor of Philosophy in Materials, University of California, Santa Barbara.
2005-2009	Bachelor of Science in Materials Science and Engineering, Northwestern University.

Experience

2009-2014	Graduate Student Researcher, University of California, Santa Barbara, Professor Michael Chabinyc.
2007-2019	Undergraduate Research Assistant and REU Participant, Northwestern University, Professor Mark Hersam.
2008	Engineering Intern, Caterpillar Inc. Advanced Materials Technology Group, Aurora, IL.

Publications

- **C. D. Liman**, S. Choi, D. W. Breiby, J. E. Cochran, M. F. Toney, E. J. Kramer, M. L. Chabinyc, "2-D GIWAXS Reveals Transient Crystal Phase in Solution-Processed Thermally Converted Tetrabenzoporphyrin", *Journal of Physical Chemistry B* **2013**, *117*, 14557-14567.
- X. Wang, **C. D. Liman**, N. D. Treat, M. L. Chabinyc, D. G. Cahill, "Ultralow thermal conductivity of fullerene derivatives", *Physical Review B* **2013**, *88*, 075310.
- S.-H. Choi, **C. D. Liman**, S. Krämer, M. L. Chabinyc, E. J. Kramer, "Crystalline polymorphs of [6,6]-phenyl-C61-butyric acid n-butyl ester (PCBNB)", *Journal of Physical Chemistry B* **2012**, *116*, 13568-13574.
- S.-Y. Ku*, **C. D. Liman*** (*co-first authors), J. E. Cochran, M. F. Toney, M. L. Chabinyc, C. J. Hawker, "Solution-processed nanostructured benzoporphyrin with polycarbonate binder for photovoltaics", *Advanced Materials* **2011**, *23*, 2289-93.
- S.-Y. Ku, **C. D. Liman**, D. J. Burke, N. D. Treat, J. E. Cochran, E. Amir, L. A. Perez, M. L. Chabinyc, C. J. Hawker, "A Facile Synthesis of Low-Band-Gap Donor-Acceptor Copolymers Based on Dithieno-[3,2-b:2',3'-d]-thiophene", *Macromolecules* **2011**, *44*, 9533-9538.

In Preparation

- **C. D. Liman**, S. Bubel, M. L. Chabinyc, "UV-induced ionic photoconductivity in ZnO photodiodes and transistors".
- **C. D. Liman**, N. Eisenmenger, R. Harris, M. L. Chabinyc, "Controlling interface and charge transfer states in small molecule organic solar cells with pure domains".

Patents

- C. J. Hawker, M. L. Chabinyc, S.-Y. Ku, **C. D. Liman**, S. Aramaki, H. Wang, T. Niinomi, US 2012/0168728 A1: Organic Electronic Devices Prepared Using Decomposable Polymer Additives, **2012**.

Awards and Honors

2012 US-Taiwan Global School for Advanced Studies: Best Proposal Award

2012-2013 UCSB MRL-Dow Chemical Travel Fellowship (2x)

2011 NSF Graduate Research Fellowship Program: Honorable Mention

2009 Cum Laude, Ford Dean Scholars, Dean's List

2005 National Merit Scholarhip

Oral Presentations

2014 "Controlling Interface and Charge Transfer States in Small Molecule Organic Solar Cells with Pure Domains", Electronic Materials Conference, Santa Barbara, CA.

2013 "Probing Interfacial Regions Using Charge Transfer States", Next-Generation Organic Photovoltaics, Groningen, Netherlands.

2013 "Examining charge transfer states in organic solar cells with controlled interfacial area", Materials Research Society Spring Meeting, San Francisco, CA.

2012 "Donor-acceptor-acceptor block copolymers: toward high efficiency solar cells", Global School for Advanced Studies Session on Organic Solar Cells, Taipei, Taiwan.

Poster Presentations

2014 "UV-Induced Ionic Photoconductivity in a-ZnO for Low-Power Light Sensing", Materials Research Society Spring Meeting, San Francisco, CA.

2013 "ZnO Photodoping in Hybrid UV Photodetectors", Defense Threat Reduction Agency Basic Research Technical Review, Springfield, VA.

2012 "Low-Cost Inverted Structure Organic/ZnO Ultraviolet Photodetectors", Materials Research Society Fall Meeting, Boston, MA.

2012 "Top illuminated organic UV photodetectors", Global School for Advanced Studies Session on Organic Solar Cells, Taipei, Taiwan.

2011 "Kinetic behavior of thin film crystallization in solution-processed thermally converted small molecule OPVs", Materials Research Society Spring Meeting, San Francisco, CA.

2010 "In situ annealing of benzoporphyrin and fullerene films with 2D GIWAXS", Organic and Hybrid Electronics Workshop, Santa Barbara, CA.

Teaching and Outreach

2010 Teaching Assistant, Introduction to the Structures and Properties of Materials

2011- Mentored three undergraduate interns and a master's student on research projects in lab

2013- Scienceline: answered science questions by K-12 students and teachers

2011- Participated in outreach events for K-12 science education

Abstract

Understanding Relationships Between Morphology and Charge Transfer States in Organic Photovoltaics

Christopher D. Liman

Renewable energy sources are becoming increasingly important as the world's energy demands continue to grow and climate change continues to occur. Photovoltaic power generation has great potential, but most commercial photovoltaic cells have typically been made from single-crystal or polycrystalline silicon which are expensive and energy intensive to produce. Organic semiconductors are one class of solar cell materials that have the potential for low cost due to solution processability, roll-to-roll fabrication, material tunability, and the very small amounts of material required to absorb light compared to crystalline silicon. Organic photovoltaic (OPV) efficiencies have increased rapidly in the past few years and are currently at about 11% power conversion efficiency.

To find new pathways to improve OPV performance, a deeper understanding of the relationships between morphology, electronic properties, and OPV performance is required. This work will explore these relationships, focusing on the relationship between morphology and charge transfer states. We focus on a small molecule material system with only pure donor and acceptor domains, unlike the typical bulk heterojunction composed of donor, acceptor, and mixed domains. The advantage of studying this system

is a more well-defined interfacial area and simpler morphology that allows us to better characterize charge transfer states at the donor-acceptor interface.

We first review the basic principles of OPV operation, fabrication and characterization methods, and charge transfer states. We then use grazing incidence wide angle X-ray scattering to characterize the crystal structures and textures of the polymorphs of the donor and acceptor in our small molecule system, which are important for understanding their blend morphology. Next, we demonstrate a new method to control morphology in this system with the use of a thermally degradable binder polymer. Afterwards, we vary interfacial area and charge transfer state density in this system through processing and characterize it using sub-bandgap external quantum efficiency measurements, allowing us to gain valuable insights about the photophysics of this system.

Finally, many of the insights and techniques used to study this system are also useful in studying other systems of organic or solution-procesed semiconductors. We optimize the morphology and performance of OPVs made with novel low-bandgap donor-acceptor copolymers. We then find that ionic photoconductivity plays an important role in the behavior of photodetectors made with solution processed amorphous ZnO and in their interaction with organic semiconductors.

Contents

List of Figures

List of Tables

Chapter 1

Introduction

1.1 Motivation and Big Questions

Renewable energy sources are becoming increasingly important as the world's energy demands continue to grow and climate change continues to occur. The raw power output of the sun is easily enough to meet humanity's needs for the forseeable future, however the main challenge lies in the cost-effective collection and distribution of this power. Unlike fossil fuels, solar power requires large areas of photovoltaic cells or mirrors in the case of solar concentrators. These cells have typically been made from single-crystal or polycrystalline silicon[1] and are expensive and energy intensive to produce. Gallium arsenide-based multijunction cells are more efficient but much more costly, and often used in concentrator or space applications. To decrease the cost of solar power, other classes of materials for use in solar cells have been investigated. Organic semiconductors are one such class of materials, which hold the promise of low cost cell fabrication due

to solution processability, roll-to-roll fabrication, material tunability, and the very small amounts of material required to absorb light compared to crystalline silicon.

Power conversion efficiencies of organic photovoltaics (OPVs) have increased rapidly in the past few years and are currently at about 11% power conversion efficiency (Fig. 1.1). The obstacles currently preventing OPVs from being commercially used on a wide scale are primarily low efficiencies and device lifetimes compared to inorganic crystalline technologies.[2–4] However, OPV efficiencies do not necessarily need to match those of inorganics because of the lower cost of OPVs. A wide variety of OPV materials can be synthesized to vary solubility, band gap, energy levels, and other properties. Furthermore, OPVs can be mechanically flexible and have potential for use in smaller scale applications such as consumer electronics. The photophysics of organic semiconductors (e.g. energy states, recombination losses, dynamics, etc.) are not understood as well as inorganic semiconductors.[2–4] To find new pathways to improve OPV performance, a deeper understanding of the relationships between morphology, electronic properties, and performance is required. This work will explore these relationships, focusing on the relationship between morphology and charge transfer states.

Charge transfer (CT) states are excitons composed of a hole on a donor and an electron on a neighboring acceptor, coulombically bound and sharing a wavefunction. CT state densities are proportional to the donor-acceptor interfacial area. Probing CT states is an effective way of non-destructively determining important morphological and elec-

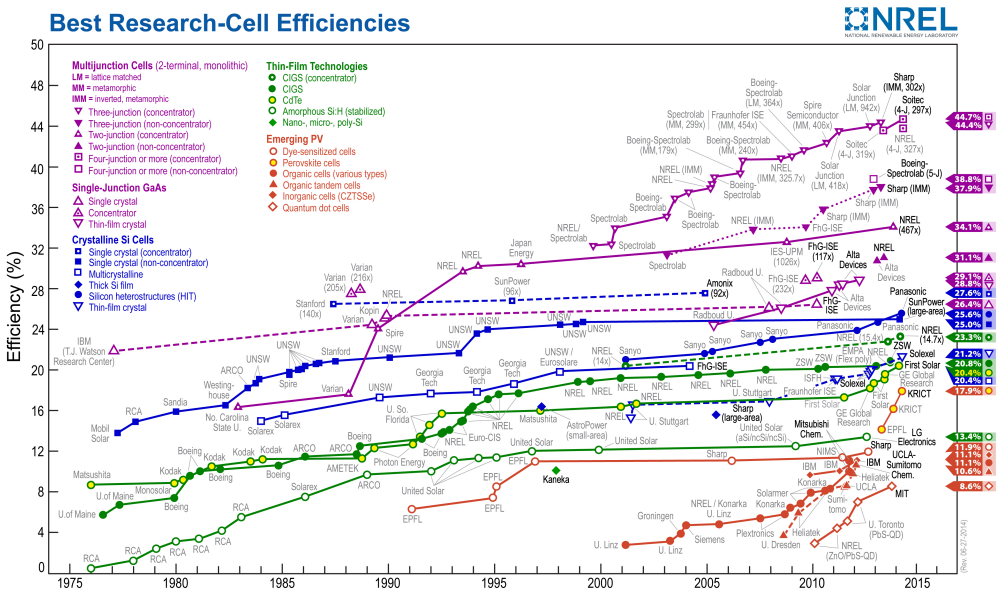

Figure 1.1: History of power conversion efficiencies of different types of solar cells.[5]

tronic properties. In this work we focus on a material system with only pure donor and acceptor domains, unlike the typical bulk heterojunction composed of donor, acceptor, and mixed domains. The advantage of studying this system is a more well-defined interfacial area and simpler morphology that allows us to better characterize CT states.

In the rest of this chapter, we review the basic principles of OPV operation, fabrication and characterization methods, and charge transfer states. In the next chapter, we characterize the crystal structures and textures of the polymorphs of the donor and acceptor in our small molecule system, which are important for understanding their blend morphology. In the following chapter, we discuss one method to control morphology in this system with the use of a binder polymer. In the chapter afterwards, we link morphol-

ogy and charge transfer states using sub-bandgap external quantum efficiency (EQE) measurements. Finally, in the last chapter, we discuss other projects related to the characterization of solution-processed electronic devices. Many of the relationships between structure, properties, and performance found in organic photovoltaics are also useful in studying organic semiconductors for other applications, as well as solution-processed photovoltaics and other electronic devices in general.

1.2 Operating Principles of Organic Photovoltaics

There are some major differences between organic and inorganic semiconductors that must be kept in mind in order to understand the behavior of OPVs. Inorganic semiconductors tend to be very crystalline with few defects, while most organics are disordered. There is weaker electronic coupling in organics, occuring mostly through π-π bonds, and electronic states are less delocalized. Therefore, instead of electronic bands, the electronic structure is represented by molecular orbitals, with the highest occupied molecular orbital (HOMO) and lowest occupied molecular orbital (LUMO) defining the band gap.

Excitons are bound pairs of an electron and a hole, coulombically attracted to each other and sharing a wavefunction.[6] In organic semiconductors, which have smaller dielectric constants than inorganic semiconductors, the distance between the electron and hole (the exciton Bohr radius) is quite small, a few angstroms, while in inorganics this dis-

tance can be a few nanometers. Due to weak electronic coupling, strong electron-phonon coupling, and a high amount of disorder and trap states, intermolecular charge transport typically occurs through hopping transport instead of band transport in inorganics. The exciton binding energy is also much higher, on the order of 0.5 eV for organics compared to around 0.01 eV for inorganics. This means that excitons will not spontaneously diffuse apart. In order to extract charges effectively from an OPV, both a donor that transports holes and an acceptor that transports electrons is required. Typically the donor and acceptor are deposited in a mixture, forming a bulk heterojunction (BHJ) with a large amount of donor-acceptor interfacial area. The excitons migrate to the heterojunction and dissociate due to the difference in HOMO or LUMO energy levels between the donor and acceptor, which needs to be at least on the order of 0.3 eV.[7]

A typical OPV is composed of a high work function anode and a low work function cathode, and an active layer sandwiched between them (Fig. 1.2). Light is absorbed in the active layer, which is typically a BHJ composed of a donor and an acceptor. At least one of the electrodes must be transparent so that light can reach the active layer, and typically a transparent conducting oxide such as indium tin oxide (ITO) is used for the bottom electrode. Other layers may be included between the electrodes and active layer for various purposes: to block one type of charge carrier and facilitate collection of the other type and reduce leakage current, or to modify the work function or surface energy

of one of the electrodes. One very common interfacial layer is a PEDOT:PSS (poly(3,4-ethylenedioxythiophene)-poly(styrenesulfonate)) hole transporting layer.

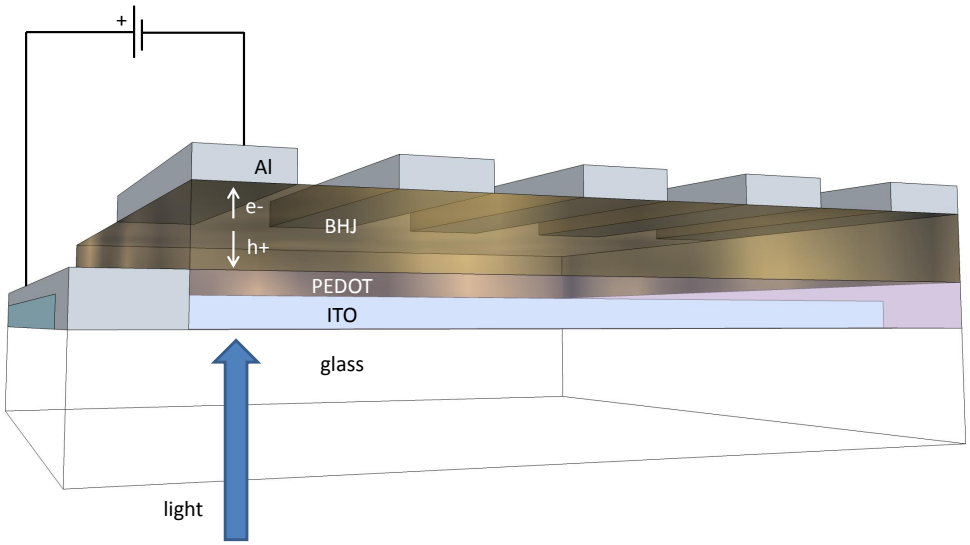

Figure 1.2: Schematic of the layers in a typical organic solar cell.

The first OPVs were composed of a single material active layer, and had very low efficiencies due to this lack of exciton separation.[8,9] In 1986 Tang et al. introduced the first bilayer heterojunction solar cell, with a 1 % power conversion efficiency.[10] Bilayer OPVs still had low efficiencies because of the short exciton diffusion lengths of about 5-20 nm in organic semiconductors. Only excitons generated within this diffusion length from a donor-acceptor interface have a good chance of diffusing to an interface before recombining. Bulk heterojunction solar cells with phase separation on the order of the exciton diffusion length proved to be much more efficient than bilayers, as the interfacial

area is much increased allowing for thicker active layers that absorb a greater fraction of sunlight while allowing for excitons to still diffuse to an interface.

The choice of donor and acceptor materials is an important factor in determining device efficiency, and throughout the years researchers have tried to synthesize more efficient materials. Early on, typically used donor polymers included MEH-PPV and MDMO-PPV. Later, the OPV community settled on poly(3-hexyl thiophene) (P3HT) as the standard donor of choice. Fullerene derivatives have been by far the most common acceptor of choice, namely [6,6]-phenyl-C_{61}-butyric acid methyl ester (PCBM) and later on the stronger absorber PC71BM. Fullerene derivatives are likely effective acceptors because of their deep HOMO and LUMO levels, high degree of conjugation, and ability to form good morphologies when mixed with polymers. The "baseline" system, P3HT:PCBM, can achieve up to 5 % power conversion efficiencies. Much of the work on finding a more efficient system has focused on the synthesis of new low bandgap donor polymers which can absorb more light than P3HT.[11] There has also been work on small molecule donors,[12] such as porphyrins and phthalocyanines that have strong and broad absorbance, including the one that this work focuses on, benzoporphyrin (BP). The choice of either a polymer or a small molecule donor has its advantages and disadvantages. Small molecules are more readily purified, have a well-defined molecular weight, and have the potential to form thin films with a high degree of crystallinity and order.[13] Polymers have a higher degree of conjugation and greater mechanical robustness. Com-

paratively less work has been done on non-fullerene acceptors, which tend to have lower efficiencies.

In a typical OPV, there are four main steps that need to occur for charges to be successfully collected, namely absorption, exciton migration, charge separation, and charge collection (Fig. 1.3). The first step that occurs when light hits a solar cell is absorption, generating a singlet exciton. Photons may be absorbed by the active layer(s), known as active absorption, or by the other layers in the device, known as parasitic absorption, or be scattered or reflected. Only the fraction of photons absorbed by the active layer η_{Abs} have a chance of being converted to electric current. The active absorption is dependent on the optical band gaps of the donor and acceptor, as well as the extinction coefficient as a function of wavelength, the active layer thickness, and optical interference effects. Tailoring the band gaps of the donor and acceptor so that the materials absorb at complementary wavelength ranges and so that their sum absorbs over a broad range will improve the absorption of the active layer.

The second step following absorption is exciton migration to a donor-acceptor interface, primarily through Förster resonance energy transfer. This requires the dipole orientations of the emitting and absorbing chromophores to be aligned, for them to have spectral overlap, and for them to be within 3-10 nm of each other. The fraction of excitons generated in the donor and acceptor that diffuse to an interface η_{EM} depends on the exciton diffusion length L_D in these materials, which ranges from about 5-20 nm and

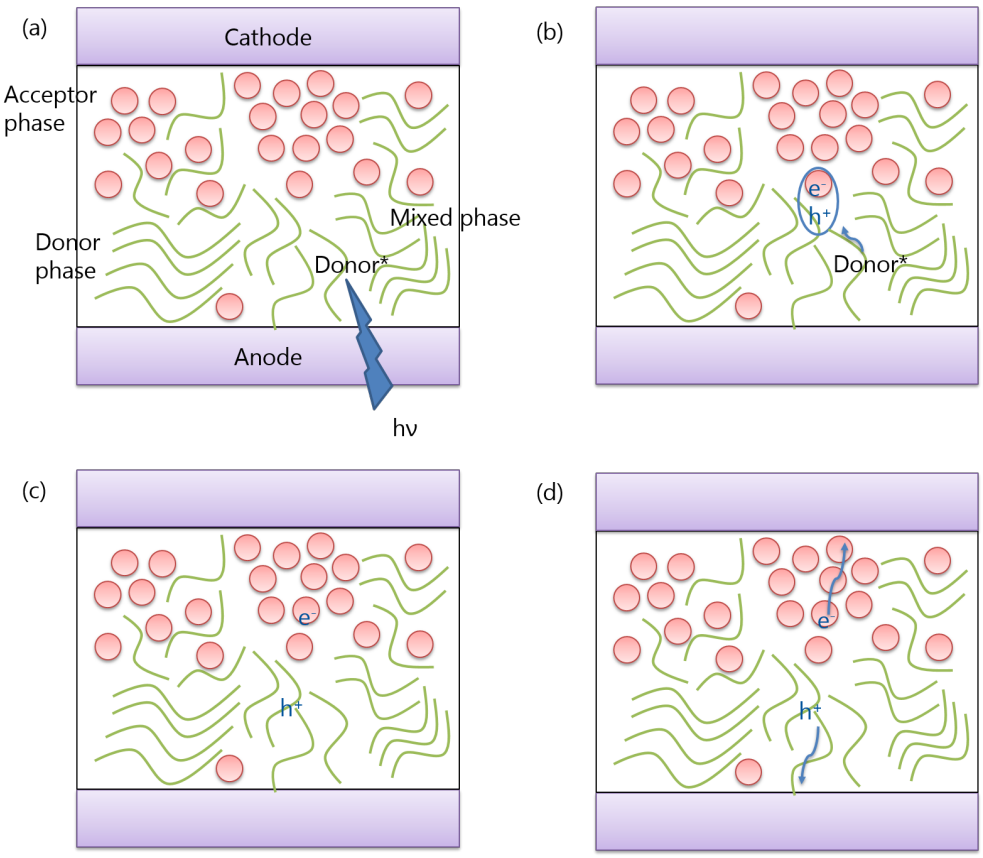

Figure 1.3: Absorption, exciton migration, charge separation, and charge collection in a BHJ solar cell.

depends on the diffusion coefficient of the excitons and the average exciton lifetime.[14] If the domain size of the donor or the acceptor is larger than L_D, many of the excitons will decay before they are able to randomly diffuse to an interface. Therefore a bilayer device architecture results in poor exciton diffusion while the best morphology in terms of exciton diffusion is a completely mixed BHJ with very small domains.

One way to measure η_{EM} is photoluminescence (PL) quenching. This typically involves comparing the PL of various thickness layers of polymer to the PL of the same thicknesses of polymer on top of a fullerene derivative which is a strong quencher (assume $\eta_{CS} = 1$). For a perfect bilayer the L_D of the polymer can be obtained by fitting the diffusion equation with the PL quenching data.[15,16] Once the L_D is known it can be used to predict the EQE of a bilayer solar cell of varying polymer thicknesses. PL quenching can also be used to simply measure the exciton harvesting efficiency $\eta_{EH} = \eta_{EM}\eta_{CS}$ in a BHJ. However, there are difficulties in measuring the PL of PCBM because its emission is weak and its emission spectrum overlaps that of P3HT.[17]

The third step is charge separation, which is the conversion of an exciton into a free hole in the donor and electron in the acceptor. This is often thought to be composed of two steps: charge transfer of the exciton at the interface to a bound electron-hole pair with the hole on a donor and the electron on an acceptor (i.e. a CT state), followed by dissociation into a free electron and hole. In order for charge transfer to occur efficiently at short circuit, typically the HOMO of the acceptor must be deeper than that of the donor, and the LUMO of the acceptor must be deeper than that of the donor. In general the differences should be greater than the exciton binding energy to provide a driving force for the charge transfer to occur. However, if these differences are too large it will result in a loss in open circuit voltage. Charge transfer has been shown to occur if the energy of the charge transfer state is lower than that of the exciton by at least 0.1 eV.[18] The

charge transfer state in pentacene has been measured to have a binding energy between 0.1 eV and 0.5 eV.[19]

After charge transfer occurs, the CT state may dissociate into free charges, or recombine through geminate or trap-assisted recombination. The alternative mechanism for charge separation is that of hot exciton dissociation, in which an exciton directly dissociates into a free electron and hole without first forming a CT state. Some evidence that the CT state mechanism is predominant is that in one polymer-fullerene system, CT states directly excited by sub-bandgap light convert into free charges with the same efficiency as excitons generated by above-bandgap light.[20]

Finally, the last step is charge collection (η_{CC}), which includes the movement of free holes and electrons to their respective electrodes and extraction of the charges at the electrodes. The driving forces for the movement of free charges are diffusion away from the donor-acceptor interfaces and the built in voltage and applied voltage across the device causing drift. An active layer morphology in which there are continuous pathways in both the donor and the acceptor to their respective electrodes, with few islands or dead ends, is desirable. This morphology can be difficult to achieve in conjunction with the small domain sizes necessary for efficient exciton diffusion. And although short pathways are desirable to reduce the probability of recombination, this is counter to the desire to have thicker active layers that improve absorption. Optimized BHJ morphologies can result in internal quantum efficiencies above 90%.[21] A loss mechanism in this step is

bimolecular recombination, in which holes and electrons not originating from the same exciton recombine.

To summarize, the losses in current that occur in a solar cell can be summarized in the equation:

$$\eta_{EQE}(\lambda) = \eta_{Abs}(\lambda)\eta_{IQE}(\lambda) = \eta_{Abs}(\lambda)\eta_{EM}(\lambda)\eta_{CS}(\lambda)\eta_{CC}(\lambda) \tag{1.1}$$

where each of the efficiency factors may be dependent on incident wavelength, position in the active layer, and different in the donor and the acceptor. These factors relate to the J_{sc} by the equation

$$J_{sc} = \int_{\lambda} e\Phi(\lambda)\eta_{EQE}(\lambda)\mathrm{d}\lambda \tag{1.2}$$

where $\Phi(\lambda)$ is the incident photon flux density.

To obtain a quantitative measurement of η_{Abs}, the propagation of light through the layers of the solar cell must be analyzed using a transfer matrix model.[15,16] This requires the thickness and the complex index of refraction $n + i\kappa$ of each layer individually to be measured, typically using spectroscopic ellipsometry. MATLAB and Python scripts that use the transfer matrix model to output the fraction of photons absorbed by each layer are available.[22,23] Instead of using spectroscopic ellipsometry, which can be difficult to interpret, an approximation can be made by letting n be a constant and letting $k = \frac{\lambda\alpha}{4\pi}$, where α is the extinction coefficient measured by absorption spectroscopy.[22] Typically, transfer matrix calculations do not account for diffuse scattering, which is dependent on

the roughness of each layer, or the inhomogeneity of each layer, especially blend layers.[24] Due to these inaccuracies, the calculations are used to calculate the relatively small parasitic absorption, which is subtracted from the measured total absorption to obtain the active absorption. Due to interference effects, the active absorption does not linearly increase with thickness but varies sinusoidally at low thicknesses, allowing one to calculate optimal absorption thicknesses without making many devices.

1.3 Device Parameters and Fabrication and Testing Methods

OPV fabrication typically starts with a glass substrate onto which a transparent bottom electrode is applied, most commonly ITO coated through RF sputtering. After substrate cleaning, the hole transporting layer, which is typically PEDOT:PSS, is spin coated in an aqueous dispersion onto the glass/ITO. The active layer or layers is applied, typically by depositing a solution of the dissolved donor and acceptor in a chlorinated solvent such as chlorobenzene. For laboratory-scale experiments, this solution is most commonly spin coated but can also be blade coated or simply drop cast. The active layer can also be thermally evaporated, although this loses the advantages of solution processability. Techniques to improve the morphology of the active layer are commonly used, including the use of solvent additives, thermal annealing, solvent annealing or slow drying. Finally,

thermal evaporation is used to apply the metal top electrode (Fig. 1.2). OPVs are often air sensitive and are usually fabricated and tested in a nitrogen glovebox.

The finished solar cells are tested under a solar simulator, a filered xenon lamp that attempts to simulate the AM 1.5 solar spectrum. The current density as a function of applied bias is measured, and from this the short circuit current J_{sc}, open circuit voltage V_{oc}, fill factor FF, and power conversion efficiency (PCE) are obtained. This measurement is repeated in the dark. Fig. 1.4 shows typical light and dark curves of an OPV, and the approximate band diagram at J_{sc}, V_{oc}, and above V_{oc}.

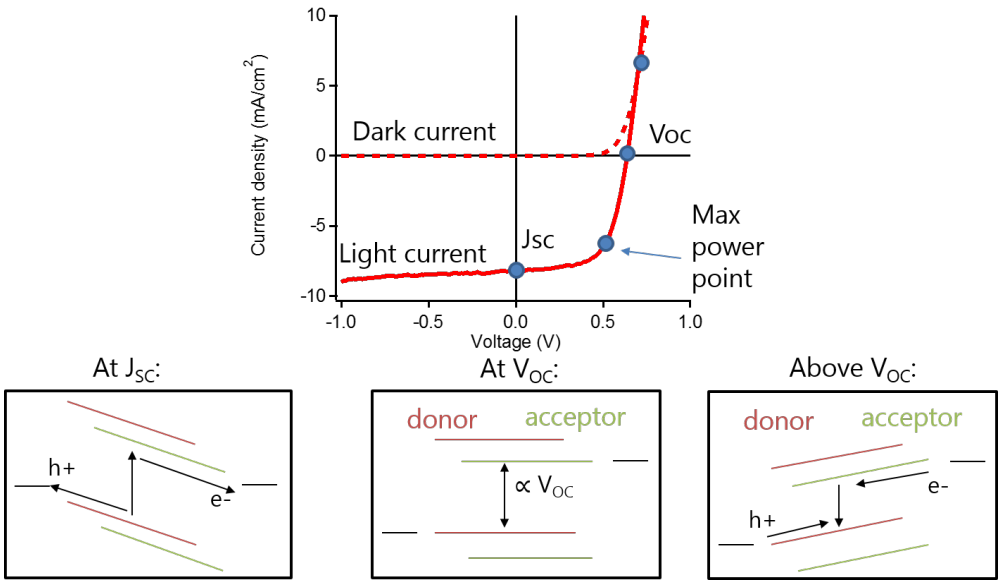

Figure 1.4: Typical current density-voltage curve of a BHJ organic solar cell and the band diagram at various applied biases.

J_{sc} is the current density at zero applied bias. This is mainly dependent on the amount of light absorbed by the active layer, but also on the efficiency of exciton migration and recombination losses at the built-in potential. V_{oc} is the bias at which zero current is collected from the solar cell. At this voltage, the applied bias cancels the built-in potential and the energy bands are flat. V_{oc} tends to be proportional to the difference between the HOMO of the donor and the LUMO of the acceptor, with losses attributed to, among other things, band bending and diffusion of charges from the electrodes into the active layer. Above V_{oc} the device acts as a diode in the "on" condition and charges are injected into the active layer. PCE, the power extracted from the device divided by the incident power, is determined by the following equation containing the preceding factors:

$$PCE = \frac{P_{out}}{P_{in}} = \frac{V_{oc} J_{sc} FF}{P_{in}} \tag{1.3}$$

The shape of the current density-voltage curve is often modeled using the following equivalent circuit (Fig. 1.5) and diode equation (Eq. (1.4)), including a series resistance R_{se} and a shunt resistance R_{sh}. R_{se} can be approximately determined from the slope of the dark J-V curve at biases greater than V_{oc}, and a low R_{se} is desirable. R_{se} is a measure of charge injection and transport in forward bias, and the resistive losses of the interfaces and electrodes. R_{sh} can be approximately determined from the slope of the dark J-V curve at large reverse biases, and a high R_{sh} is desirable. R_{sh} is a measure of the current leakage in reverse bias.

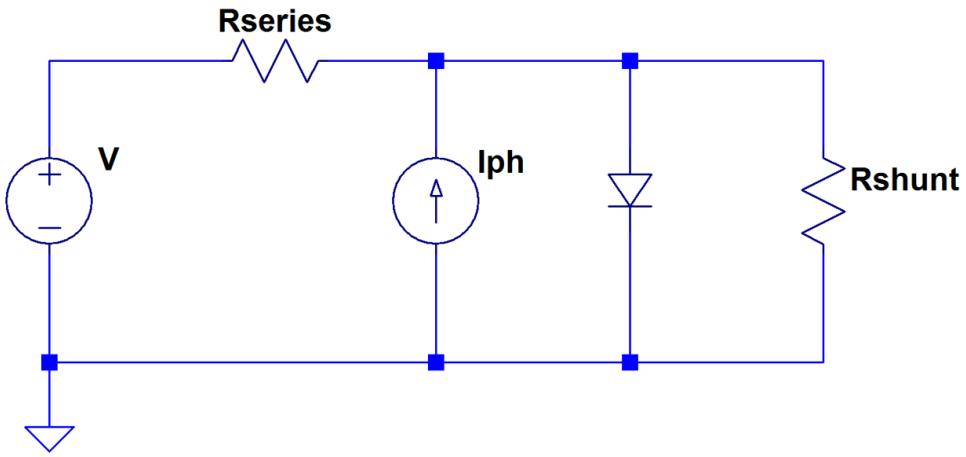

Figure 1.5: Equivalent circuit for solar cell.

$$J_d(V) = J_0 \left[\exp\left(\frac{q(V - J_d(V)R_{se})}{nkT} \right) - 1 \right] + \frac{V}{R_{sh}} \tag{1.4}$$

The external quantum efficiency (EQE) and internal quantum efficiency as a function of incident wavelength are two more important parameters in an OPV. EQE measures the number of charges collected from the solar cell divided by the number of incident photons, while IQE uses the number of absorbed photons instead.

$$EQE = \frac{N_e}{N_v^{\text{incident}}} \tag{1.5}$$

$$IQE = \frac{N_e}{N_v^{\text{absorbed}}} \tag{1.6}$$

In an EQE measurement, monochromatic light is incident on the sample while current is measured. This current is converted to a fraction using the known photon flux for each

incident wavelength. A lock-in setup is often used to measure low EQE and minimize noise, especially for sub-bandgap EQE which can be several orders of magnitude weaker than above-bandgap EQE (Fig. 1.6). Above-bandgap EQE gives information about the absorption bands of the donor and acceptor and how effectively the excitons generated in both materials are converted to CT states and free charges. Sub-bandgap EQE gives information about the presence, number, and energies of CT states. Finally, IQE is typically obtained by dividing the EQE by the fraction of incident light absorbed by the device, from UV-vis reflectance. Sometimes a more accurate IQE is calculated based on the light absorbed by the active layer and not the whole device, by using a transfer matrix calculation to find the parasitic absorbance. The IQE in efficient solar cells tends to vary only a small amount with wavelength.

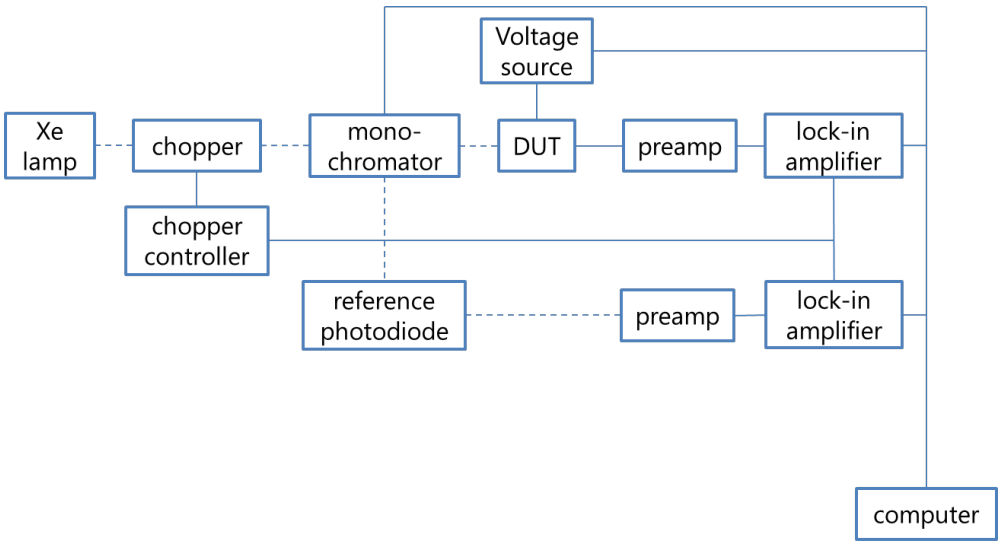

Figure 1.6: Typical lock-in setup for measuring external quantum efficiency.

The hole and electron mobilities of organic semiconductors are often measured using TFT mobility, time-of-flight mobiity, or Hall effect mobility. UV-vis absorption spectroscopy gives us the optical bandgap and absorption spectrum of the film, while photoluminescence gives us information about radiative recombination. Ultraviolet photoelectron spectroscopy can be used to find the HOMO energy level of the film, and combining this with absorption spectroscopy gives us the LUMO. Cyclic voltammetry is also used to find the HOMO and LUMO of organic semiconductors.

There are a wide range of physical characterization methods commonly used to characterize OPV materials, either with the donor and acceptor blended or studied separately. X-ray scattering can reveal important information on morphology, but the low thickness and high degree of disorder in organic thin films means that standard sources are not intense enough to offer , and synchrotron X-ray sources are typically used instead. Grazing incidence wide-angle X-ray scattering (GIWAXS) is useful for probing shorter length scale information such as crystal structure and texture (degree to which crystallites are oriented in the same direction relative to the substrate), while grazing incidence small-angle X-ray scattering (GISAXS) can probe longer length scale information. Atomic force microscopy and profilometry directly probe the surface of the film, and scanning and transmission electron microscopy are useful for both probing morphology and in-plane crystallinity.

Chapter 2

Characterization of Polymorphs of Molecular OPV Materials

2.1 Benzoporphyrin

Thermally convertible organic materials are useful for the fabrication of multilayer thin film electronic devices such as solar cells. However, substantial changes in molecular ordering can occur during the conversion process that may lead to multiple polymorphs having differing electronic properties. In-situ grazing incidence wide angle X-ray scattering with two-dimensional detection (2-D GIWAXS) was used to study the changes in the thin film crystal structure, texture, and crystallite size of a convertible small molecule electron donor, tetrabenzoporphyrin (BP), during thermal conversion from the precursor bicycloporphyrin (CP), and the resulting crystal-crystal phase transition from a metastable phase (phase I) to a stable phase (phase II). The annealing temperature and the presence of an underlying BP layer both affect the phase transition behavior. Phase II has a much

weaker degree of crystalline texture than phase I, attributed to changes in molecular packing to achieve a herringbone arrangement. The unit cell for phase I was determined by electron diffraction and GIWAXS, and the thin film structure of phase II matched the previously determined bulk structure. The texture of crystallites in phase II was characterized by simulation of the GIWAXS pattern. Transmission electron microscopy revealed differences in the morphology, grain size, and film coverage of the two polymorphs. Peak shape analysis with corrections for geometric smearing and paracrystalline disorder showed an increase in crystallite size from phase I to phase II. These results demonstrate the utility of in-situ 2-D GIWAXS in revealing polymorphic phases during the structural transition of thermally convertible organic semiconductors, the presence of which may impact the performance of solar cells.

2.1.1 Introduction

Solution processed semiconducting small molecules are a promising class of material for low cost organic electronics such as solar cells[12,13,25,26] and thin film transistors.[27–29] Recently, organic solar cells have achieved power conversion efficiencies of 10.0% and external quantum efficiencies near 100%.[30] Compared to polymers, small molecules can be more readily purified, have a well-defined molecular weight, and have the potential to form thin films with a high degree of crystallinity and order.[13] Improved structural ordering has potential benefits in photovoltaic cells including higher charge carrier mobility,

increased exciton diffusion length, and higher open circuit voltage due to a reduction in band tail width. There are also potential drawbacks of improved ordering in bulk heterojunction solar cells, such as increased phase separation and grain boundaries that may act as barriers to charge transport.[31] To better understand the changes in ordering and phase formation that can occur in these materials, we have studied a thermally convertible small molecule with two polymorphs.

Non-convertible porphyrins and phthalocyanines have been used in a wide range of heterojunction and dye-sensitized solar cells due to their high optical density and broad spectral absorbance.[32] For example, CuPc was used in one of the first organic solar cells.[10] In the bulk of the literature these materials are deposited from vapor[33] but more recently they have been explored as solution processable materials.[34,35] Solution processed small molecules that are thermally or photochemically convertible are of particular interest because the converted molecule tends to be insoluble, allowing for easily processed multilayer devices.[36] Also, solubilizing groups that allow for solution processability may disrupt the $\pi - \pi$ stacking within and between molecules, diminishing device performance. Convertible molecules lose these solubilizing groups upon conversion. Examples of these molecules include thermally or photochemically convertible pentacene precursors,[37,38] oligothiophene derivatives,[39] and precursors of porphyrins and phthalocyanines.[40–48] These types of convertible molecules have so far been primarily tested in organic thin film transistors but not in solar cells.

Here we examine an insoluble semiconducting small molecule, tetrabenzoporphyrin (BP), which is thermally converted from the soluble precursor bicycloporphyrin (CP).[49,50] We describe a detailed study of the thermal conversion of thin films of CP to BP and the crystal-crystal phase transition between the metastable phase I and stable phase II of BP. In-situ 2-D grazing incidence wide angle X-ray scattering (GIWAXS) is used to study the changes in the ordering of the films during the conversion process. This data is supplemented by transmission electron microscopy (TEM) and optical absorption spectroscopy to characterize the films.

A range of morphology characterization techniques are available to characterize organic semiconductor films.[51] In-situ X-ray scattering has been used extensively to study the evolution of crystalline ordering in organic semiconductors during deposition or thermal phase transitions. In-situ studies of the growth of thin films from vapor have been reported on pentacene,[52–55] copper phthalocyanines,[56,57] diindenoperylene,[58,59] and other materials.[60,61] These studies have revealed changes in growth modes between the initial monolayers and thicker films using specular scattering at growth rates of about 0.1 to 1 monolayers per minute. Grazing incidence scattering has also been used to study in-plane crystalline ordering during growth.[56,58] Thermal transitions of films have also been examined in real time. For example, in one work a point detector was used to study the changes in the in-plane peaks of hexabenzocoronene during the crystalline to liquid-crystalline phase transition.[62] An important consideration for in-situ experiments is the

time scale of the measurement relative to the physical process studied. In vapor growth studies, it is possible to control the deposition rate precisely, enabling in-situ scattering experiments using point detectors. For studies of processes with faster kinetics, an alternative method is required.

In-situ GIWAXS with a 2-D area detector is particularly helpful for studying processes with fast kinetics because it allows observation of a large portion of reciprocal space simultaneously. For example, the study of solution processed films is challenging due to the relatively rapid (e.g. about 1 minute) drying kinetics during casting. The nucleation and growth of TIPS-pentacene during drop casting[63] or blade coating[64] have recently been studied with in-situ 2-D GIWAXS. The formation of bulk heterojunction solar cells during and shortly after casting have recently been studied as well.[65,66] Finally, changes in morphology during the thermal processing of complex layers used in solar cells such as blends[67,68] and bilayers of P3HT:PCBM[69] have also been studied. We use this technique here to examine the CP to BP transition, which is a process in which BP is chemically formed thermally from CP and the crystal structure of the resulting BP changes dramatically during a subsequent phase transition. In this way we are able to obtain relatively complete information about the changes in the material's crystal structure, texture, and morphology during annealing.

BP has been used to make solution processed organic solar cells with a relatively high efficiency of 5.2%,[70] as well as organic thin film transistors with mobilities up to 0.07

cm^2/Vs.[71] This material has a strong peak linear attenuation coefficient[72] of $3x10^5$ cm^{-1} so thin films absorb a significant fraction of light. Furthermore, tandem devices could lead to increased efficiency by overcoming the lack of absorbance at 500-650 nm and below the band gap. The insolubility of the BP once it is annealed has allowed for the use of a multilayered solar cell device structure, with an electron-blocking layer of pure BP, a blend layer of BP and fullerene derivative, and a hole-blocking layer of pure fullerene derivative. This stack has a more ideal morphology than a single layer bulk heterojunction, as the heterojunction layer is composed of column-like structures of BP and fullerene, allowing for more continuous pathways between the interface and the electrodes while retaining a large interfacial area.[33] The morphology of phase II has been characterized using X-ray diffraction, scanning electron microscopy,[71] and photoconductive atomic force microscopy.[73] In addition, we have explored the use of thermally degradable polymers to increase solution viscosity and improve processability of BP devices.[74]

The microstructural changes during the thermal conversion process of CP to BP are complex. Spin-coated CP films are amorphous, but upon heating undergo a retro Diels-Alder reaction to form crystalline BP with the loss of 4 equivalents of ethylene, as shown by thermogravimetric analysis.[50] During the conversion process after loss of the ethylene groups, BP forms an intermediate phase, identified both by X-ray scattering and optical spectroscopy, that has been referred to as a "metastable phase" (phase I) before undergoing a phase transition to the final crystalline phase (phase II) (Fig. 2.1). Phase

II is also formed by vapor deposition of BP powder at temperatures higher than 150°C, while phase I is formed by vapor deposition of BP powder at temperatures lower than 80°C.[75] While phase II has a known bulk crystal structure, phase I is generally thought to be significantly less ordered than phase II because few out-of-plane diffraction peaks have been observed by specular X-ray scattering.[49]

The existence of two polymorphs of BP affects the absorption and power conversion efficiency of solar cells as well as the field effect mobility of transistors. In early BP solar cells, using vapor deposited phase I in a bilayer solar cell resulted in a similar efficiency as spin-coated phase II, 2.2%, however it is likely that solvent from the spin-coated acceptor layer converted this phase I into phase II.[72] The field effect mobility of vapor deposited phase I, $3x10^{-4}$ cm^2/Vs, is much higher than that of vapor deposited phase II, but lower than that of spin-coated phase II, $1.7x10^{-2}$ cm^2/Vs.[50] It should be noted that different degrees of photocurrent generation from different polymorphs have also been observed in phthalocyanines.[76,77]

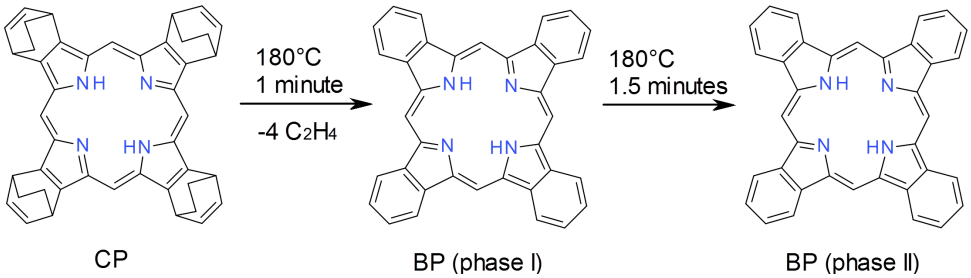

Figure 2.1: Chemical structure of CP and the two polymorphs of BP.

2.1.2 Experimental section

CP (1,4:8,11:15,18:22,25-tetraethano-29H,31H-tetrabenzo[b,g,l,q]porphin) powder was obtained from Mitsubishi Chemical. To prepare UV-vis samples, CP at a concentration of 7.5 mg/mL was spin coated onto glass substrates inside a glovebox from a solution of 2:1 chlorobenzene:chloroform resulting in 25 nm thick films. The films were annealed on a hot plate at a nominal temperature of 180°C for various times between 0.5 and 20 minutes.

To prepare films of CP for GIWAXS, 35 nm of PEDOT:PSS (poly(3,4-ethylenedioxythiophene)-poly(styrenesulfonate)) was spin coated onto clean silicon substrates and annealed at 180°C. Then, CP at a concentration of 7.5 mg/mL was spin coated inside a glovebox from a solution of 2:1 chlorobenzene:chloroform, resulting in a film thickness of 20-25 nm. GIWAXS on the 11-3 beamline at the Stanford Synchrotron Radiation Lightsource was used to observe the changes in the film's crystal structure and microstructure throughout the course of the transformation. A hot stage and a 2-D detector were used on this beamline, and annealing was carried out under flowing He gas. An incident angle of 0.10° or 0.12°, an X-ray energy of 12.7 keV, and a detector distance of 399.5 mm were used. To prepare films of CP on top of an underlying layer of already annealed phase II BP, the first CP layer was spin coated and annealed inside a glovebox at 180°C for 20 minutes, then the second CP layer was spin coated on top. The top layer was observed with 2-D GIWAXS using an incident angle of 0.08° so that most of the X-ray radiation

would only reach the CP layer and little diffraction from the phase II layer would be seen. Some discussion about incidence angles is in the SI.

The samples were prepared 1-3 days before GIWAXS was performed, and were transported in an airtight container. The final annealing temperatures were 160°C or 180°C, which are the temperatures typically used to anneal BP solar cells in the literature.[72] Due to calibration requirements, the heating stage had to be brought from room temperature to the final temperature with the sample already on it, taking approximately 4 minutes. Therefore, the samples' thermal history consisted of a ramp to the final temperature instead of an immediate jump. Soon after the start of the annealing ramp, the CP thermally converted to BP (29H,31H-tetrabenzo[b,g,l,q]porphyrin). After about 20 minutes of annealing, the samples were slowly brought back to room temperature by cooling with a fan. In addition to an initial diffraction pattern before heating, diffraction patterns were collected approximately every 2 minutes during the entire heating and cooling process using an exposure time of 30 seconds, and a final diffraction pattern was collected at room temperature. Additional samples that were previously annealed on a hot plate for various durations were also run in 2-D GIWAXS at room temperature. To limit beam damage, the samples were moved laterally 0.2 mm for every 8 minutes (at most) of X-ray exposure. Beam damage will increase disorder and reduce the intensity of the sharp peaks. However in our plots of peak intensity vs. time we have observed the effect to be quite small for the exposure times we are using.

The resulting raw diffraction patterns are a distorted representation of reciprocal space due to the grazing incidence geometry.[78,79] The WxDiff program was used to apply polarization and χ-corrections and plot the intensity versus the scattering vector components parallel and perpendicular to the substrate q_{xy} and q_z.[80] The absorbance correction to intensity was not applied because it is negligible in this geometry for organics. At grazing incidence, the section of each diffraction pattern close to the q_z axis cannot be measured without changing the incident angle to each Bragg angle of interest, but the non-zero peak widths in the polar angle χ allow for the tail of the peaks on the q_z axis to be observed. For some samples, pole figures were created by also scanning the incidence angle at the relevant Bragg angle and then stitching together the grazing incidence and Bragg angle scans.[79] Line scans were produced by integrating 2-D GIWAXS data over the polar angle range available in the 2-D GIWAXS images.

To prepare samples for TEM, PEDOT:PSS was spin coated onto substrates of silicon with a 150 nm thermal oxide. After spin coating and annealing of CP, The specimens for TEM were prepared by etching away the SiO_2 layer with a 5 vol% hydrofluoric acid solution. The floated thin film was placed on a TEM grid (Ted Pella Inc.). Imaging and diffraction experiments were performed with a FEI Tecnai G2 TEM at 200 kV.

Several hypothetical unit cells for phase I were obtained with Dicvol, an automated indexing routine for powders, using d-spacings obtained from 2-D GIWAXS and electron diffraction.[81] The SimDiffraction program[82] was used to generate the square of the

structure factor in reciprocal space, simulating corrected 2-D GIWAXS patterns for phase I and phase II from given unit cells, atom positions, and distributions of out-of-plane orientations. In the case of phase I, because the atom positions are unknown, systematic absences and peak intensities are neglected. The simulated patterns, the GIXD Igor Analysis Routine, and a custom MATLAB script to generate tables of peak locations were used to check the potential unit cells against the experimental GIWAXS patterns to select the best fitting BP phase I unit cell, modify the previously reported BP phase II bulk unit cell for thin films, and determine the distribution of crystallite orientations in both phases.

2.1.3 Results and discussion

Absorption spectra

The CP to BP phase I conversion and the phase I to phase II crystal-crystal transition was confirmed using UV-Vis absorption spectra that show the disappearance of the absorption features of phase I between 1.5-2.5 minutes of annealing at 180°C (Fig. 2.2). In porphyrins, there is typically a Soret band at a short wavelength and a Q band with several peaks at longer wavelengths.[34] The CP to BP phase I conversion corresponds to a redshift in the Soret band of the absorption spectrum from 380 nm to 410 nm and in the Q band from 500-620 nm to 550-660 nm. This transition occurs rapidly after the start of annealing. The phase I to phase II transition corresponds to a further redshift in Soret and Q bands to 445 nm and 640-690 nm respectively. Because the spectrum of phase I

matches the spectrum previously observed from phase I obtained by vapor-depositing BP powder onto a cold substrate, we confirm that the film converts to the metastable phase I before undergoing a phase transition to phase II. Interestingly, the peaks in the Q band in phase II are very intense, especially the longest wavelength one, compared to the weak Q peaks typically seen in porphyrins.[34] The increased absorption makes phase II more beneficial for use in organic solar cells.

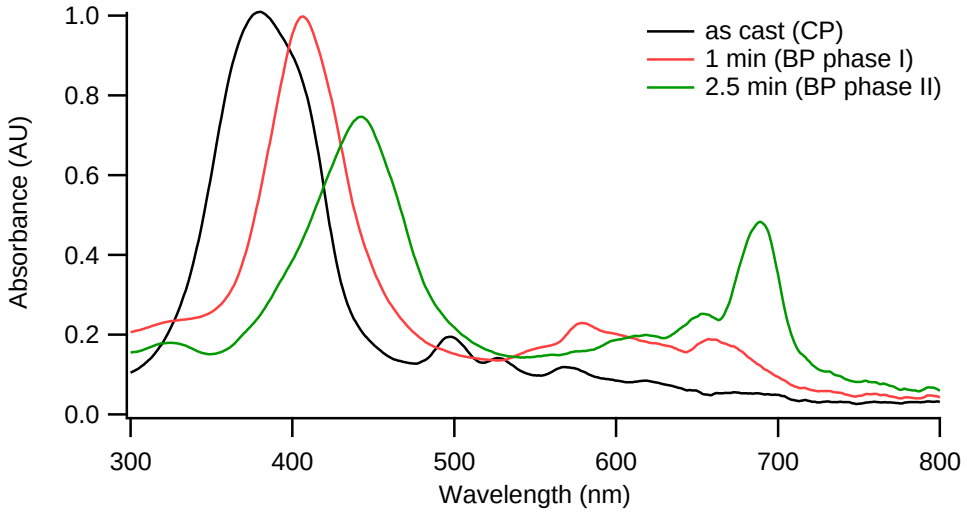

Figure 2.2: Absorption spectra of CP, BP phase I, and BP phase II with the same initial thickness after various annealing times at 180°C.

In samples where the temperature of the hot plate was not verified at the exact position of the sample (see SI), we observed that phase I peaks were still present at up to 4 minutes because of the temperature variation, estimated at between 167°C and 173°C. From this

we conclude that a small variance in temperature causes a large change in the kinetics of the phase transition.

Crystal structure

We used 2-D X-ray scattering to examine the crystal structures of BP phase I and phase II observed during the thermal conversion process of CP to BP at 180°C. While most X-ray studies examine single crystal, powder, or specular scattering, in this case the extra information from 2-D GIWAXS aids in the determination of the thin film unit cell. At the beginning of the in-situ GIWAXS experiment, the CP film was amorphous and a broad ring was observed in the diffraction pattern (Fig. 2.3a).

After some annealing time, a well-defined pattern of peaks corresponding to phase I (metastable BP) was observed, demonstrating that phase I is more highly ordered than previously believed (Fig. 2.3b). This figure was indexed with the proposed unit cell discussed further below. In this particular sample, the phase I diffraction pattern was observed in only one scan, which lasted between 3.75 and 4.25 minutes from the start of the annealing ramp. At the beginning of this scan, the sample was at 178°C and had been above 170°C for 2 minutes. The diffracted intensities were relatively high and there were three sets of diffraction planes with multiple orders of peaks, showing that crystallites with three dimensional ordering were formed. The intensity of the amorphous CP ring was also greatly diminished.

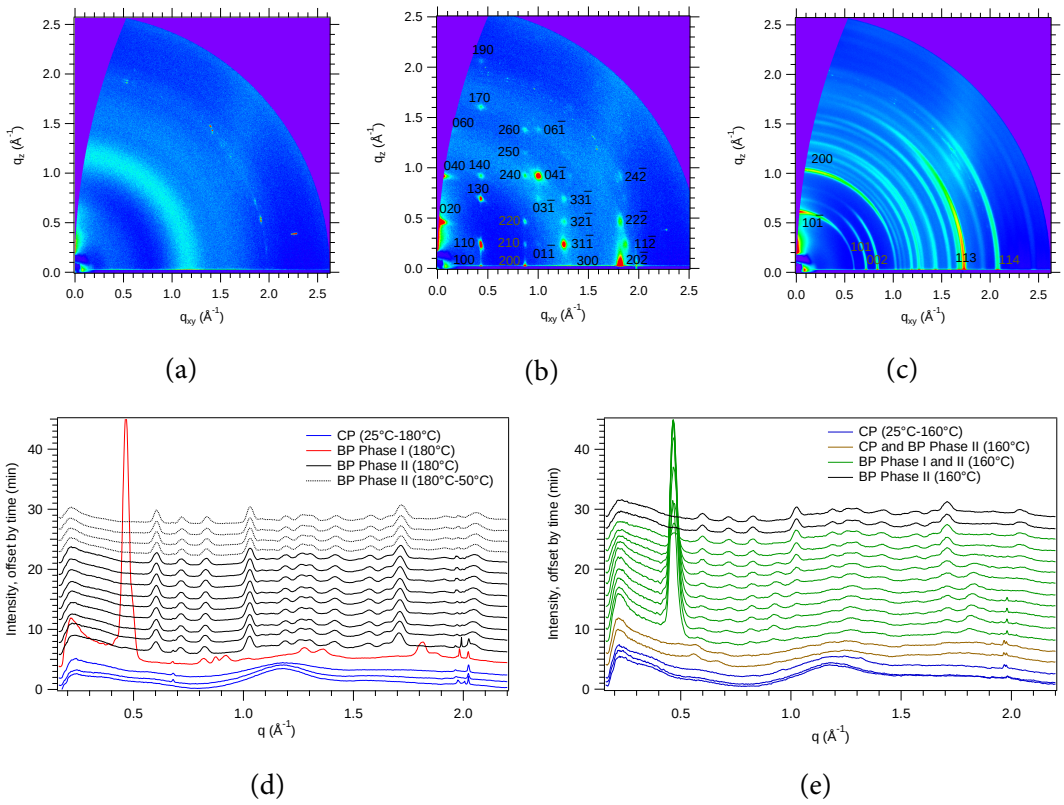

Figure 2.3: (a) 2-D GIWAXS of CP at 25°C as cast; (b) 2-D GIWAXS of BP phase I at 178°C with indexed peaks; (c) 2-D GIWAXS of BP phase II at 180°C with indexed peaks labeled. Line scans produced by integrating over polar angle during in-situ annealing and cooling, for (d) a final annealing temperature of 180°C, (e) a final annealing temperature of 160°C; the intensities are offset by the amount of time that has passed since the start of annealing.

The next diffraction image taken (Fig. 2.3c) shows that the phase I to phase II transition occurred rapidly. The peaks from phase I are no longer present in this scan, which

lasted between 5.6 and 6.1 minutes from the start of the ramp and shows only diffraction from phase II. As seen in Fig. 2.3d, the scattering peaks from phase I and phase II are at different q values, and therefore the unit cell and molecular packing are different in the two phases. The loss of crystalline texture (angular arcing of the peaks) will be discussed in the following section.

The stable phase II was found to have almost the same crystal structure as that of the single crystal obtained by Aramaki et al. (monoclinic, $P2_1/n$, a = 12.405Å, b = 6.591Å, c = 14.927Å, β = 101.445°).[49] In our films, we found that at room temperature, c is slightly increased to about 15.4Å. This is due to both thin film confinement and thermal expansion, since the bulk crystal structure was obtained at -180°C. Based on our current data, we are not able to separate the two effects. However the thin film crystal structure is very similar to that of the bulk, which is not always the case in other organic thin films.[83] Changes in the unit cell will influence electronic properties; for example, changes due to lattice strain have been found to alter the charge carrier mobility in thin film transistors.[84]

The diffraction pattern of this modified structure (a = 12.405Å, b = 6.591Å, c = 15.4Å, β = 101.445°) was simulated with SimDiffraction[82] and compared to the experimental 2-D GIWAXS data. The molecular packing assumed in the simulation has the same fractional coordinates as the bulk single crystal, but is stretched along the c-axis. The integrated intensities versus q in the simulated and experimental data are very similar and the agreement was much improved with the modification in the crystal structure

(Fig. 2.4c), supporting the assertion that this is indeed the correct packing of phase II in the thin film.

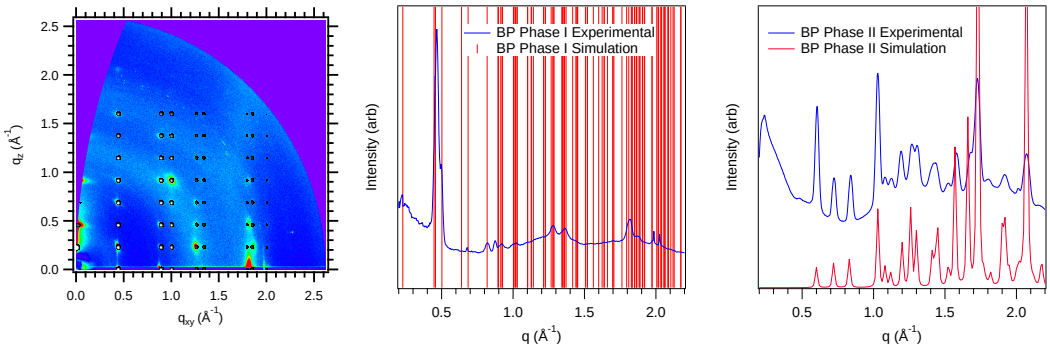

(a) (b) (c)

Figure 2.4: (a) Overlay of experimental (color) and simulated (grayscale) 2-D GIWAXS of BP phase I with (010) orientation; (b) Comparison of simulated and actual line scans for BP phase I; (c) Comparison of simulated and actual line scans for BP phase II. Line scans were produced by integrating over polar angle.

The crystal structure of phase I is unknown, so we have used a combination of 2-D GIWAXS and electron diffraction to index the unit cell. Several possible unit cells for phase I were obtained with an automated indexing routine for powders using d-spacings obtained from these two techniques.[81] However, the powder indexing routine does not take into account the peak locations in q_{xy} and q_z when searching for possible unit cells, only q. This extra information was used to find the best unit cell by modeling the scattering from each unit cell with SimDiffraction and assessing which one best matches

the experimental 2-D GIWAXS data. The best fit for the phase I peaks is the following monoclinic unit cell: a = 15.7Å, b = 27.5Å, c = 7.0Å, β = 116.5°. The film has strong out-of-plane texture with the (010) planes parallel to the substrate surface. The indexed peaks are shown in Fig. 2.3b. The d-spacings of this unit cell match the experimental data well (see SI).

By comparing the simulated and experimental peaks, we also gained information about the symmetry of the phase I crystal structure (Figs. 2.4a and 2.4b). As the simulation does not contain the unknown symmetry, it displays peaks in Fig. 2.4a which are missing from the experimental data because of systematic absences due to symmetry. Not all the missing peaks can be matched to a symmetry element, but the 010, 030, and 050 peaks are missing, indicating that there is a 2-fold screw axis parallel to the b-axis. Also, note that the 300 peak is present but very faint. The volume of the proposed phase I unit cell is 2.19 times that of the modified phase II unit cell (2704.7Å^3 compared to 1234.1Å^3). Assuming that the densities of the two phases are close, there should be four molecules per unit cell in phase I compared to two in phase II.

Films annealed in-situ at a lower temperature of 160°C (Fig. 2.3e) have a different thermal conversion and phase transition behavior than the previously discussed 180°C films. With the lower temperature, both phase I and phase II were present throughout much of the annealing process, while in films annealed at the higher temperature, only one phase was observed during each scan because the kinetics are rapid. Interestingly,

before the very intense phase I peak appeared in the scan that starts at 7.8 minutes, two of the lower-q phase II peaks appeared faintly in two scans starting at 3.9 minutes. This indicates that a small fraction of the film has converted to phase II BP during the time between 1.9 minutes (the end of the previous scan) and 3.9 minutes. Because of the time between scans, we do not know whether this fraction converted directly from CP to phase II, or went from CP to phase I to phase II. After phase I appeared the main phase I peak grew more intense until 10 minutes, and thereafter decreased in intensity until it disappeared at 27 minutes while phase II increased in intensity. In the literature, larger grain sizes and decreased roughness have been observed in BP films converted at lower temperatures.[71]

The transformation kinetics at higher temperatures were also observed with ex situ GIWAXS on samples directly annealed on a hot plate for various annealing times at 180°C (the samples reach this temperature within 1 second). Thermal conversion followed by phase transition were observed, with only BP phase I peaks seen in the samples annealed for 1.0 and 1.5 minutes, and only phase II peaks seen in the samples annealed for 2.5 minutes or longer (see SI). As these samples were examined with GIWAXS several days after annealing, this shows that phase I does not spontaneously convert to phase II if it is not annealed further.

Crystallite size, morphology, and texture

The Scherrer equation was used to calculate the average crystallite size along various crystallographic directions in the two phases of BP:[85]

$$D = \frac{K\lambda}{B_{hkl}\cos\theta}$$

where D is the crystallite size along the diffraction direction, K is the Scherrer constant, here taken as 0.9, λ is the X-ray wavelength, B_{hkl} is the crystallite size contribution to the full width at half maximum of the hkl peak when plotted in terms of 2θ, and θ is the Bragg angle of the hkl peak which is equal to $\sin^{-1}(q\lambda/4\pi)$. B_{hkl} differs from the measured peak width $B_{exp} = \Delta q_{exp}\lambda/4\pi\cos\theta$ because of several factors. First, geometric smearing due to the finite length of the beam footprint on the sample contributes significantly to measured peak width.[86] When this footprint is taken into account, the equation for the sample-specific contribution to peak width B_{sample} is:

$$B_{sample} = (B_{exp}^2 - B_{geo}^2)^{1/2} = \left[\left(\frac{\Delta q_{exp}\lambda}{4\pi\cos\theta}\right)^2 - \left(\frac{w\tan(2\theta)}{L}\right)^2\right]^{1/2}$$

where B_{geo} is the geometric smearing contribution to peak width, w is the footprint of the beam on the sample (5 mm) and L is the sample-detector distance (399.5 mm).

If B_{sample} does not vary with peak order h in a series of peaks, the major contributor to B_{sample} is the crystallite size and $B_{hkl} = B_{sample}$. However, if there is a linear relationship between B_{sample} and h in a series of peaks, part of the peak width can be attributed to nonuniform strain, and if there is a linear relationship between B_{sample} and h^2, part of

the peak width can be attributed to paracrystalline disorder.[85,87] In the latter case, B_{hkl} can be estimated by linear regression using the following equation:[68,88]

$$B^2_{sample} = B^2_{hkl} + (q^2\pi^4 g^4)h^4$$

where g is the paracrystalline disorder parameter.

There are three series of peaks with multiple orders in phase I BP. The 100 and 200 in-plane peaks have the same B_{sample}, so the crystallite size in the in-plane direction is calculated to be 32.6 nm with negligible nonuniform strain or paracrystalline disorder. For the 020, 040, and 060 out-of-plane peaks, the relationship between width and peak order is consistent with a small amount of paracrystalline disorder (see SI). This is also true for the 110 and 220 off-axis peaks. The crystallite size is calculated to be 18.7 nm in the out-of-plane direction and 30.1 nm in the [110]* direction. It should be noted that the former value is approximately equal to the film thickness. The paracrystalline disorder parameter is 1.4x10^{-2} in the out-of-plane direction and 1.1x10^{-2} in the [110]* direction. These values are similar to those observed in other small molecules and several times smaller than typical paracrystalline disorder parameters in polymers.[68]

In phase II BP, there are no series of peaks with multiple orders, so the Scherrer equation is not strictly applicable in determining crystallite size. Using the peak width of the peak with the lowest q-value, $10\bar{1}$, the nominal crystallite size is found to be 44.0 nm.

Bright field TEM shows that the two phases of BP have different morphologies in addition to the differing crystal structures. In phase I (Fig. 2.5a), diffuse grains approxi-

mately 400 nm in diameter composed of lighter and darker areas were observed. Based on the contrast inside the grains and the crystallite size obtained from peak width analysis of the GIWAXS patterns, these grains are composed of many small crystallites with the same out-of-plane orientation. The darker streaks, which are oriented in about the same direction within each grain, are crystallites of phase I, while the lighter streaks inside the grains are less ordered areas of CP or BP. The large dark spots are silicon dust. In general, more crystalline areas are darker because more electrons are diffracted. Bright field images of BP phase II (Fig. 2.5c) show that this phase has more distinct and anisotropic grains, about 150-200 nm in width and 150-1000 nm in length. However, BP coverage is worse than in phase I, due to the film dewetting in some areas. Based on peak width analysis of the GIWAXS patterns, the phase II grains also are not single crystals but are composed of many small crystallites with the same out-of-plane orientation.

Electron diffraction of the two phases help to confirm the unit cells determined from 2-D GIWAXS and to assess the degree of in-plane texture. Electron diffraction of phase I with an aperture of the same size as the bright field image showed a diffraction ring (Fig. 2.5b inset), indicating that over micron-sized areas there are crystallites with different in-plane orientations. But when a small aperture (about 270 nm in diameter) was used to focus on one of the grains containing light and dark streaks (Fig. 2.5b), distinct peaks were observed, indicating that the crystallites inside each grain have the same in-plane orientation as well as out-of-plane. The d-spacings of these peaks match the ones

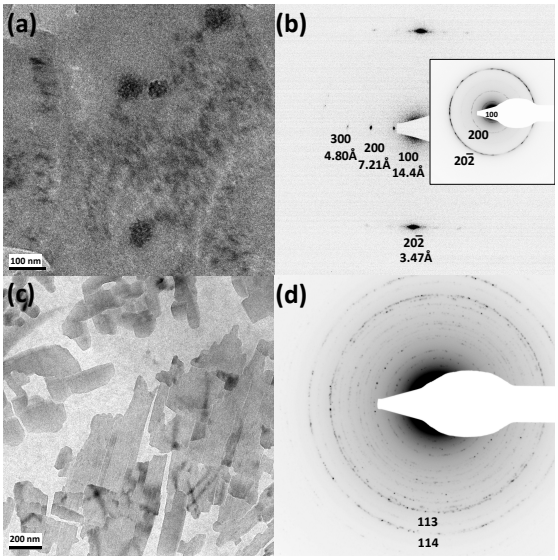

Figure 2.5: (a) Bright field TEM of BP phase I; (b) Electron diffraction of BP phase I with a 270 nm aperture (inset: large aperture); (c) Bright field TEM of BP phase II; (d) Electron diffraction of BP phase II with a large aperture.

observed in 2-D GIWAXS on the q_{xy} axis and these peaks are indexed according to the proposed phase I unit cell. The angle of the peaks also reveals some information that is not provided by 2-D GIWAXS in that the 3.47Å peak corresponds to a diffraction plane that is approximately normal from the other three in-plane peaks. The $20\overline{2}$ peak is at a 93.3° angle from the other three peaks, which closely matches the calculated 93.02° angle in the proposed unit cell. Electron diffraction of phase II using a large aperture shows that grains are formed with different in-plane orientations (Fig. 2.5d).

Now we examine the out-of-plane texture in both phases of BP. In phase I, the distinct peaks (Fig. 2.3b) show that it has a very strong degree of out-of-plane texture, i.e.

almost all its crystallites have the same out-of-plane orientation, similar to pentacene films. In phase II, the arcs in the polar angle indicate that it has a much weaker degree of out-of-plane texture than phase I. In phase II, the texture is observed to be a broad distribution centered about two out-of-plane orientations, (100) and (10$\bar{1}$). This is suggested by the fact that these two peaks have arcs which are most intense near q_z. To support this observation, SimDiffraction was used to simulate 2-D GIWAXS patterns of a set of phase II crystallites with the modified crystal structure, having a broad (a FWHM of 90° is simulated) Gaussian distribution of out-of-plane orientations centered on each of these orientations (Fig. 2.6a and b). Each of the simulated patterns closely matches parts of the experimental data, showing that the combination of the two distributions describes the out-of-plane texture well.

Both phases of BP have $\pi-\pi$ stacking along a direction close to parallel to the substrate. The unit cells and out-of-plane orientations were plotted with the VESTA program[89] (Fig. 2.7a). It can be seen that in both favored orientations of phase II, the molecules are close to edge-on to the substrate. In the (10$\bar{1}$) orientation, the planes of the molecules are 16.0° off perpendicular to the substrate, and in the (100) orientation, the planes of the molecules are 21.4° off perpendicular to the substrate. Note that although the molecules are in a "herringbone" arrangement relative to each other, the planes of the molecules, which are approximately (115) and (1$\bar{1}$5), have the same angle with the substrate. For the molecules to be perfectly edge-on to the substrate, the sample would need to have the

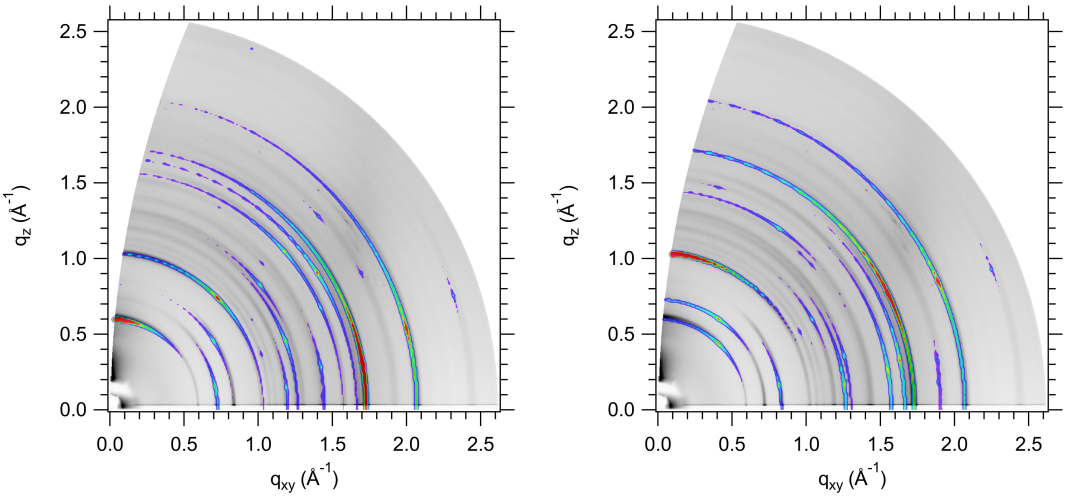

Figure 2.6: Overlay of experimental (grayscale) and simulated (color) 2-D GIWAXS at 25°C of (a) BP phase II with $(10\bar{1})$ orientation, (b) BP phase II with (100) orientation.

$(20\bar{1})$ out-of-plane orientation (Fig. 2.7b). In phase I, we conjecture that $\pi - \pi$ stacking is somewhat more edge-on than in phase II because of the shape of the unit cell. Unlike in the phase II unit cell, there is enough room for the molecules to lie edge-on and not adopt a herringbone arrangement, as the b-axis is long enough that two molecules can lie one on top of the other. This potential difference in $\pi - \pi$ stacking can strongly affect charge transport and mobility.

After assigning the unit cells and out-of-plane orientations of phase I and phase II, we examine the question of why phase I has a much stronger degree of texture than phase II. During the phase transition from phase I to phase II, the molecules twist into

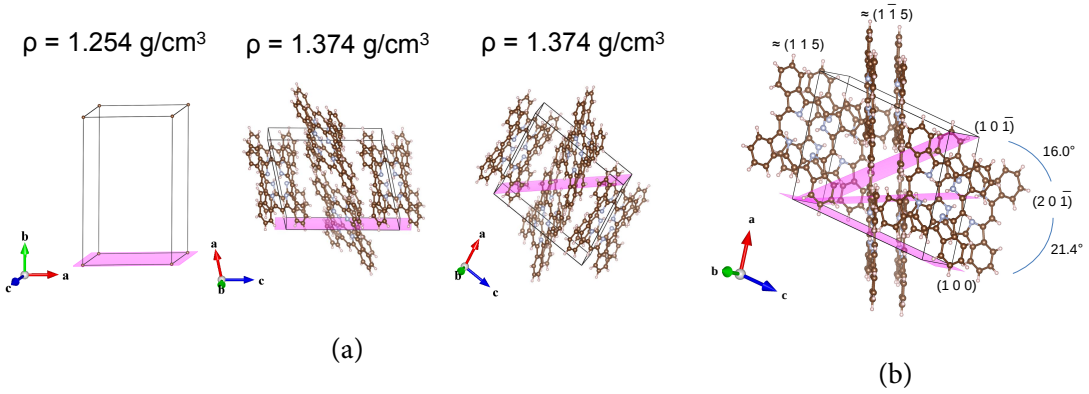

Figure 2.7: Unit cells of: (a) Left to right: BP phase I with (010) orientation, BP phase II with (100) orientation, BP phase II with (10$\bar{1}$) orientation; (b) Illustration of the two dominant out-of-plane orientations in BP phase II, (100) and (10$\bar{1}$), the out-of-plane orientation which would have given edge-on in-plane $\pi - \pi$ stacking, (20$\bar{1}$), and the angles between them.

a herringbone arrangement. In different nuclei of the new phase, the molecules may twist in different directions causing a loss of texture as the new crystallites have different orientations. The rapid nature of the phase transition (a complete disappearance of phase I within 1 minute at 180°C) suggests that there are a large number of these nuclei, which leads to a weak degree of texture. It was observed that the slower phase transition that occurs at lower annealing temperatures leads to a greater degree of texture in the final phase II (see SI).

Finally, it was observed that the *d*-spacing of each peak in phase II BP decreases during in-situ annealing and cooling. The peak position, width, and height of six peaks were plotted as a function of heating and cooling time and temperature (see SI). There is no clear trend in peak width or height, indicating that the crystallites do not grow or become more numerous over a long period of time but instead that the microstructure is fixed within at most two minutes after the initial formation of phase II. However, the *d*-spacing of each peak decreases by about 0.5 to 1% during the heating process which occurs at a constant 180°C, which is unusual and may be caused by annealing out defects. The *d*-spacing continues to decrease when the heat stage is turned off and the sample is cooled, because of thermal contraction. At about 63°C, the *d*-spacing decreases more rapidly, suggesting that the thermal expansion coefficient is temperature dependent. This behavior was observed for all of the peaks, as shown in the plots of normalized *d*-spacing (see SI). Rough approximations of average thermal expansion coefficients were calculated to be 1.2x10^{-5} K^{-1} between 180°C and 63°C, and 3.4x10^{-4} K^{-1} below 63°C.

Growth of seeded films

Finally, we examined the question of whether the thermal conversion and phase transition behavior of BP depends on nucleation sites. We annealed a film of CP which was on top of an underlying layer of already annealed phase II BP and observed the differences in crystallization behavior using in-situ 2-D GIWAXS compared to the behavior with-

out an underlying BP layer. As with the other films, the temperature was ramped from room temperature to final annealing temperatures of 160°C and 180°C (Fig. 2.8a and b). Before annealing, the diffraction pattern was almost the same as that of CP without an underlying layer as in Fig. 2.3a, because the incident X-ray angle is small such that diffraction occurs from mostly the top layer (refer to SI for incident angle calculations). During annealing, significantly intense diffraction peaks from phase II were observed first, and peaks from phase I later appeared and then disappeared. As the phase I peaks disappeared, the phase II peaks became more intense. This is similar to the behavior of single layer films annealed at 160°C (Fig. 2.3e), but it appears that with an underlying layer, a much larger fraction of the top layer converted directly from CP to phase II BP. This could be the result of a significant fraction of the top layer growing off of the underlying phase II layer. This behavior could also have been the result of gaps starting to form in the CP layer near the start of annealing but before conversion, allowing for diffraction from the underlying phase II BP layer. However, TEM of phase I BP does not indicate that there are gaps in the film, and so this seems unlikely.

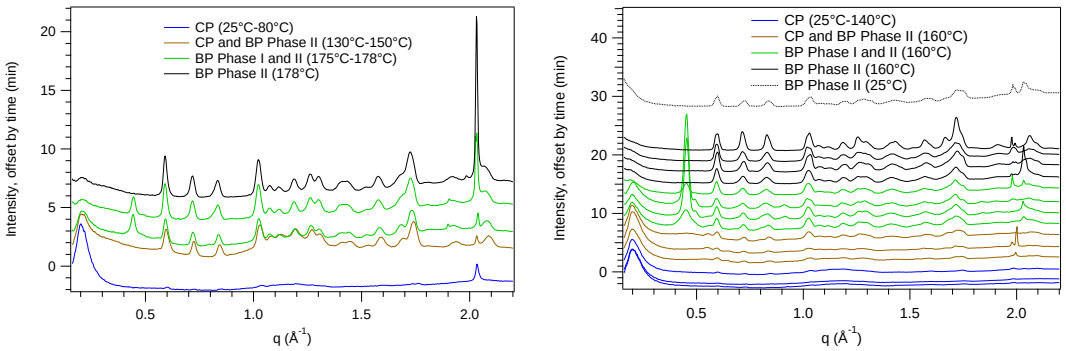

(a) (b)

Figure 2.8: Line scans (2-D GIWAXS integrated over polar angle) during in-situ annealing and cooling, for CP films with an underlying BP layer and (a) a final annealing temperature of 180°C, (b) a final annealing temperature of 160°C. The intensities are offset by the amount of time that has passed since the start of annealing.

2.1.4 Conclusion

In-situ 2-D GIWAXS has been shown to be a particularly useful tool for characterizing phase transitions in a material used for solution-processed organic solar cells, as it rapidly yields information about the transformation behaviors, crystal structures, textures, and crystallite sizes of the various phases during annealing. We have used this technique to study the CP to BP conversion and the crystal-crystal phase I to phase II transition in tetrabenzoporphyrin thin films, along with the use of GIWAXS simulation to study texture and TEM to study morphology. Emerging solid state detectors[64] will enable faster

detection that will allow for these kinds of structural changes to be observed with a higher time resolution.

The annealing temperature used and the presence of an underlying BP film both affect the phase transition behavior. In samples annealed at 180°C without an underlying film, all of the CP first converts to BP phase I before transitioning to phase II. In samples annealed at 160°C without an underlying film, or annealed at 160°C or 180°C with an underlying film, phase I and phase II are both present during much of the annealing time. In the samples with an underlying film a significant fraction of the CP is converts directly to phase II BP by growing off of the underlying layer.

2-D GIWAXS and electron diffraction data have yielded a preliminary unit cell for the metastable phase I. Phase I potentially has different $\pi - \pi$ stacking than phase II as there is room in the unit cell for a non-herringbone molecular arrangement, leading to differences in charge transport. 2-D GIWAXS has also allowed us to find the thin film crystal structure of phase II, slightly distorted from the previously found bulk crystal structure due to confinement.

Phase I has strong out-of-plane texture and this texture is lost when it converts to phase II, which is a surprising finding. We find that the crystallites in phase II have a distribution of orientations centered about the (100) and $(10\bar{1})$ out-of-plane orientations, and for both of these, the molecules are oriented close to edge-on to the substrate. TEM shows that phase I has diffuse grains while phase II has distinct and anisotropic grains with gaps

in between grains. In-plane texture within individual grains is also noted in both phases. Peak width analysis estimates the crystallite sizes in phase I to range between 19 and 33 nm, and reveals that these crystallites exhibit a small degree of paracrystalline disorder in two non-in-plane directions. The crystallite sizes in phase II grow to approximately 44 nm.

Our characterization of the properties of polymorphic phases during the structural transition of BP is critical because the differences in unit cell, $\pi - \pi$ stacking, crystallite orientation, morphology, and crystallite size all lead to differences in charge transport and therefore electronic device performance.[31] A wide variety of other soluble porphyrin and phthalocyanine precursors with or without metal centers have also recently been synthesized,[36] and the crystallization behavior of BP may be useful in understanding these similar molecules. More broadly, understanding polymorphism in organic compounds is important in other fields, for example influencing the dissolution rate and efficacy of a pharmaceutical.[90] In-situ 2-D GIWAXS combined with simulation is a valuable technique to understand transient behaviors in organic compounds such as these.

2.1.5 Supporting Information

Incident angles of 0.10° and 0.12° were used for the 2-D GIWAXS samples with a single 20-25 nm layer of CP or BP on top of 35 nm of PEDOT:PSS and a Si substrate. These angles were selected by taking short-exposure diffraction patterns at different incident

angles and picking the ones that resulted in the best signal to noise ratio of diffraction from BP to diffraction from Si. Snell's law shows that for an incident angle of 0.12° into the BP, the X-rays are transmitted through the BP and PEDOT:PSS layers but undergo total internal reflection at the PEDOT:PSS/Si interface, which improves the signal to noise ratio.[91] The refractive indices of each layer and the substrate were calculated using the Center for X-Ray Optics website (Lawrence Berkeley National Laboratory, `http://henke.lbl.gov/optical_constants/`). The density of PEDOT:PSS used was 1.45 g/cm^3.[92]

```
BP (C36H22N4) Density=1.374
Energy(eV), Delta, Beta
12700.  1.8450E-06  1.1963E-09

PEDOT:PSS (C14H11S2O5) Density=1.45
Energy(eV), Delta, Beta
12700.  1.9349E-06  6.7799E-09

Si Density=2.33
Energy(eV), Delta, Beta
12700.  3.0193E-06  2.8730E-08

90-asind(1*sind(90-0.12)/(1-1.8450E-6)) = 0.0478

90-asind((1-1.8450E-6)*sind(90-0.0478)/(1-1.9349E-6)) = 0.0412

90-asind((1-1.9349E-6)*sind(90-0.0412)/(1-3.0193E-6)) = 0 + 0.0736i
```

For the in-situ samples with a layer of CP on top of a layer of BP, the incident angle of 0.08° was selected by taking short-exposure diffraction patterns at different incident angles and picking the greatest incident angle where no diffraction from BP was observed.

The electric field distribution was plotted using the XOP program with the IMD extension (Fig. 2.9), showing that at 0.08°, the evanescent wave of the electric field only penetrates into the CP layer so that there can be no diffraction from the BP layer, while at higher incident angles the electric field is non-zero in both layers.

Pole figures of BP phase II samples annealed at different temperatures were created by stitching together the 2-D GIWAXS data from grazing incidence and from the Bragg angle for the 200 peak[79] (Fig. 2.10d). The pole figures show that there is a greater degree of crystalline texture for samples annealed at lower temperatures.

Peak fitting was conducted on the pole figure of the 200 arc of the sample annealed at 180°C (Fig. 2.11). The large peak centered on the q_z axis corresponds to the (100) out-of-plane orientation, and the small peak about halfway between the q_z and q_{xy} axes corresponds to the $(10\bar{1})$ out-of-plane orientation. Peak fitting was used to find the locations and intensities of these peaks. SimDiffraction was used to simulate the intensity of the 200 peak assuming that the entire sample had the (100) out-of-plane orientation and then the $(10\bar{1})$ out-of-plane orientation. The locations of the simulated peaks (χ = 46.78° for $(10\bar{1})$ out-of-plane, and χ = 90° for (100) out-of-plane) closely matched those of the experimental peaks. The intensities of the simulated peaks were compared with the intensities of the experimental peaks to find the ratio of BP in the film with the $(10\bar{1})$ out-of-plane orientation to that with the (100) out-of-plane orientation. The ratio obtained was 1.05 to 1. It should be noted that this is an approximate number and is done simply to show

the potential usefulness of the method, because we have not taken into account factors such as multiple scattering, beam divergence, surface roughness, and Lorentz and other corrections which affect the peak intensities.

Figure 2.12 shows that the 2-D GIWAXS peaks of BP samples annealed on a hotplate are similar to those of samples annealed in-situ during GIWAXS.

Figure 2.13 is just a larger version of Figure 4a of the main text.

Figure 2.14 shows the simulated 2-D GIWAXS peaks that are overlaid in Figures 4a and 6 of the main text.

Figure 2.15 shows a table of observed and model BP phase I peaks with deviations in d-spacing.

Figure 2.16 shows the fits to the equation $B^2_{sample} = B^2_{hkl} + (q^2\pi^4 g^4)h^4$ to obtain B_{hkl} and g for two sets of peaks in BP phase I.

Figure 2.17 shows how the d-spacing of each peak in phase II BP decreases during in-situ annealing and cooling.

Figure 2.18 shows how the height and area of the broad amorphous CP peak decreases linearly with time during in-situ heating at 180°C.

Finally, Figure 2.19 shows UV-Vis spectra of CP/BP films annealed at slightly lower temperatures than in the main text, showing that a small variance in temperature causes a large change in the kinetics of the phase transition.

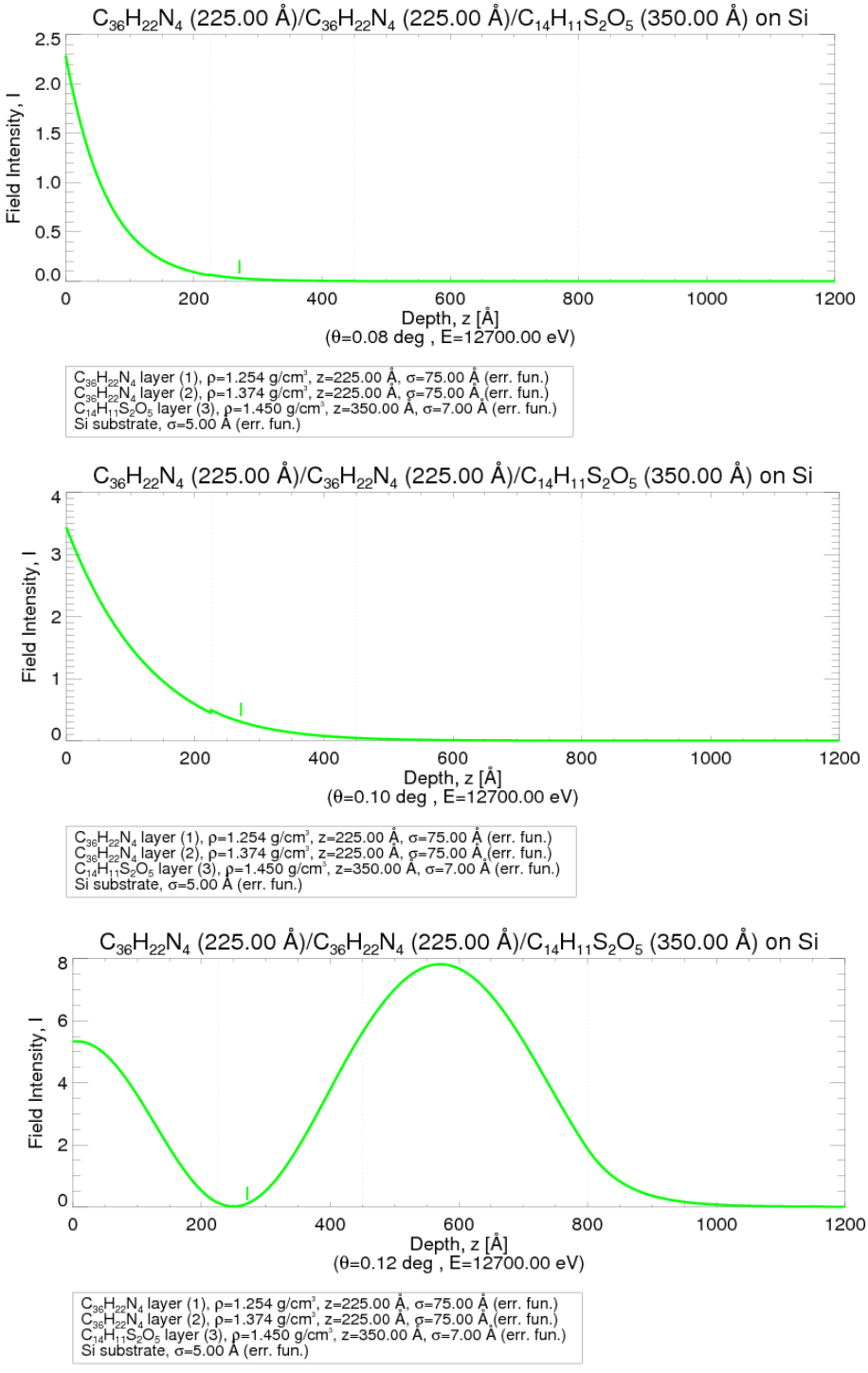

Figure 2.9: Calculated electric field in the Si/PEDOT:PSS/BP/CP stack during 2-D GI-WAXS at three incidence angles

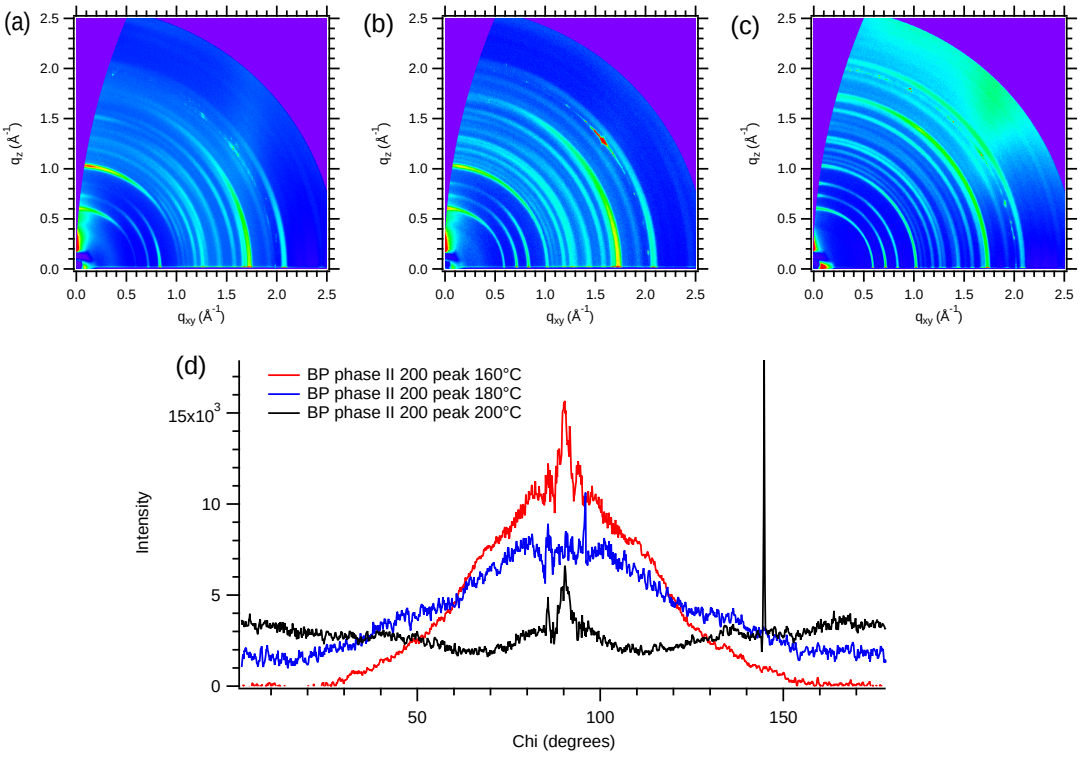

Figure 2.10: Non in-situ 2-D GIWAXS of: (a) BP phase II annealed at 160°C for 20 minutes, (b) BP phase II annealed at 180°C for 20 minutes, (c) BP phase II annealed at 200°C for 20 minutes; (d) Stitched pole figure of the 200 peak in the above samples.

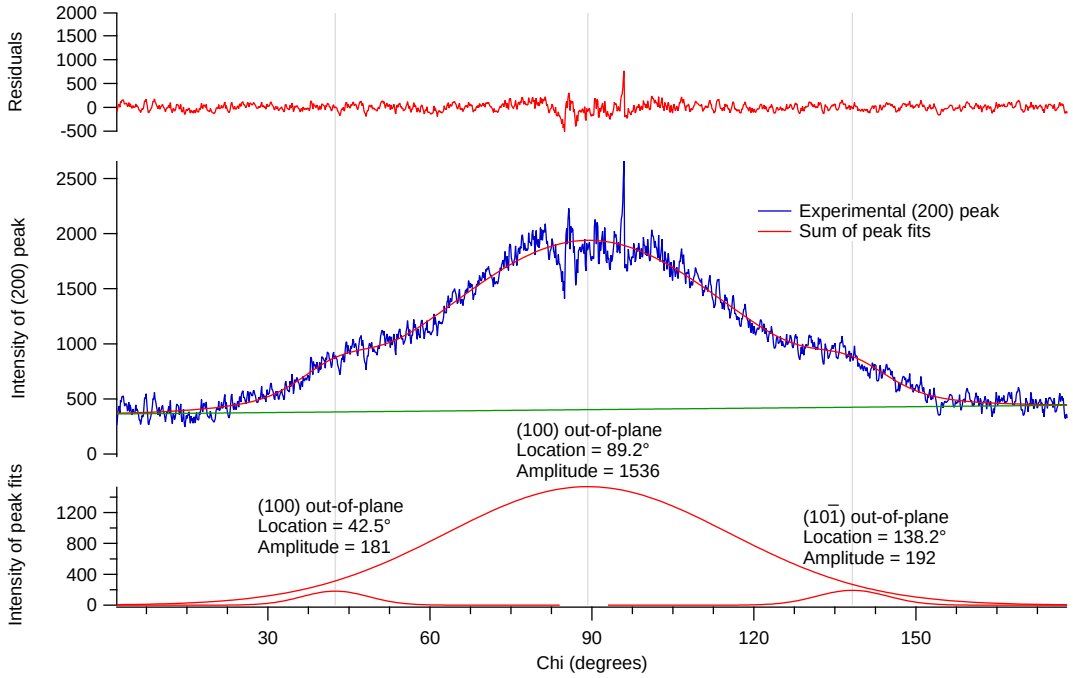

Figure 2.11: Experimental BP phase II 200 arc vs. χ, the fits of the peaks corresponding to the (100) and (10$\bar{1}$ out-of-plane orientations, the sum of the peak fits, and the residual of the sum of the peak fits.

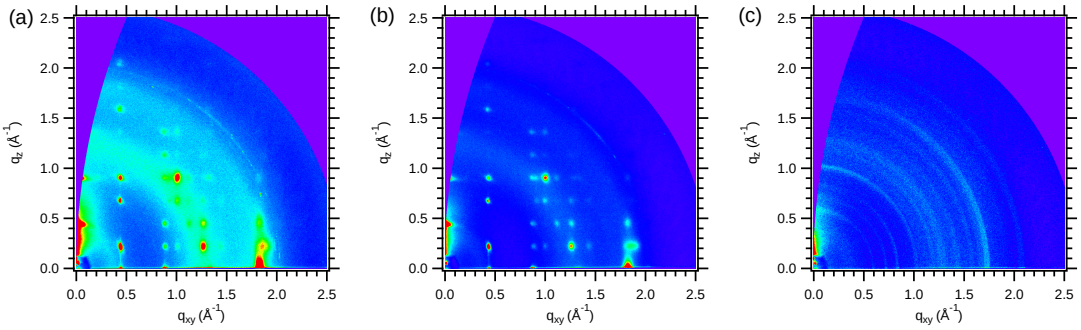

Figure 2.12: Non in-situ 2-D GIWAXS of: (a) BP phase I annealed at 180°C for 1 minute, (b) BP phase I annealed at 180°C for 1.5 minutes, (c) BP phase II annealed at 180°C for 2.5 minutes.

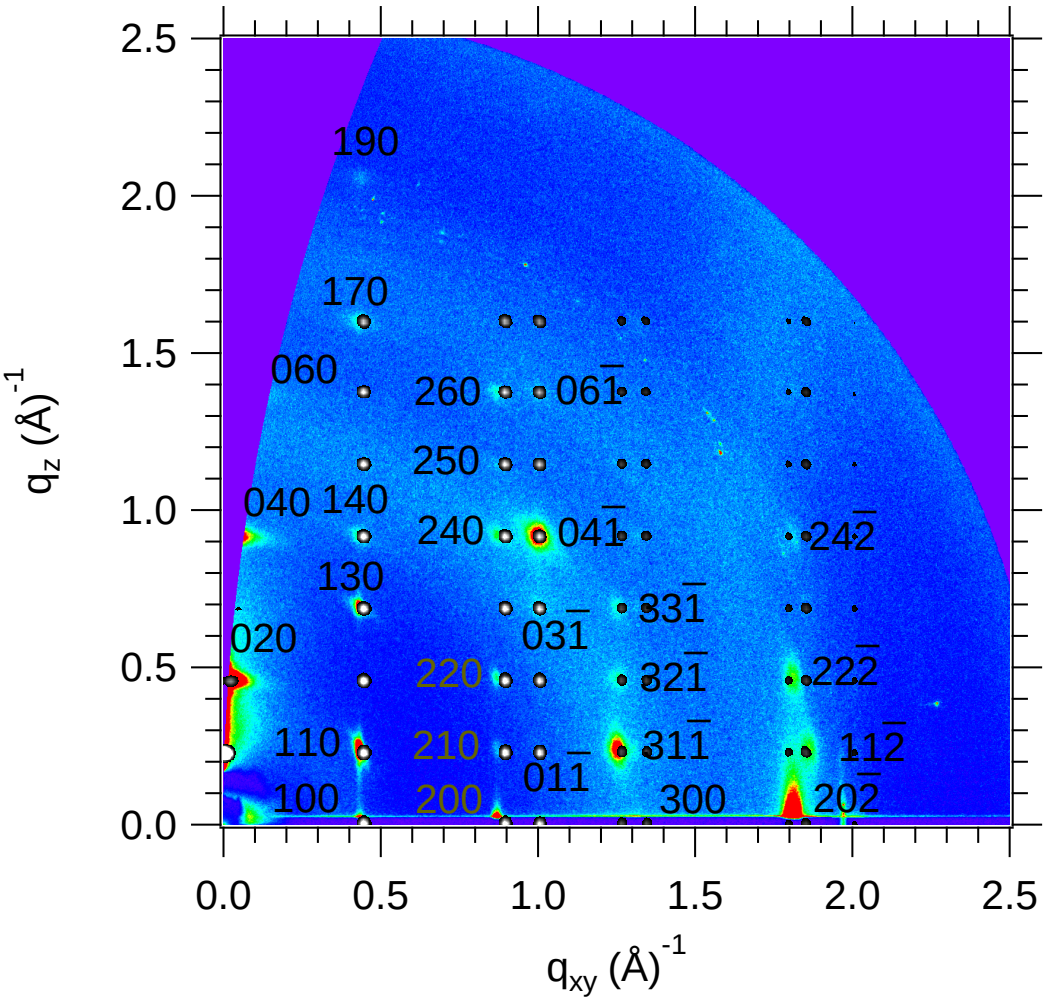

Figure 2.13: Overlay of experimental (color) and simulated (grayscale) 2-D GIWAXS of BP phase I (010) parallel to the substrate with peaks appearing in the experimental data labeled.

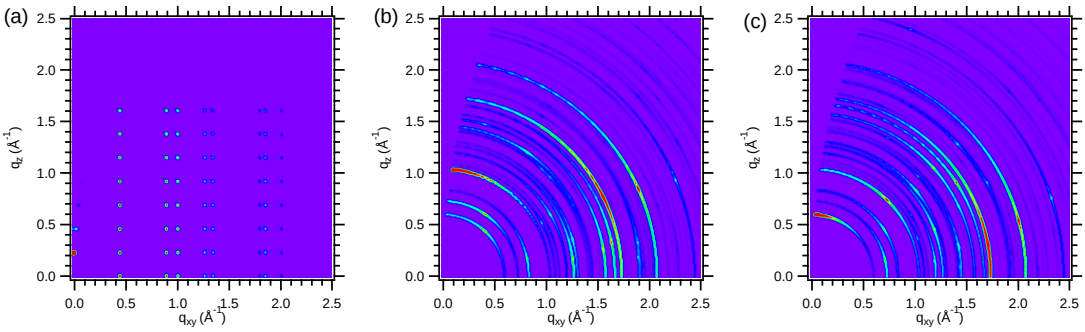

Figure 2.14: Simulated 2-D GIWAXS of (a) BP phase I (010) parallel to the substrate, (b) BP phase II (10$\bar{1}$) parallel to the substrate, (c) BP phase II (100) parallel to the substrate.

Calculated							Experimental GIWAXS				Experimental ED		Calculated - Actual GIWAXS
h	k	l	qxy(Å^-1)	qz(Å^-1)	q(Å^-1)	d(Å)	qxy(Å^-1)	qz(Å^-1)	q(Å^-1)	d(Å)	angle(°)	d(Å)	% error in calculated d
0	1	0	0.000	0.228	0.228	27.500							
1	0	0	0.447	0.000	0.447	14.050	0.435	0	0.435	14.444	150.8	14.4	-2.725
0	2	0	0.000	0.457	0.457	13.750	0	0.468	0.468	13.426			2.416
1	1	0	0.447	0.228	0.502	12.512	0.435	0.24	0.497	12.647			-1.067
1	2	0	0.447	0.457	0.639	9.827							
0	3	0	0.000	0.685	0.685	9.167							
1	3	0	0.447	0.685	0.818	7.677	0.435	0.695	0.820	7.663			0.183
2	0	0	0.894	0.000	0.894	7.025	0.87	0	0.870	7.222	150.8	7.21	-2.725
1	0	-1	0.898	0.000	0.898	7.000							
0	4	0	0.000	0.914	0.914	6.875	0	0.917	0.917	6.852			0.337
2	1	0	0.894	0.228	0.923	6.807	0.87	0.24	0.902	6.962			-2.232
1	1	-1	0.898	0.228	0.926	6.784							
2	0	-1	1.003	0.000	1.003	6.266							
0	0	-1	1.003	0.000	1.003	6.265							
2	2	0	0.894	0.457	1.004	6.256	0.87	0.468	0.988	6.360			-1.639
1	2	-1	0.898	0.457	1.007	6.238							
1	4	0	0.447	0.914	1.017	6.175	0.435	0.917	1.015	6.191			-0.247
2	1	-1	1.003	0.228	1.028	6.110	1	0.24	1.028	6.110			0.002
0	1	-1	1.003	0.228	1.029	6.108	1	0.24	1.028	6.110			-0.027
2	2	-1	1.003	0.457	1.102	5.702							
0	2	-1	1.003	0.457	1.102	5.701							
2	3	0	0.894	0.685	1.127	5.576							
1	3	-1	0.898	0.685	1.129	5.563							
0	5	0	0.000	1.142	1.142	5.500							
2	3	-1	1.003	0.685	1.215	5.173	1	0.695	1.218	5.159			0.266
0	3	-1	1.003	0.685	1.215	5.172	1	0.695	1.218	5.159			0.245
1	5	0	0.447	1.142	1.227	5.122							
3	0	-1	1.267	0.000	1.267	4.960							
2	4	0	0.894	0.914	1.279	4.914	0.87	0.917	1.264	4.971			-1.149
1	4	-1	0.898	0.914	1.281	4.905							
3	1	-1	1.267	0.228	1.287	4.881	1.254	0.24	1.277	4.921			-0.820
3	0	0	1.342	0.000	1.342	4.683	1.31	0	1.310	4.796	150.8	4.8	-2.353
3	2	-1	1.267	0.457	1.347	4.665	1.254	0.468	1.338	4.694			-0.615
2	4	-1	1.003	0.914	1.357	4.631	1	0.917	1.357	4.631			0.008
0	4	-1	1.003	0.914	1.357	4.631	1	0.917	1.357	4.631			-0.009
3	1	0	1.342	0.228	1.361	4.617							
0	6	0	0.000	1.371	1.371	4.583	0	1.37	1.370	4.586			-0.064
3	2	0	1.342	0.457	1.417	4.433							
3	3	-1	1.267	0.685	1.440	4.362	1.254	0.695	1.434	4.382			-0.465
1	6	0	0.447	1.371	1.442	4.357							
2	5	0	0.894	1.142	1.451	4.331	0.87	1.15	1.442	4.357			-0.609
1	5	-1	0.898	1.142	1.453	4.325							
3	3	0	1.342	0.685	1.507	4.171							
2	5	-1	1.003	1.142	1.520	4.134							
0	5	-1	1.003	1.142	1.520	4.133							
3	4	-1	1.267	0.914	1.562	4.022							
0	7	0	0.000	1.599	1.599	3.929							
3	4	0	1.342	0.914	1.623	3.871							
2	6	0	0.894	1.371	1.637	3.839	0.87	1.38	1.631	3.852			-0.335
1	6	-1	0.898	1.371	1.639	3.835							
1	7	0	0.447	1.599	1.661	3.783	0.435	1.603	1.661	3.783			0.017
2	6	-1	1.003	1.371	1.698	3.699	1	1.38	1.704	3.687			0.342
0	6	-1	1.003	1.371	1.699	3.699	1	1.38	1.704	3.687			0.331
3	5	-1	1.267	1.142	1.706	3.683							
3	5	0	1.342	1.142	1.762	3.566							
2	0	-2	1.795	0.000	1.795	3.500	1.81	0	1.810	3.471	64	3.47	0.825
2	1	-2	1.795	0.228	1.810	3.472							
0	8	0	0.000	1.828	1.828	3.438							
2	7	0	0.894	1.599	1.832	3.429							
1	7	-1	0.898	1.599	1.834	3.426							
3	0	-2	1.850	0.000	1.850	3.397							
1	0	-2	1.850	0.000	1.850	3.396							
2	2	-2	1.795	0.457	1.852	3.392	1.81	0.468	1.870	3.361			0.922
3	1	-2	1.850	0.228	1.864	3.371	1.86	0.24	1.875	3.350			0.615
1	1	-2	1.850	0.228	1.864	3.370	1.86	0.24	1.875	3.350			0.598
3	6	-1	1.267	1.371	1.867	3.366							
1	8	0	0.447	1.828	1.882	3.339							
2	7	-1	1.003	1.599	1.888	3.329							
0	7	-1	1.003	1.599	1.888	3.328							
3	2	-2	1.850	0.457	1.905	3.297							
1	2	-2	1.850	0.457	1.906	3.297							
3	6	0	1.342	1.371	1.918	3.276							
2	3	-2	1.795	0.685	1.922	3.270							
3	3	-2	1.850	0.685	1.973	3.185							
1	3	-2	1.850	0.685	1.973	3.184							
0	0	-2	2.006	0.000	2.006	3.132							
2	4	-2	1.795	0.914	2.014	3.119	1.81	0.917	2.029	3.097			0.725
0	1	-2	2.006	0.228	2.019	3.112							
2	8	0	0.894	1.828	2.035	3.088							
1	8	-1	0.898	1.828	2.036	3.086							
3	7	-1	1.267	1.599	2.040	3.080							
0	9	0	0.000	2.056	2.056	3.056							
0	2	-2	2.006	0.457	2.057	3.054							
3	4	-2	1.850	0.914	2.063	3.045							
1	4	-2	1.850	0.914	2.064	3.045							
2	8	-1	1.003	1.828	2.085	3.014							
0	8	-1	1.003	1.828	2.085	3.014							
3	7	0	1.342	1.599	2.088	3.010							
1	9	0	0.447	2.056	2.104	2.986	0.435	2.06	2.105	2.984			0.050

Figure 2.15: Table of observed and model BP phase I peaks with deviations in d-spacing.

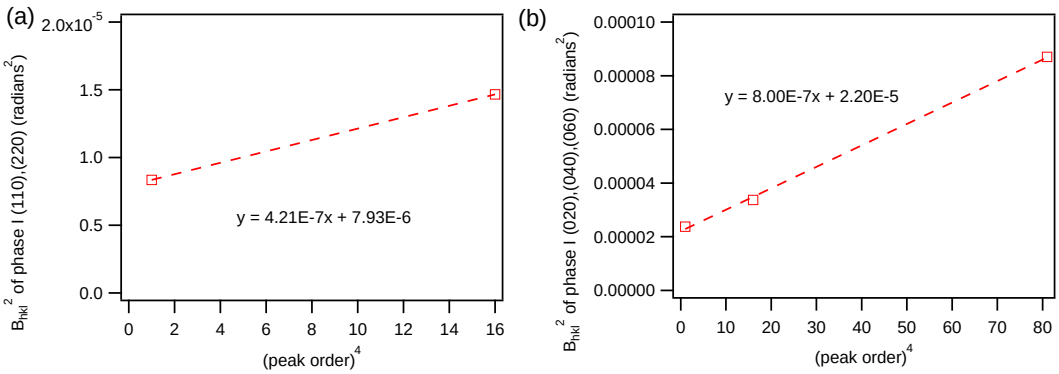

Figure 2.16: Crystallite size contribution to peak width (B_{hkl}) of (a) the (110)-order off-axis peaks and (b) the (020)-order out-of-plane peaks in BP phase I.

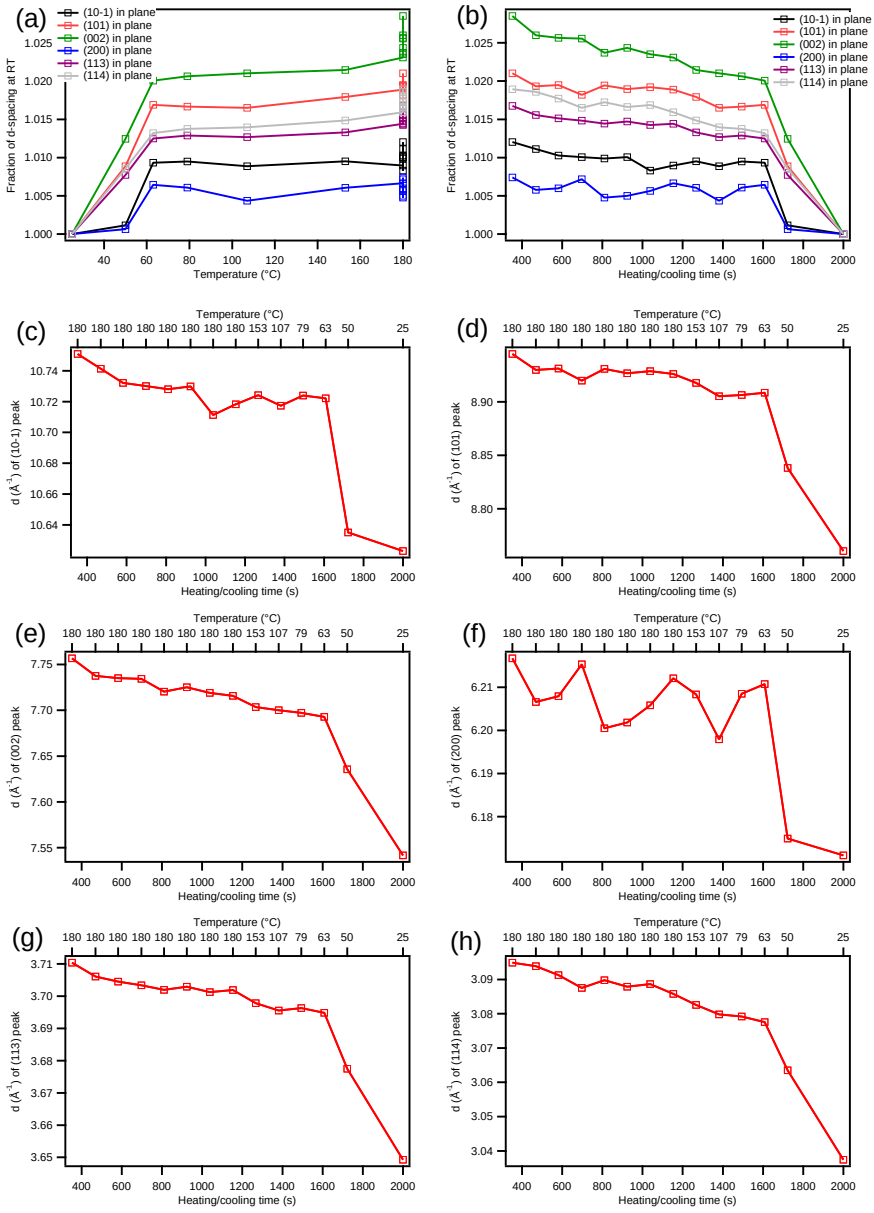

Figure 2.17: Normalized *d*-spacing of six in-plane peaks in BP phase II as a function of (a) temperature; (b) heating and cooling time; (c-h) *d*-spacing of six in-plane peaks in BP phase II as a function of heating and cooling time and temperature.

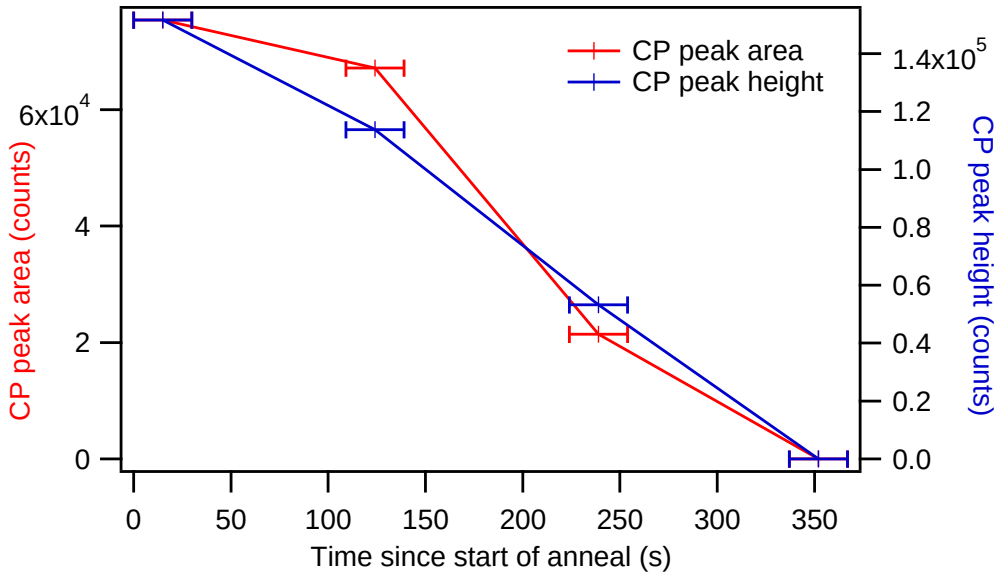

Figure 2.18: Height and area of the broad amorphous CP peak over time during in-situ heating of Si/PEDOT/CP at 180°C

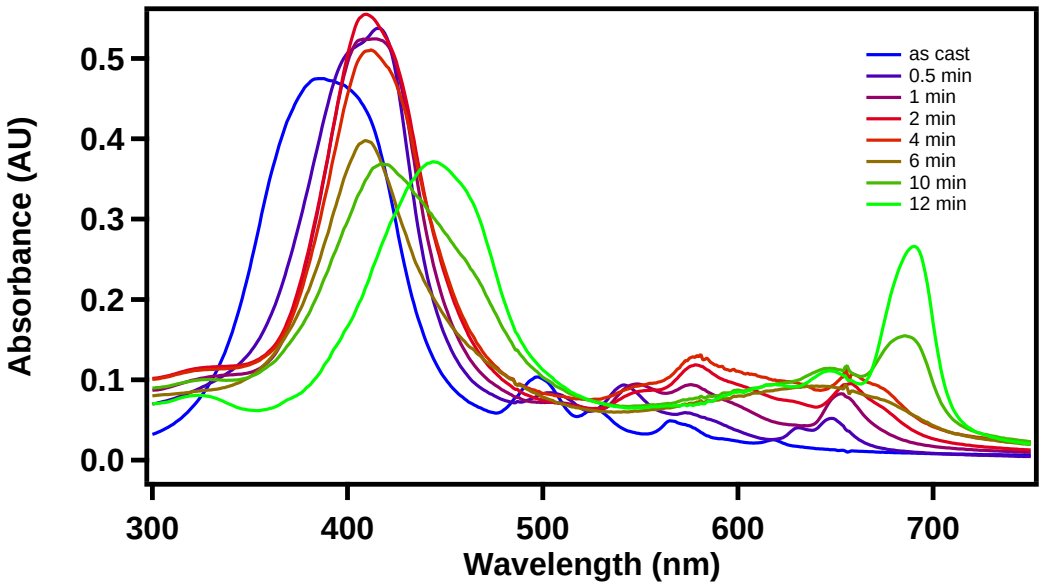

Figure 2.19: Absorption spectra of CP, BP phase I, and BP phase II with the same initial thickness after various annealing times at temperatures estimated between 167°C and 173°C.

2.2 PCBNB

The thermotropic behavior of [6,6]-phenyl-C_{61}-butyric acid n-butyl ester (PCBNB) in powder and thin film form was investigated using X-ray diffraction and transmission electron microscopy. Upon heating PCBNB powder above its glass transition temperature, an amorphous-to-crystalline transition (i.e., cold crystallization) and a subsequent melting of these crystals were observed. A thin film of PCBNB was observed to order on a simple hexagonal lattice (HEX) with the c axis preferentially oriented normal to film at an annealing temperature of 180°C, but became disordered above 200°C, consistent with the powder results. However when annealed at 160°C, the PCBNB thin film ordered on a superlattice of the HEX as indicated both by electron diffraction and high-angle annular dark field scanning TEM (HAADF-STEM) images. The formation of the HEX superlattice polymorph was independent of both solvent and substrate and could be formed both on heating from the amorphous as cast state, or by cooling from the HEX structure formed at a higher temperature. HAADF-STEM show that the superlattice corresponds to a regular deficiency of PCBNB molecules on every fifth (1 $\bar{1}$ 0 0) plane of the HEX structure.

2.2.1 Introduction

Organic electronic devices have great potential for low-cost, flexible electronics because of the ability to use simple solution-processing methods for deposition of thin films.[93] One important challenge is to fabricate organic photovoltaics (OPVs) that achieve power-conversion efficiencies comparable to traditional inorganic photovoltaics.[94–97] It has been widely accepted that the performance of organic photovoltaics is related to both molecular intrinsic electronic properties and morphological features such as phase separation and crystalline structure. Improved control of the interface between electron donors and acceptors and achievement of higher crystallinity is believed to be beneficial to improve power-conversion efficiency of OPVs.[91,98]

Fullerene derivatives are the most commonly employed electron acceptors in bulk heterojunction (BHJ) OPVs. In particular, [6,6]-phenyl-C_{61}-butyric acid methyl ester (PCBM) has been widely investigated due to its solubility in common solvents and its ability to phase separate into nanoscale domains for charge generation and extraction with most conjugated polymers.[99] Experiments have focused on the morphology of the blend (i.e., donor and acceptor) and the relationship to device performance.[67,68,94,100–103] Despite the significant progress on understanding the morphology of BHJs, less attention has been paid to the intrinsic phase behavior of the fullerene derivatives. The correlation between crystalline structure and electronic properties, for example carrier mobility, can shed light on the way to achieve the best performance through optimization.[104] In spite

of recent computer simulations[105–107] and experiments[67,108–111] the behavior of crystalline PCBM structure has not been fully resolved yet.

Previously, C_{60} fullerene molecules have been shown to be ordered on a face-centered cubic (fcc) lattice in powder and thin films at room temperature.[112–114] However the pendant group attached on C_{60} cage of PCBM induces a significant change in the phase behavior observed for C_{60}. The PCBM crystalline structure both in thin films and single crystals depends significantly upon preparation method such as choice of solvent, solvent evaporation rate, and annealing temperature.[67,108,110,111] Recently, Verploegen et al. investigated the temperature dependent growth mechanism of PCBM crystals in thin films using grazing incidence X-ray scattering.[67] The density of nucleation sites depends upon annealing temperature and determines growth mechanism and crystal orientation. In addition the PCBM crystalline structure in thin films and in single crystals upon thermal annealing was investigated systematically by Zheng et al.[110,111] They observed that the PCBM undergoes both an amorphous-to-crystalline phase transition starting from an as cast thin film (i.e., cold crystallization) and a crystalline-to-crystalline phase transformation upon heating further.

The present study focuses on the phase behavior of [6,6]-phenyl-C_{61}-butyric acid n-butyl ester (PCBNB) in powder and thin film form upon thermal annealing. PCBNB is structurally similar to PCBM but has a longer aliphatic tail (butyl vs. methyl) (Fig. 2.20). The field effect mobility of PCBNB was reported to be an order of magnitude lower than

that of PCBM.[115] However, relative to PCBM, solubility of PCBNB in common solvents is enhanced due to the longer aliphatic tail, resulting in the use of this fullerene derivative as an acceptor in some OPVs.[72–75,116] Interestingly, we observed that the small change in the molecular structure leads to remarkable difference in the phase behavior from PCBM including a decreased molecular mobility, a decrease in melting temperature, and the presence of a stable superlattice phase. Since many BHJs are thermally annealed in the temperature range where these PCBNB crystal polymorphs are observed, these polymorphs and their formation are potentially of interest for OPV applications.

2.2.2 Experimental Section

[6,6]-phenyl-C_{61}-butyric acid n-butyl ester (PCBNB, Fig. 2.20) was obtained from Mitsubishi Chemical and used as received. Poly(styrene sulfonate) and poly(3,4-ethylene dioxythiophene) (PEDOT:PSS, HC Starck) mixture in an aqueous solution was spin-coated on a silicon wafer covered by a 100–150 nm thick SiO2 layer (Silicon Quest International), then annealed at 150°C for 10 min. PCBNB in either toluene, chlorobenzene, or chloroform (ca. 12–15 mg/mL) was spin-coated on the PEDOT:PSS layer. Then the thin film was annealed at the target temperature for more than 30 min, followed by rapid cooling to room temperature.

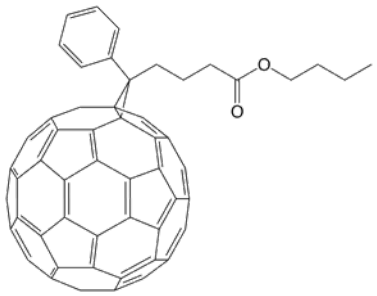

Figure 2.20: Molecular structure of [6,6]-phenyl-C_{61}-butyric acid n-butyl ester.

2.2.3 Results and Discussion

Soo-Hyung Choi in Prof. Ed Kramer's group performed XRD on PCBNB powders to identify the crystal structure of PCBNB below Tm. The Bragg peaks were indexed on a primitive hexagonal lattice with lattice constants of a = 10.01 Åand c = 10.29 Å(i.e., c/a = 1.028). The simple hexagonal lattice with a = 10.01 Åand c = 10.29 Åis intriguing. With respect to the fullerene moiety, a simple hexagonal structure has been observed for a fulleride solid ($C_{60}I_4$),[117] and has been theoretically proposed as one of the possible crystalline structures for PCBM[105] but not yet observed experimentally. However, this simple hexagonal structure is not common in materials science, even though a few materials have been reported as having this crystalline structure.[118,119] Comparing to C_{60} fullerene ordered onto an fcc lattice, these values indicate that the distance between PCBNB along the *a* axis is interestingly slightly smaller than C_{60} fullerene (= 10.08 Å),[111] and the pendant group of PCBNB is expected to be intercalated between (0 0 0 1) planes. This thermotropic

behavior and crystalline structure of PCBNB powder provides a guideline to understand the behavior of PCBNB in a thin film.

PCBNB thin films were annealed at target temperatures for at least 30 min, and were subsequently cooled rapidly to room temperature. We believe that the structural reorganization of PCBNB is so slow that the structure does not change upon reasonably rapid cooling. By referring to the powder DSC results, annealing temperatures for the thin films were chosen as 160°C, 180°C and 200°C, and the resulting thin films will be referred to as PCBNB 160, PCBNB 180, and PCBNB 200, respectively. XRD results show that the PCBNB 160 and PCBNB 180 thin films have very similar structures. Bragg peaks are indexed using a simple hexagonal lattice as observed for the powder sample (a = 10.01 Åand c = 10.29 Å). Bragg peaks of (0 0 0 h) are obtained in out-of-plane measurement, that were not observed with powder XRD measurement. Therefore, PCBNB thin films prepared by thermal annealing are highly oriented such that the *c* axis is nearly perpendicular to the substrate.

Electron diffraction by Soo-Hyung shows that the PCBNB molecules become disordered at 200°C as indicated by the broad halo. DSC results on the PCBNB powder show that melting takes place above 200°C at relatively fast heating rate (i.e., 10 °/min), but the measured value in DSC is affected by kinetics of the melting transition. The fact that PCBNB 200 thin films are not crystalline after prolonged annealing and subsequent quenching is reasonably consistent with DSC results on the PCBNB powder.

However, it is surprising that PCBNB 160 thin films show a superlattice structure as indicated by the ED pattern and a domain texture seen in the bright field image. Four weaker diffraction peaks emerge between the strong diffraction peaks that appear in the PCBNB 180 thin films. The superlattice has a structure that repeats every five (1 $\bar{1}$ 0 0) planes. The direction of the superlattice rows is parallel to [1 1 $\bar{2}$ 0] and the angle between two superlattice rows is 60°. This superlattice structure from PCBNB 160 was not detected in the thin film XRD measurements mainly due to limited resolution of the lab source X-ray system.

The superlattice structure has been observed for PCBNB thin films spin coated from different solvents such as chloroform and chlorobenzene, and then annealed at 160°C for more than 30 min. In addition, this structure has been obtained from PCBNB thin films spin coated both on PEDOT:PSS and on an SiO2 layer. Therefore, both solvent and substrate do not affect the formation of the superlattice structure. In addition to the thin film annealed at 160°C after spin casting, the superlattice structure was also observed from the thin films prepared by spin casting, heating to 230°C for an hour and annealed at 160°C for an hour. Therefore the superlattice structure is the equilibrium PCBNB crystalline structure at 160°C.

In order to obtain more detail about the crystalline structure of PCBNB, high-angle annular dark field scanning TEM (HAADF-STEM) was performed by Soo-Hyung on PCBNB 160 and PCBNB 180 thin films. HAADF images are formed from electrons scat-

tered with large scattering angles, resulting in images dominated by Z-contrast. Heavier atoms scatter more electrons, leading to a brighter image in HAADF-STEM. Therefore, brighter circles of about 1 nm diameter represent PCBNB C_{60} cages.[40] For PCBNB 180 thin films, PCBNB C_{60} cages are placed on a hexagonal lattice, consistent with the previous results. However, dark streaks were observed for the PCBNB 160 thin film, which indicates a regular deficiency of PCBNB C_{60} cages in every fifth $(1\ \bar{1}\ 0\ 0)$ plane. Therefore, this spatially regular deficiency in C_{60} cages is the origin of the superlattice structure. Furthermore, we strongly suspect that a periodic preferential orientation of the pendant butyl ester group induces the regular deficiency.

Fig. 2.21 displays 2D images of GIWAXS results obtained from PCBNB 160, PCBNB 180, and PCBNB 200 thin films. Consistent with TEM results, the PCBNB 200 thin film (Fig. 2.21c) shows a disordered state, and the PCBNB 180 thin film (Fig. 2.21b) is ordered onto a simple hexagonal lattice where the c axis is perpendicular to the substrate. The peaks are reproduced and indexed as shown in Fig. 2.21d using the simple hexagonal lattice with the lattice constant of a = 10.01 Åand c = 10.29 Å. Fig. 2.21a from the PCBNB 160 film displays weak peaks in the in-plane direction between stronger peaks, at the same q values at those observed from the PCBNB 180 thin film. These weak peaks are attributed to the superlattice structure of the PCBNB 160 thin film. It should be also pointed out that the superlattice peaks are only observed along the in-plane direction.

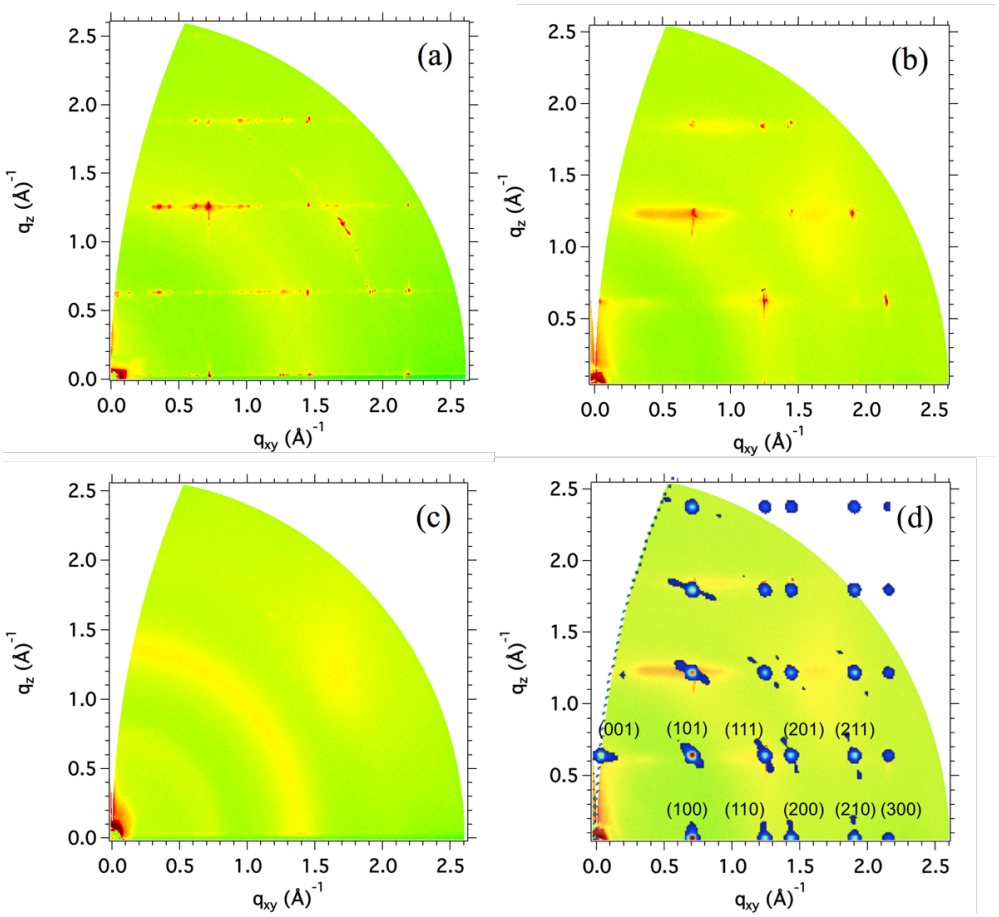

Figure 2.21: 2-D GIWAXS of (a) PCBNB 160, (b) PCBNB 180, and (c) PCBNB 200 thin films. Bragg peaks shown in (c) are indexed using simple hexagonal lattice where c axis is normal to the substrate.

Based on the ED patterns and HAADF images, we envision the superlattice structure formed by PCBNB thin film annealed at 160°C illustrated in Fig. 2.22. Twenty PCBNB molecules in simple hexagonal ordering with 5 C_{60} deficient sites provides a building block (a' = b' = 50.05 Å), that is tiled to allow the texture shown in Figure 5(a). This

structure explains that the angle between two superlattice rows is 60° as shown in Fig. 2.22 with red and green building blocks. Then the layer is stacked on top of the others with c' = 10.29 Å. Note that we do not claim that the open circles are empty, only that the probability of occupancy of these sites by C_{60} cages considerably less than 1. These sites may also contain a high concentration of butyl side chains.

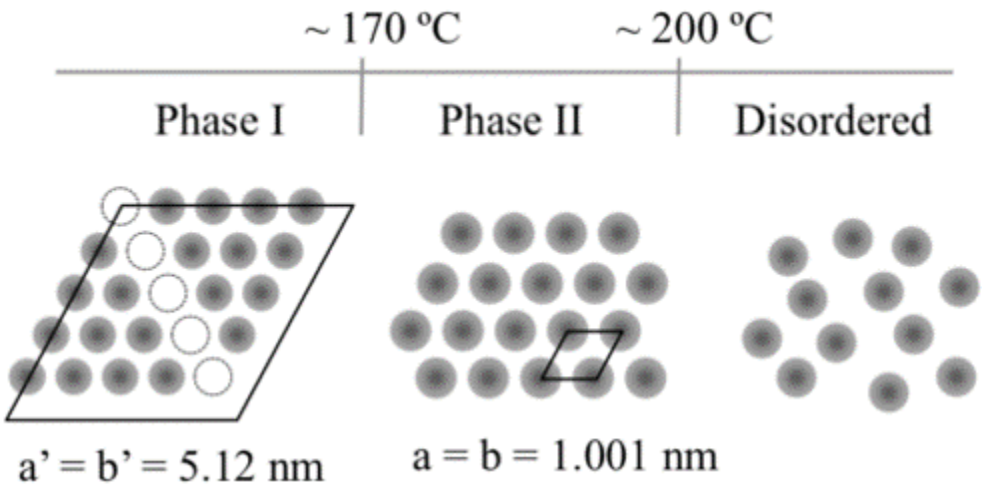

Figure 2.22: Temperature dependent phase behavior of the PCBNB thin film. Dark spheres represent PCBNB molecules, and blank ones indicate deficiency of the molecules.

2.2.4 Conclusion

In this work, the phase behavior of PCBNB molecules in both powders and thin films was investigated upon thermal annealing. Investigation of thermotropic behavior and crystalline structure of PCBNB powder provides guidance to understand the thin film

behavior. In thin films the PCBNB molecules are ordered on simple hexagonal lattice with the *c* axis perpendicular to the substrate when annealed at 180 °C below melting temperature. At the lower annealing temperature of 160°C superlattice formation with a basis of simple hexagonal ordering was observed, resulting from regular deficiency of PCBNB molecule along every fifth $(1\bar{1}\,0\,0)$ plane. These results are tentatively attributed to the orientation of the pendant group that is preferentially oriented at 160°C, but randomly oriented at 180°C due to higher thermal energy. However, other explanations cannot be excluded, so further study is necessary. Here it should be pointed out that three more methylene groups in the ester chain produce a significant difference in the phase behavior with the comparison with that of PCBM.

Chapter 3

Microstructure Control in Small Molecule OPV Devices with the Use of Binder Polymers

3.1 Introduction

Organic photovoltaics (OPV) based on bulk heterojunctions (BHJ) have efficiencies above 7%[120,121] and can be processed from solution at potentially low cost.[122] BHJs comprise a blend of an electron donor and an electron acceptor in a phase separated morphology that provides a large interfacial area for photogeneration of electron-hole pairs.[4] The highest performance OPVs currently comprise blends of semiconducting polymers and fullerenes, such as [6,6]-phenyl-C61-butyric acid methyl ester (PCBM).[123] Despite their performance in BHJs, semiconducting polymers often take many complicated steps to synthesize and may be difficult to purify.[124,125] Replacing the polymer donor with a

small molecule donor is attractive because small molecules have well defined molecular structures, exact molecular weights, and high purity.[13,126]

BHJ solar cells with efficiencies of 5.2% can be made with blends of 29H,31H-tetrabenzo[b,g,l,q]porphine, BP, and fullerene.[70,72,75] Although BP is poorly soluble in organic solvents, solution coating is enabled by a soluble precursor (1,4:8,11:15,18:22,25-tetraethano-29H,31H-tetrabenzo[b,g,l,q]porphine, CP (Fig. 3.1a) that undergoes a series of retro-Diels Alder reactions on heating to form BP. The mechanism by which this chemical process allows formation of polycrystalline films is not well understood. BP is attractive as a donor in OPVs because it has an absorption edge near 720 nm and its insolubility allows it to be used in multilayered structures, for example to form an electron blocking layer at the hole extracting electrode.

One of the barriers to the use of small molecules in BHJs is that they can be difficult to process from solution over large areas. Commercial large area solution-processed solar cells are likely to be fabricated by methods such as inkjet printing[127] and slot or blade coating[128] where the control of the viscosity of dilute solutions of small molecules is necessary.[129,130] One method to modify the viscosity of a solution of small molecules is the addition of a polymeric binder that can be removed after deposition. While the control over viscosity from a binder is beneficial, the challenge is that it cannot diminish the electronic properties of the original materials after removal.

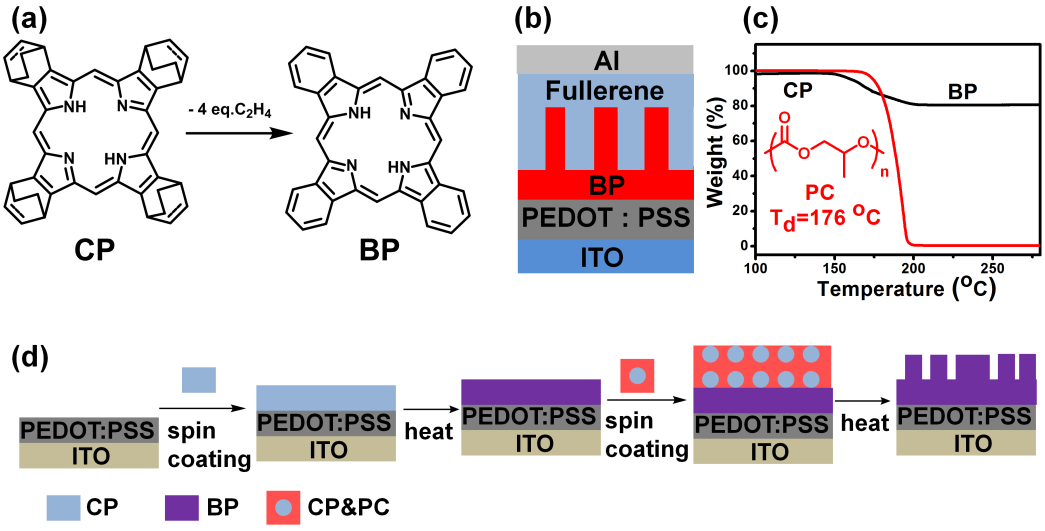

Figure 3.1: (a) Chemical transformation of BP precursor (CP) to benzoporphyrin (BP) during annealing; (b) standard BP OPV device; (c) TGA analysis of PC and CP; (d) schematic of processing method used to form films of BP for morphology analysis.

In this work, we demonstrate a method to fabricate solution-processed small molecule solar cells with the aid of a sacrificial thermally degradable binder, poly(propylene carbonate) (PC). We examine the morphological changes in films of BP formed using PC binders using a combination of grazing incidence x-ray scattering (GIWAXS) and scanning electron microscopy (SEM). These studies show that use of PC does not significantly degrade the electronic properties of BP and also helps to form nanostructured film morphologies beneficial to OPVs.

Poly(propylene carbonate) (PC) (Fig. 3.1c), derived from carbon dioxide and propylene oxide, has attracted practical interest with respect to CO_2 fixation and biodegrad-

ability.[131] The carbonate linkage in the backbone of PC results in a relatively low thermal decomposition temperature (T_d), potentially limiting its practical applications as a standalone material. However, this low T_d, coupled with decomposition to volatile small molecules, can be exploited in the design of processes involving sacrificial polymer templates.[132,133]

The incorporation of PC binder into the CP solution increases the viscosity of the solution and improves processability for large area fabrication. To evaluate the range of change in viscosity, solutions of small molecules with and without the PC binder were prepared. The solution with the binder contained a 2.0wt% blend of CP and PC (0.6:1.4 weight ratio) in a chloroform:chlorobenzene mixture (1:2 weight ratio). To compare this with the solution used to make the BHJ layer in the literature, a solution of small molecules was prepared comprising CP and a fullerene derivative instead of PC. At 25°C, the viscosity of the control solution of small molecules, 0.8 cP, is not much greater than the viscosity of the solvent mixture (about 0.7 cP). However, the viscosity of the solution with the PC binder increases to 1.6 cP. While the increase in viscosity at these low loading levels is modest, such changes are known to have significant impact on coating using inkjet printing where solutions with viscosity in the range of 1-10 cP are desirable.[130–135] The viscosity may be further increased if necessary for other printing methods, such as screen printing, by using higher concentrations of the binder. In this initial study, we

have chosen to work with the lower range of PC loading amenable to inkjet or gravure printing.

3.2 Experimental section

To test the influence of the binder on electronic properties, we used the PC binder to form simple films and photovoltaic devices in a modified version of the route that has been used to fabricate OPV devices with BP. The best photovoltaic devices with BP have been obtained using a p-i-n structure. In this nomenclature, p refers to an electron-blocking layer of pure BP, i refers to a blend of BP:fullerene, and n refers to a hole-blocking layer of pure fullerene. A BHJ photovoltaic cell with BP is made in a multi-step process. First, the soluble precursor CP is spin-coated onto a glass/ITO/PEDOT:PSS anode, then heated at 180°C to convert it to the highly insoluble, crystalline BP donor with the release of ethylene (Fig. 3.1a) to create the p-layer. Then a blend of CP and a soluble fullerene is spin-coated on top and thermally converted to create the i-layer. This heating and conversion process does not cause the fullerene to react or degrade, but does cause it to crystallize. Finally, the soluble fullerene is spin-coated on top to create the n-layer, and an Al cathode was thermally evaporated (Figure 1b). Matsuo et al. has demonstrated that photovoltaic cells formed with a BHJ of BP and SIMEF (1,4-bis(dimethylphenylsilylmethyl[60]fullerene) with a 2,9-bis(naphthalen-2yl)-4,7-diphenyl-

1,10-phenanthroline buffer layer between the n layer and Al electrode can achieve a power-conversion efficiency of 5.2%.[70] Here, we modify this process by using a PC binder in the coating of the CP precursor layers.

A critical aspect of the sacrificial polymer binder strategy is the effect of the PC binder on the morphology of BP films. To assess this effect, the p-layer and the donor component of the i-layer were fabricated through the CP:PC route. To make the p-layer, the CP solution is first spin-coated on a glass/ITO/PEDOT:PSS substrate for devices (or a Si/PEDOT:PSS substrate for morphological studies) and is thermally converted to the donor BP at 180°C (Fig. 3.1d). In the second step, a homogeneous mixture of degradable PC binder (0.25 wt%) and CP (0.75wt%) in a co-solvent of chloroform and either chlorobenzene or 2-chloroethanol is spin-coated to form the CP:PC layer. The conversion of CP to BP occurs at 180°C and is the same temperature that PC begins to decompose. Complete removal of PC requires heating to 200°C. Therefore, the samples were heated first to 180°C to convert the soluble CP precursor to insoluble BP, and then to 200°C to remove residual PC binder, resulting in a nanostructured BP layer. The resulting structure is PEDOT:PSS/BP/BP′, where BP′ denotes a layer made through the CP:PC route. The gaps in this film can be backfilled with a fullerene to form the i-layer. A second set of samples was fabricated containing only the p-layer made through the CP:PC route to investigate the effect of using the CP:PC route on top of PEDOT:PSS rather than BP as

well. The procedure used was the same as that of the i-layer, but without the underlying BP layer, resulting in a PEDOT:PSS/BP′ structure.

3.3 Results and discussion

Top-down view and cross-section SEM were used to observe the resulting morphology and nanostructure of the films. Grazing incidence wide angle X-ray scattering (GIWAXS) with 2-dimensional detection was used to study the crystal structure and texture in the BP films. BP single crystals were previously found to have a monoclinic unit cell and the P21/n space group.[49] Through GIWAXS, it was found that fully annealed PEDOT:PSS/BP/BP′ films formed by the CP:PC route as well as PEDOT:PSS/BP films formed by the standard route have this same crystal structure (see S.I.). Significantly, GIWAXS characterization was also performed on these films while annealing in situ (see S.I.), and it was shown that the sacrificial binder does not affect the final crystal structure. The texture of these films, i.e. the distribution of orientations of the crystallite domains, was also examined. First, the texture of PEDOT:PSS/BP/BP′ films made through the CP:PC route was compared to that of PEDOT:PSS/BP films made through the standard route. The intensities of the diffraction peaks with respect to angle from the vertical axis β in 2-D GIWAXS plots were nearly the same for both types of films (Fig. 3.2c and f)

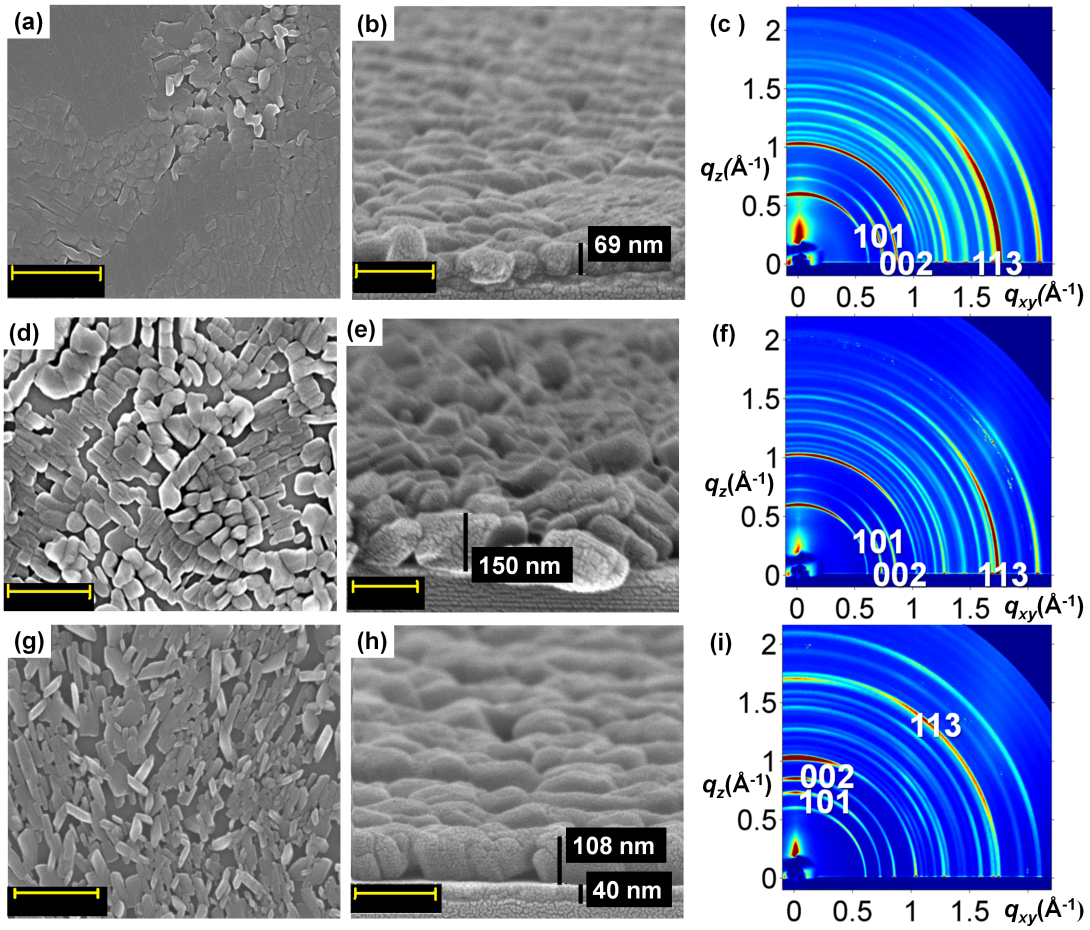

Figure 3.2: Sample A (PEDOT:PSS/BP), sample B (PEDOT:PSS/BP/BP′) and sample C (PEDOT:PSS/BP′); scale bar in top view image is 1 µm; scale bar in cross-section is 200 nm; film thicknesses obtained by SEM are approximate. (a) top view SEM of sample A; (b) cross-section SEM of sample A; (c) 2-D GIWAXS of sample A; (d) top view SEM of sample B; (e) cross-section SEM of sample B; (f) 2-D GIWAXS of sample B; (g) top view SEM of sample C; (h) cross-section of sample C; (i) 2-D GIWAXS of sample C.

While it was shown that addition of the PC binder does not impact molecular scale ordering in BP′ films, it does affect the large-scale morphology. The morphological influence of the PC binder on the PEDOT:PSS/BP/BP′ film is to create a textured nanostructure that is appropriate for BHJ solar cells. Through SEM, it was found that the vast majority of the surface consists of rectangular BP columns (ca. diameter of 50-100 nm and height of 100-150 nm) (Fig. 3.2d and e). In contrast, a film of PEDOT:PSS/BP formed by the standard route revealed two types of crystal shapes, consisting of large flat regions in the majority and smaller vertical domains in the minority (Fig. 3.2a and b), with few gaps in the film. Films of PEDOT:PSS/BP/BP also show a similar morphology, but with a slightly more ordered and uniform packing of the grains (see S.I.). The difference in morphology does not affect crystallographic texture as seen in GIWAXS; the texture is a result of the orientation of crystallites, which may not depend on the possible gaps between them. It is conjectured that the reason for the difference in morphology is that during the annealing process for a neat BP film formed by the standard route, CP transforms to BP with 20% weight loss by releasing 4 equivalents of ethylene. In direct contrast, CP:PC films undergo ca. 40% weight loss due to the additional presence of PC binder and the released small molecule mixture consisting of ethylene, CO2 and acetone. The weight loss of CP:PC films not only results in thinner films, but also disrupts and changes the morphology of the BP crystals, resulting in the desired ordered polycrystalline BP′

with nanoscale (50-100 nm) gaps between each crystallite. When the gaps between the crystallites are filled with acceptor material, the morphology forms the BHJ i-layer.

We also examined the use of CP:PC solutions to form the p-layer of the photovoltaic devices. PEDOT:PSS/BP′ films were not advantageous for the p-layer relative to films formed without polycarbonate. They have a less desirable crystal texture due to a wider range of crystallite orientations and morphology due to gaps in the film to the underlying PEDOT:PSS layer. After annealing, the integration of 2-D GIWAXS patterns of these films over all β showed crystal structures for the BP′ in these films to be the same as that of the previously mentioned films (see S.I.). However, the intensities of the diffraction peaks with respect to β show that the texture is different (Fig. 3.2i and S.I.). In PEDOT:PSS/BP′ films, the (101) and (002) rings are most intense on the qz axis of the figure (defined as β = 0°), indicating that most crystallite orientations have these planes parallel to the substrate. In comparison, for PEDOT:PSS/BP and PEDOT:PSS/BP/BP′ films, these rings are most intense on the qxy axis, indicating that these planes are perpendicular to the substrate. Because the (101) and (002) planes both contain the b-axis of the unit cell [010], a large fraction of crystallites in the latter two films have the b-axis is oriented perpendicular to the substrate. This texture is potentially beneficial for charge transport in solar cells because it has been suggested that the b-axis of BP has better hole mobility than the a- and c-axes due to π-π stacking.[23] The morphology of PEDOT:PSS/BP′ films comprises large rectangular columns of BP approximately 300 nm in width and 100 nm in height as

shown in Fig. 3.2g and h. In addition to the GIWAXS data, this also suggests that the long direction of the crystallites parallel to the surface is the b-axis. This may be beneficial for charge transport in OFETs, but the films are currently too rough to produce OFETs. Overall, the data show that for benzoporphyrin films made through the CP:PC route, the morphology and crystal texture is affected by interactions with the substrate. The base layer of PEDOT:PSS/BP in BP′ samples results in much better crystal coverage as well as smaller crystals useful for BHJ devices.

Films utilizing the BHJ morphology created as a result of the PC binder can be used to make effective solar cells that are compatible with large area fabrication methods. OPVs made with PEDOT:PSS/BP/BP′ films through the CP:PC route were fabricated and compared with devices made through the standard route (Table 3.1 and Fig. 3.3). To test the hypothesis that fullerene can be added to the nanostructured BP′ layer to produce an i-layer, PCBNB ([6,6]-phenyl-C61-butyric acid n-butyl ester) was spin-coated on top of PEDOT:PSS/BP/BP′ samples and annealed, and finally thermal evaporation was used to deposit an aluminum electrode, resulting in the p-i PEDOT:PSS/BP/BP′:PCBNB/Al structure. In another set of devices, the BP′ layer was treated as an additional p-layer and therefore a standard i-layer of CP:PCBNB was spin coated on top and thermally converted, and finally aluminum was deposited, resulting in the p-i PEDOT:PSS /BP /BP′ /BP:PCBNB /Al structure. Samples spun from two different co-solvent blends were also tested. These two types of devices were compared to the standard p-i and p-i-n control

BP-based solar cells, made by starting with PEDOT:PSS/BP followed by spin-coating an i-layer of CP:PCBNB on top and thermally converting, optionally spin-coating an n-layer of PCBNB, and depositing aluminum.

Type	Structure	Route	V_{oc}[V]	J_{sc}[mA/cm^2]	FF	PCE[%]
p-i	BP/BP′:PCBNB	CP:PC[a]	0.57	4.33	0.46	1.12
p-i	BP/BP′:PCBNB	CP:PC[b]	0.54	5.15	0.48	1.35
p-i	BP/BP′/BP:PCBNB	CP:PC[a]	0.60	4.67	0.42	1.19
p-i	BP/BP′/BP:PCBNB	CP:PC[b]	0.55	5.12	0.51	1.43
p-i	BP/BP:PCBNB	Standard	0.58	5.48	0.49	1.54
p-i-n	BP/BP:PCBNB/PCBNB	Standard	0.41	5.45	0.60	1.34

Table 3.1: Device parameters of solar cells made through the CP:PC and standard routes (average of five devices each). (a) The CP:PC solution was prepared with 2:1 by volume of chloroform:2-chloroethanol; (b) The CP:PC solution was prepared with 2:1 by volume of chlorobenzene:chloroform.

The efficiencies (1.35%) of p-i devices where BP′:PCBNB was the i-layer were only slightly below those of the p-i control devices made by the standard route (1.54%). By approximating the behavior of these devices with the Hecht expression,[136] it was determined that they had similar mobility-lifetime ($\mu\tau$) products of 5.5×10^{-10} cm^2/V and

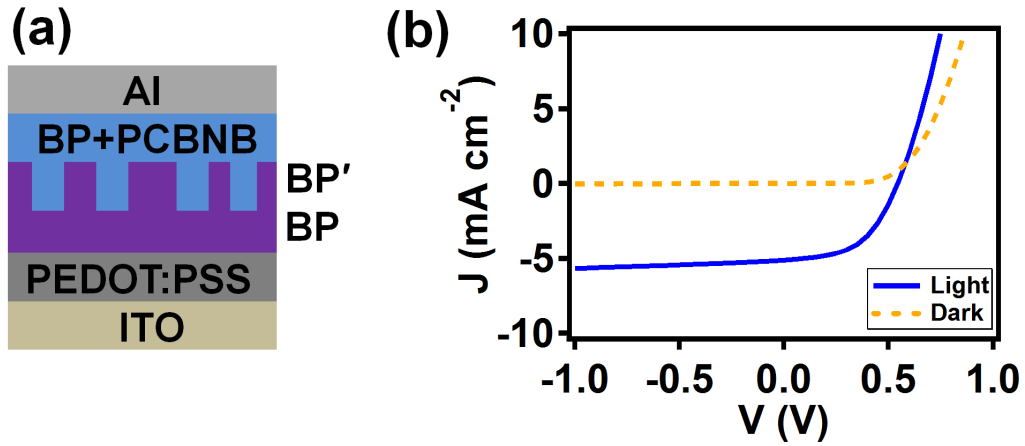

Figure 3.3: (a) BP OPV device made through the CP:PC route; (b) J-V curve of device type PEDOT:PSS/BP/BP′/BP:PCBNB/Al (chlorobenzene:chloroform) in Table 1, tested under 1 sun and AM 1.5. J-V curves of other devices are in Fig. 3.6.

5.0×10^{-10} cm^2/V respectively suggesting similar electronic properties in both cases. Devices in which CP:PC was spun from chlorobenzene:chloroform (CB:CL) were more efficient than devices in which CP:PC was spun from chloroform:2-chloroethanol (CL:CE). However, the morphology of the two observed by SEM was similar (see S.I.). These results demonstrate that the CP:PC route can be used to make OPV devices without sacrificing efficiency. Besides viscosity control, another advantage of using this route to create an i-layer is increased flexibility when adding the fullerene derivative or other acceptor. It does not require the acceptor to be annealed, increasing the potential range of solvents for the acceptor, and causes the BHJ feature size to be independent of the choice of acceptor.

Similar morphologies can be formed with different acceptors simplifying the evaluation of new materials. The efficiency is sensitive to the solvent used for casting.

The strategy of treating BP′ as an additional p-layer and adding a standard i-layer of BP:PCBNB to form a PEDOT:PSS/BP/BP′/BP:PCBNB/Al device was also examined. These devices had similar efficiency (1.43%) to PEDOT:PSS/BP/BP′:PCBNB/Al devices where BP′:PCBNB was the i-layer (1.35%). Through SEM, it was found that these devices exhibited a BHJ that contained both a larger and a smaller feature size (about 100 nm from BP′ and 20 nm from BP:PCBNB). The morphology consists of smaller columnar nanostructures due to the BP:PCBNB, on top of larger rectangular crystallites due to the BP′ (see S.I.). Interestingly, when an n-layer consisting of PCBNB is added to the control p-i devices to form p-i-n devices, the efficiency actually goes down (1.54% to 1.34%). Because the total device thickness remains the same and the short circuit current remains the same, this difference is due mainly to the difference in the open circuit voltage, Voc. Examination of the dark current shows that these devices have larger forward bias currents than the others causing a reduction in Voc. The origin of the differences likely lies in the energetic line-up at the aluminum electrode, but cannot be resolved from the studies here.

It is important to note that the insulating PC binder could easily diminish device efficiency and hole transport properties if it did not completely degrade. However, the J_{sc} of devices made by the CP:PC route reached 5.1 mA/cm^2, which is comparable to the J_{sc}

of devices made by the standard route. This observation suggests that after the annealing process and deposition of the fullerene that there is no residue from the PC binder in the BP′ film to impede charge carrier generation.

3.4 Conclusion

In conclusion, this work has shown that a thermally degradable binder strategy in processing solar cells based on small molecule donors and fullerene acceptors results in improved process control without sacrificing efficiency. A poly(propylene carbonate) binder allowed control of the solution viscosity without harming optoelectronic performance. Significantly the use of PC does not change the crystal structure or texturing of benzoporphyrin relative to the neat benzoporphyrin film, but it does result in increased nanoscale texturing and surface area that is desirable for subsequent deposition of a fullerene-based acceptor. Besides controlling viscosity, another advantage of using a decomposable binder such as PC to form a BHJ is increased flexibility in the choice and processing of the acceptor. One drawback of this method is that it currently requires an underlying BP layer fabricated from a lower viscosity solution, to alleviate roughness and gaps in the film. But the use of other decomposable polymers such as poly(acetaldehyde) and the optimization of polymer:BP phase separation could eliminate this requirement. Most importantly, photovoltaic devices with this BHJ exhibit comparable performance

to the previously used method of simply mixing the BP and PCBNB suggesting that the decomposable binder does not degrade photovoltaic power conversion efficiency.

3.5 Supporting Information

Solution Preparation:

CP (1,4:8,11:15,18:22,25-tetraethano-29H,31H-tetrabenzo[b,g,l,q]porphine, i.e. bicycloporphyrin) and PCBNB ([6,6]-phenyl-C61-butyric acid n-butyl ester) were obtained from Mitsubishi Chemical. PC (poly(propylene carbonate)) was obtained from Novomer. TGA was conducted on the PC and BP precursor. Solutions of 7 mg/mL CP in a co-solvent of 2:1 chlorobenzene:chloroform, as well as 2:1 chloroform:2-chloroethanol, were prepared. Solutions of 7.5 mg/mL CP and 2.5 mg/mL PC in both of these co-solvents were also prepared. Solutions of 6 mg/mL CP and 14 mg/mL PCBNB in 1:1 chlorobenzene:chloroform were prepared. Finally, solutions of 12 mg/mL PCBNB in toluene were prepared. Viscosity measurements were conducted with an RE-80L viscometer (TOKI SANGYO CO., LTD.)

Film Preparation: Glass/ITO (indium tin oxide) and Si substrates were sonicated in acetone, soap and DI water, DI water, and isopropanol for 20 minutes each. PEDOT:PSS (poly(3,4-ethylenedioxythiophene)-poly(styrenesulfonate), brand name Clevios PH) was obtained from H.C. Starck and spin coated onto glass/ITO substrates at 4500 rpm to form

films about 40 nm thick. CP films (about 20 nm thick from chlorobenzene:chloroform and about 40 nm thick from chloroform:chloroethanol) were spin-coated in a glovebox at 1500 rpm speed onto Si and glass/ITO/PEDOT:PSS substrates. The films were annealed in a glovebox for 20 minutes at 180°C to thermally decompose the CP to BP (29H,31H-tetrabenzo[b,g,l,q]porphin, i.e. benzoporphyrin). CP:PCBNB films about 110 nm thick were spin-coated at 1500 rpm speed and annealed for 20 minutes at 180°C. CP:PC films about 130 nm thick were spin-coated at 1500 rpm speed and 500 acceleration and annealed for 20 minutes at 180°C, then for 20 minutes at 200°C, to transform CP to BP′ and thermally decompose the PC without residue. PCBNB films were spin-coated at 1500 or 3000 rpm speed and dried for 10 minutes at 65°C.

Device Fabrication and Testing: On the glass/ITO/PEDOT:PSS/active layer samples, the PEDOT:PSS and active layer were scraped off on one side to allow Al to deposit on the ITO electrode. 90 nm of Al was thermally evaporated using a mask, creating 5 top contact pixels and a bottom contact to the ITO. The devices were placed in a solar simulator in a glovebox and tested under 1 sun and in the dark to obtain J-V curves.

Sample Characterization: Film thicknesses were measured by profilometry. Absorption spectroscopy was conducted on samples with glass substrates at various annealing times. Top-down and cross-section SEM were conducted on samples with Si substrates using an FEI XL30 Sirion FEG microscope. 2-D grazing incidence wide angle X-ray scattering (GIWAXS) on the 11-3 beamline at the Stanford Synchrotron Radiation Light-

source (SSRL) was conducted on samples with Si substrates. The WxDiff program and the GIXD Analysis Routine for Igor Pro were used to analyze GIWAXS data.

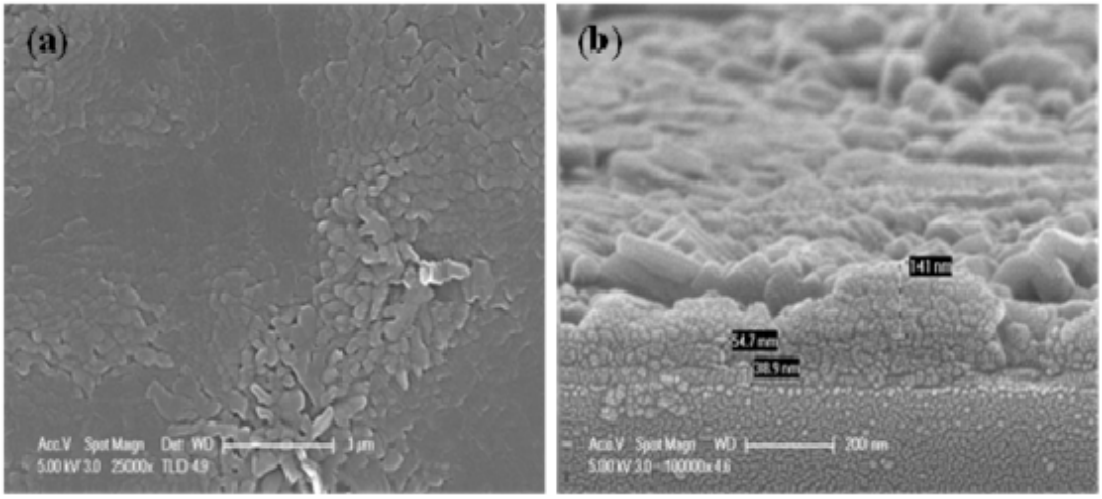

Figure 3.4: Control sample made through the standard route (PEDOT:PSS/BP/BP) (a) SEM top view; (b) SEM cross-section.

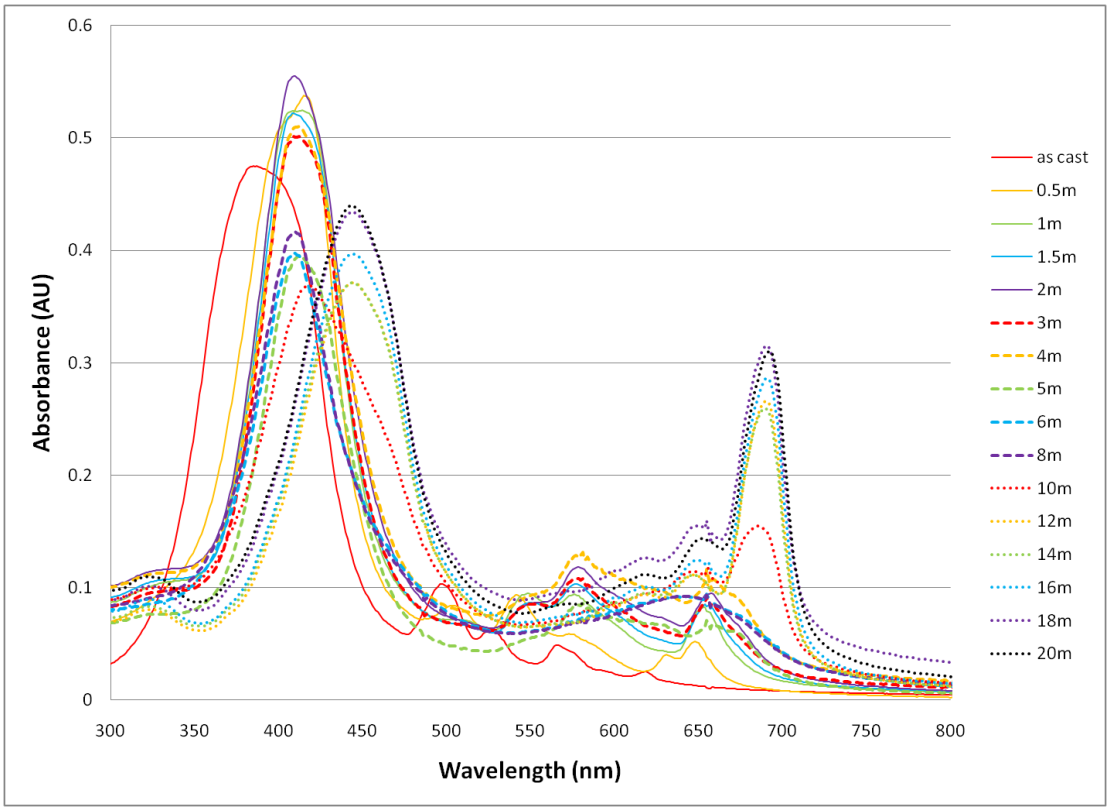

Figure 3.5: UV/Vis absorption spectra of the progression from CP to BP on glass substrates after different annealing times at 180°C.

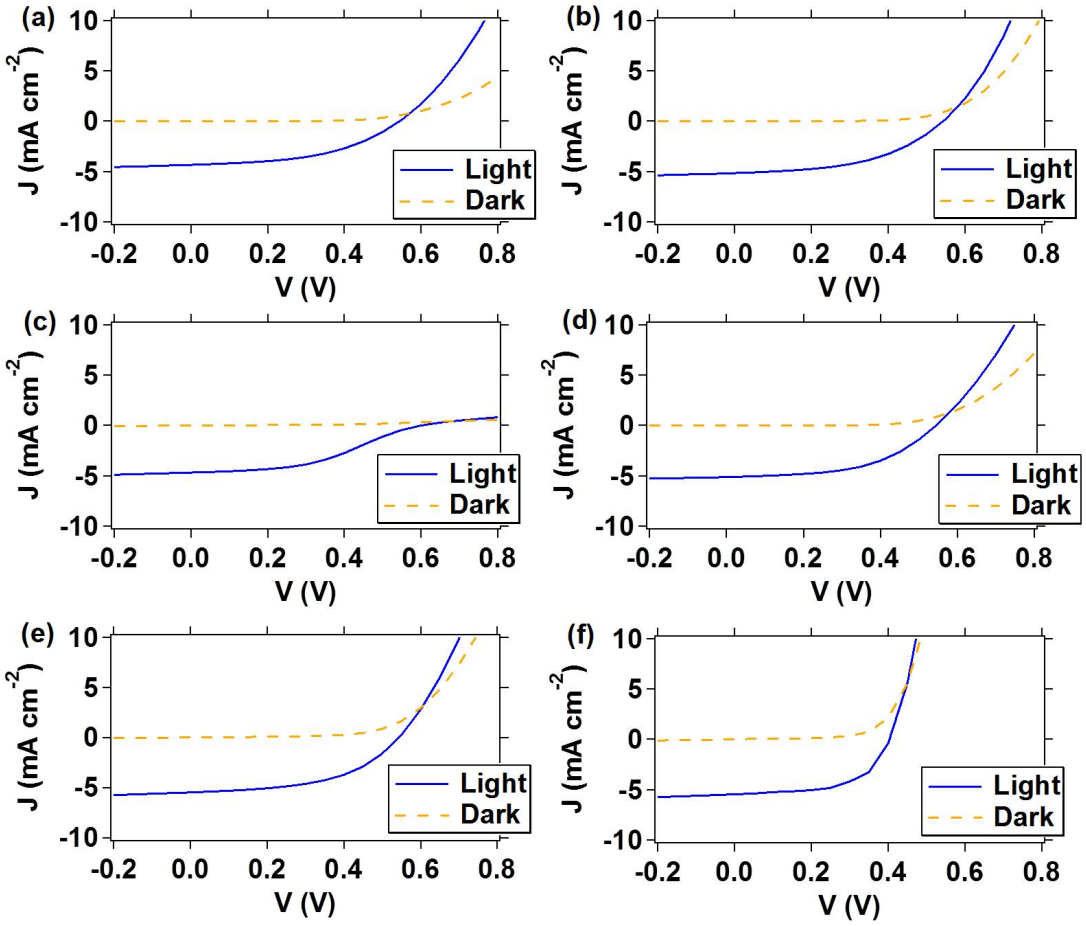

Figure 3.6: J-V curves of the devices in Table 3.1. (a) PEDOT:PSS /BP /BP′:PCBNB / Al (CL:CE); (b) PEDOT:PSS /BP /BP′:PCBNB /Al (CB:CL); (c) PEDOT:PSS /BP /BP′ /BP:PCBNB /Al (CL:CE); (d) PEDOT:PSS /BP /BP′ /BP:PCBNB /Al (CB:CL); (e) PEDOT:PSS /BP /BP:PCBNB /Al; (f) PEDOT:PSS /BP /BP:PCBNB /PCBNB /Al.

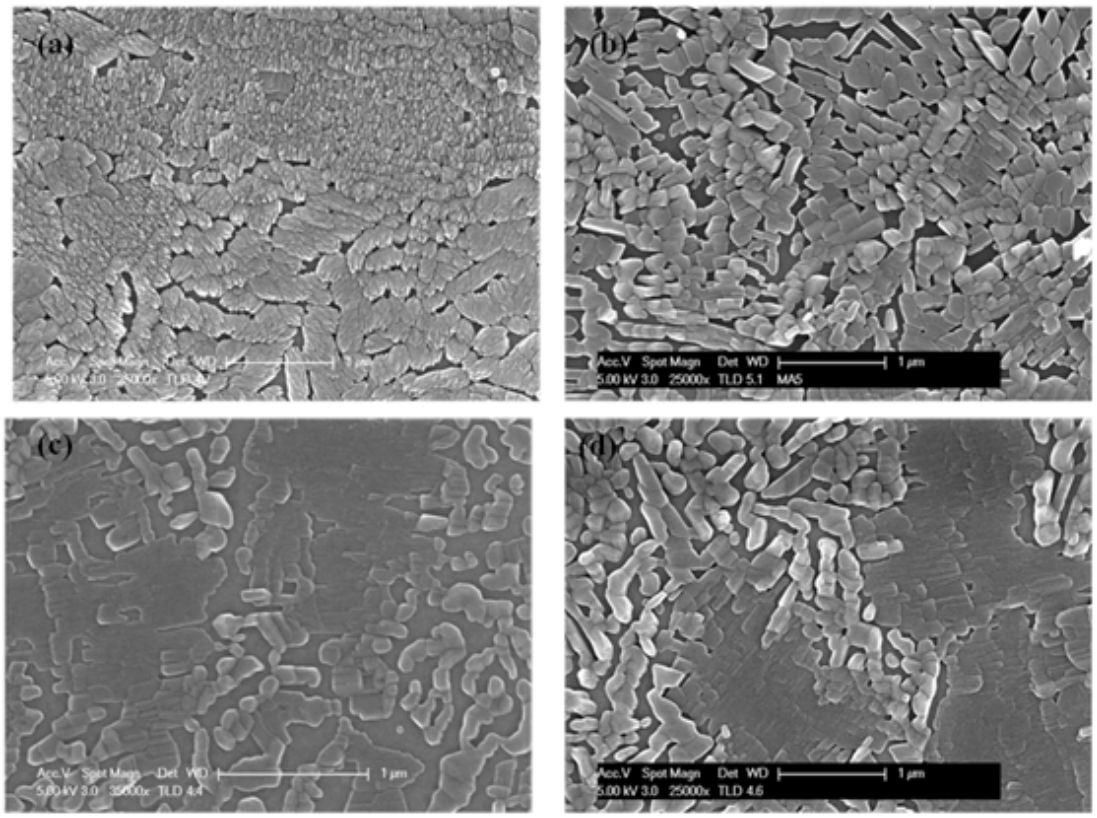

Figure 3.7: (a) SEM top view of sample PEDOT:PSS/BP/BP′/BP:PCBNB before Al contact deposition and with PCBNB removed by toluene rinse; (b) SEM top view of sample PEDOT:PSS/BP/BP′ spin-coated from 2:1 CB:CL; (c) SEM top view of sample PEDOT:PSS/BP′ spin-coated from 2:1 CB:CL; (d) SEM top view of sample PEDOT:PSS/BP/BP′ spin-coated from 2:1 CB:CL.

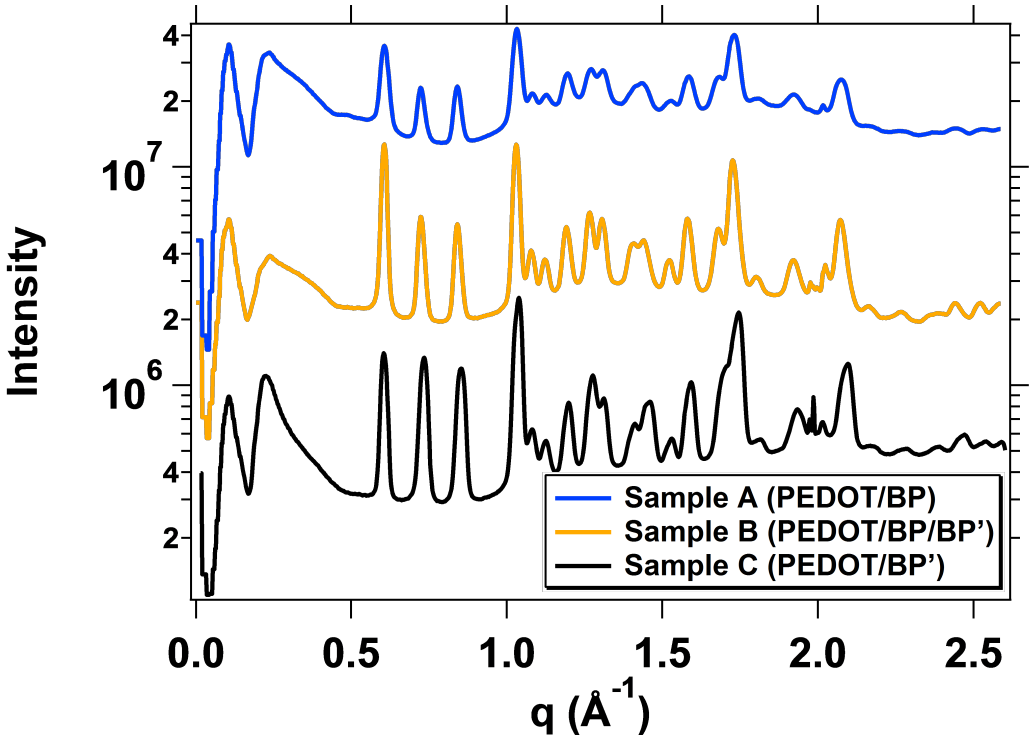

Figure 3.8: Integration of 2-D GIWAXS figures in Fig. 3.2 (c), (f), and (i) over all β to yield intensity vs. q. The peak positions are all the same and the intensities are nearly the same, which shows that these films all adopt the same structure. Comparison with known diffraction data shows that this is the monoclinic, P21/n structure reported previously.

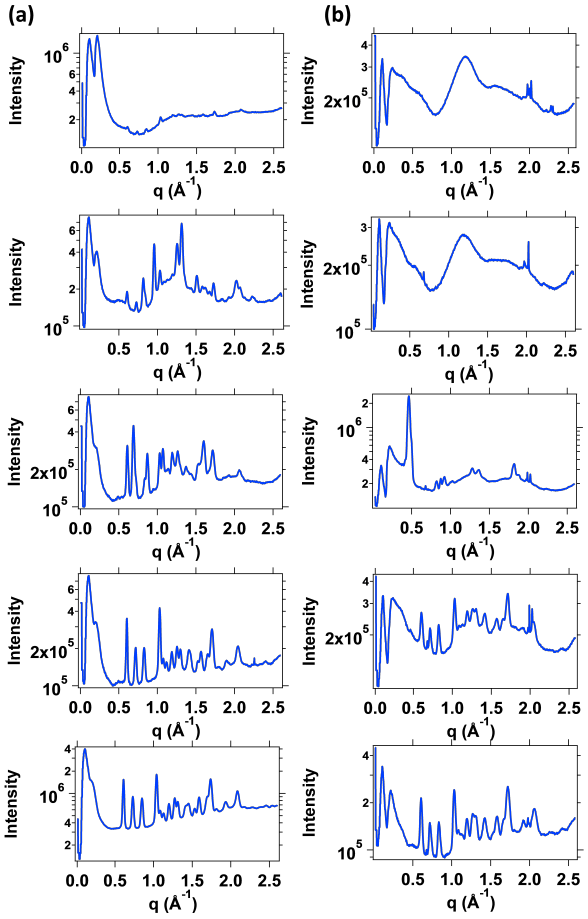

Figure 3.9: (a) GIWAXS plots of a film made through the CP:PC route during in-situ annealing at 180°C, progressing from Si/BP/CP:PC to Si/BP/BP′. (b) GIWAXS plots of a film made through the standard route during in-situ annealing, progressing from Si/CP to Si/BP. From top to bottom: as cast, after 2 minutes, after 4 minutes, after 6 minutes, after cooling. The very sharp peaks near $q = 2$ Å^{-1} are due to the Si substrate and parasitic scattering. These data show that both routes produce films with the same end structure.

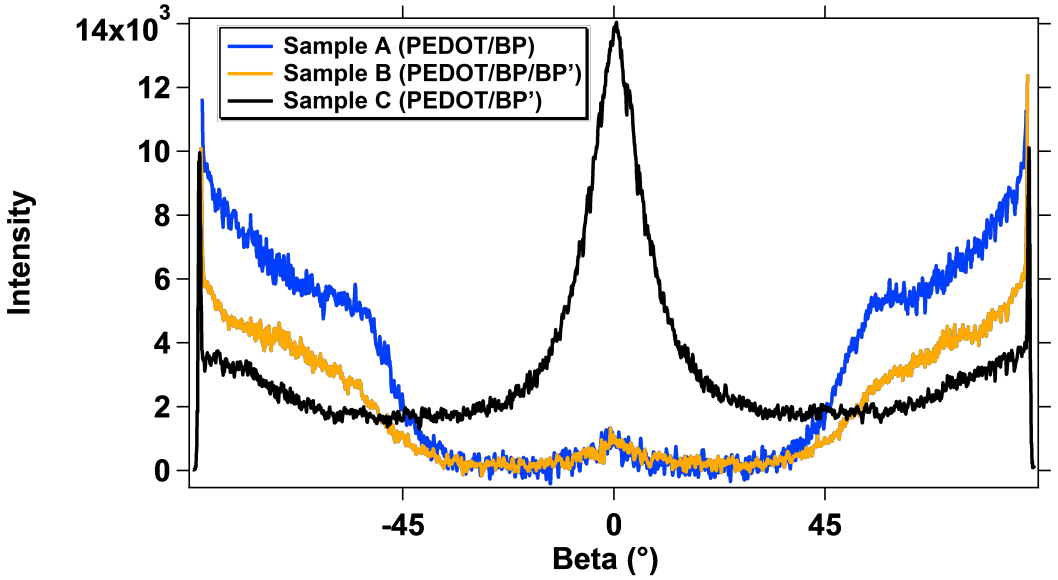

Figure 3.10: Integration of the (002) rings of the 2-D GIWAXS figures in Fig. 3.2 (c), (f), and (i) over q to yield intensity vs. β. Here q_z is at 0° and q_{xy} is at +/- 90°.

Chapter 4

Controlling Interface and Charge Transfer States in Small Molecule OPV with Pure Domains

Charge transfer (CT) states at the interface of the donor and acceptor play a crucial role in photocurrent generation and recombination in organic solar cells. In this work, we use external quantum efficiency (EQE) measurements to non-destructively characterize CT states in small molecule solar cells composed of the donor BP and the acceptor PCBNB. By varying annealing temperature and the donor-acceptor ratio, we control the columnar morphology and interfacial area between the donor and acceptor. We demonstrate that the height of the CT peak in EQE spectra can be used to approximate interfacial area. We observe that the height of the CT peak in EQE spectra varies over an order of magnitude with processing, while the energy of the CT peak remains relatively constant despite differences in the interface at the molecular level. The Urbach energy of the CT peak is slightly lower for samples with more interfacial area suggesting that in these samples

there is less disorder. With the assumption that the sub-bandgap IQE is similar to the above-bandgap IQE we calculate the oscillator strength of a CT state. Finally, using a model of Förster resonance energy transfer between chromophores within our active layer films, we calculate bounds for the components of EQE and for the exciton binding energy.

4.1 Introduction

Organic photovoltaics (OPVs) are a technology for renewable energy that have rapidly increased in efficiency in the past few years. A continuing challenge for improving efficiency is the need to better understand the morphological and electronic properties of these devices, especially in a way that is low-cost and non-destructive. Charge transfer (CT) states at the interface of the donor and acceptor play a crucial role in photocurrent generation and recombination in these devices, and need to be better understood. In this work we use external quantum efficiency (EQE) measurements to non-destructively characterize CT states, and we quantify the impact of processing on CT state density and donor-acceptor interfacial area. The charge transfer peaks of the EQE spectra show much greater changes with sample preparation than the main absorption peaks, which is helpful in characterization and optimization of OPVs.

Charge transfer (CT) states in organic solar cells are electronic energy states in which a hole in the donor material and an electron in the acceptor material have overlapping wave functions and are bound to each other. They are an intermediate state between the generation of Frenkel excitons in the donor or acceptor and migration to a donor-acceptor interface on one hand, and separation into free charges in the donor and the acceptor on the other. The formation and separation of CT states is a crucial step in charge generation, during which recombination may occur. But CT states can also be generated directly by absorbing light which has an energy lower than the band gaps of both the donor and acceptor, and we observe the current extracted from these states in EQE spectra at sub-gandgap energies.

CT states have been studied extensively in the literature. There are two main interpretations of the shape of the sub-bandgap EQE and absorption. One is that the Gaussian-like shape of the sub-bandgap EQE can be explained by electron-phonon interactions (the Franck-Condon principle) with the peak of the curve centered at the zero-phonon CT state energy plus the coupling or reorganizational energy. Marcus theory allows one to fit EQE curves to obtain physical parameters such as the CT state energy, reorganizational energy, and a factor which combines internal quantum efficiency (IQE), CT state density, and the CT absorption cross section.[137,138] Sub-bandgap EQE and electroluminescence measurements have been used to study the dark saturation current and the losses in V_{oc} due to radiative and non-radiative recombination.[139,140] The fits resulting from this

interpretation generally only fit well at photon energies below the sub-bandgap EQE peak.

The other interpretation is that the disorder in the film, characterized by exponential tails in the density of states of the acceptor below its LUMO and of the donor above its HOMO, dominates over electron-phonon interactions.[141] In this interpretation, the shape below the CT state energy is an exponential Urbach tail. The EQE and CT state absorption above and below the CT state energy can be modeled by an integral over the density of states of the donor and acceptor, multiplied by the matrix element and interfacial volume. A disordered dispersive transport model also fits transient photocurrent data. We examine both interpretations of the EQE shape using our data.

Finally, an empirical fit of the EQE composed of the sum of an exponential for disorder and three Gaussians for the absorption of the CT state and for the donor and acceptor seems to fit most of the EQE curve well in a P3HT:PCBM system, suggesting that it is likely that both coupling and disorder are significant.[142] While this is a good fit to the EQE down to a certain energy, a comparison to EQE data of the same system at lower energies suggests that this fit predicts an EQE that is too high at lower energies.[138,141]

Unlike typical polymer-fullerene bulk heterojunctions that are composed of mixed domains as well as pure domains of donor and acceptor, we study a small molecule system with only pure domains of donor and acceptor. The donor is insoluble once annealed, so the acceptor is rinsed off to view the interfacial area with atomic force microscopy

(AFM), grazing-incidence small-angle X-ray scattering (GISAXS), and cross-sectional scanning electron microscopy (SEM). This lets us verify that the interfacial area and CT state density, measured by the EQE CT peak, are correlated. By varying the annealing temperature and donor-acceptor ratio, we easily control both the amount of interfacial area and the CT state density.

The donor material we use is the insoluble semiconducting small molecule tetrabenzoporphyrin (BP), which is thermally converted from the soluble precursor bicycloporphyrin (CP).[49,50] BP has been used to make solution processed organic solar cells with power conversion efficiencies (PCE) up to 5.2%.[70] The insolubility of the BP once it is annealed has allowed for the use of a multilayered device structure, with an electron-blocking layer of pure BP, a heterojunction layer of BP and fullerene derivative, and a hole-blocking layer of pure fullerene derivative. This stack has a more ideal morphology[33] than a single layer bulk heterojunction, as the heterojunction layer is composed of column-like structures of BP and fullerene, allowing for more continuous pathways between the interface and the electrodes while retaining a large interfacial area (Fig. 4.1). While controlling the morphology of a pure BP layer using different annealing temperatures has been studied,[71] no similar work has been done on controlling the morphology of the heterojunction layer. Previously, we have explored the use of thermally degradable polymers to increase solution viscosity and improve processability of BP devices,[74] as

well as the changes in molecular ordering that take place during the thermal conversion between the metastable phase I and the stable phase II of BP.[143]

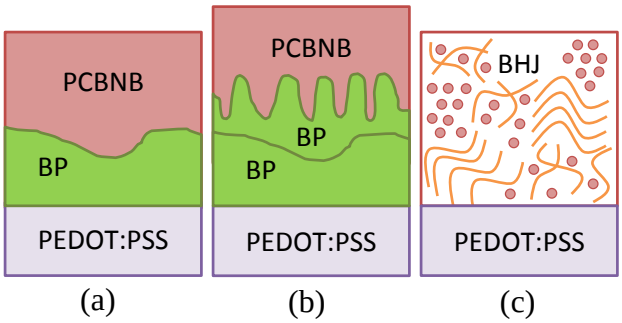

Figure 4.1: Device structures of solar cells: (a) BP/PCBNB rough bilayer, (b) BP/BP:PCBNB columnar heterojunction with pure domains, (c) typical polymer-fullerene bulk heterojunction with pure and mixed domains.

We further analyze CT states in our system by calculating above-bandgap IQE as a function of energy, from the EQE, absorption spectroscopy, thickness measurements, and a transfer matrix optical model. Absorption spectroscopy is not sensitive enough to measure sub-bandgap photon energies, so we can assume that the efficiency of exciton migration to an interface is near 1, so that the sub-bandgap IQE in each sample is almost the same as the above-bandgap IQE, which has been observed to be the case in other work.[141] This lets us calculate the CT state density and the oscillator strength of a CT state. Finally, we attempt to calculate the exciton migration efficiency by using kinetic Monte-Carlo algorithms to simulate Förster resonance energy transfer between chromophores within our active layer films, letting us calculate a more accurate sub-bandgap IQE and

thus CT state density and oscillator strength. The low oscillator strength of CT states compared to Frenkel excitons, as well as their lower density, contribute to the sub-bandgap EQE being several orders of magnitude less than the above-bandgap EQE.

4.2 Experimental section

CP (1,4:8,11:15,18:22,25-tetraethano-29H,31H-tetrabenzo[b,g,l,q]porphine) powder was obtained from Mitsubishi Chemical. PCBNB ([6,6]-phenyl-C61-butyric acid n-butyl ester) powder was obtained from Solenne. The following solutions were fabricated: 7 and 14 mg/mL of CP in a 2:1 volume ratio of chorobenzene:chloroform, 20 mg/mL of PCBNB in 1:1 chorobenzene:chloroform, and CP:PCBNB blends with a total concentration of 20 mg/mL in 1:1 chlorobenzene:chloroform and 10 wt%, 20 wt%, 30 wt%, and 40 wt% CP. ITO (indium tin oxide) substrates were used for electrical testing, AFM, and reflectance of solar cells, and silicon substrates were used for SEM and GISAXS. Substrates were cleaned by sonication in deionized water and Alconox detergent for 20 minutes, then deionized water for 20 minutes, then acetone for 20 minutes, and finally isopropanol for 20 minutes.

The substrates were then cleaned with air plasma to enable better wetting of PEDOT:PSS. PEDOT:PSS (poly(3,4-ethylenedioxythiophene)-poly(styrenesulfonate)) (brand name: Clevios P VP AI4083) was filtered with a 0.45 μm PVDF filter and spin coated at

4000 rpm onto clean substrates to form the 35 nm anode and annealed on a hot plate at 150°C for 20 minutes. The samples were transferred to a nitrogen glovebox and pure CP solution was spin coated at 1500 rpm and annealed at 180°C for 20 minutes. This converts the CP to the BP (29H,31H-tetrabenzo[b,g,l,q]porphyrin) electron blocking bottom layer. Then for the acceptor or columnar heterojunction top layer, PCBNB solution or a CP:PCBNB blend was spin coated at 1500 rpm and annealed at either 200°C for 20 minutes, or at 150°C for 4 hours. All solutions in chlorinated solvents were filtered with 0.45 μm PTFE filters directly onto the samples. For solar cell samples, on one edge of each sample, the organic layers were removed to expose the ITO and 80 nm of Al was deposited with a thermal evaporator and a patterned mask to form the cathode.

For GIWAXS, GISAXS, AFM, and SEM, some of the samples were first immersed in toluene for about 1 minute to dissolve and remove the PCBNB but not the insoluble BP. 2-D GIWAXS was performed at beamline 11-3 of the Stanford Synchrotron Radiation Lightsource at the SLAC National Accelerator Laboratory and analyzed with the wxdiff software. A photon energy of 12.7 keV, a detector distance of 400 mm, and an incidence angle of 0.12° was used. 2-D GISAXS was performed at beamline 7.3.3 of the Advanced Light Source at Lawrence Berkeley National Laboratory and analyzed with the Nika software.[144] A photon energy of 10 keV, a detector distance of 4000 mm, and an incidence angle of 0.14° was used. AFM was performed with an Asylum MFP-3D system. Cross-sectional SEM was performed with an FEI XL30 Sirion FEG system.

The current density-voltage curves of the solar cells were measured using a 300W xenon arc lamp to closely match the AM 1.5 solar spectrum. EQE was measured using the same lamp and a monochromator with about a 10 nm wavelength width. Measuring EQE with low noise for a large dynamic range was accomplished through using a lock-in technique, a reference photodiode to compensate for light intensity fluctuations over time, and through changing amplifier sensitivities. The 300W xenon arc lamp was connected to a chopper synchronized with two lock-in amplifiers. The light from the chopper went into a monochromator and was then split between the sample and the reference silicon photodiode. The currents from the sample and the reference each were connected to a transimpedance preamplifier and then to a lock-in amplifier. The sample preamplifier was set to a higher sensitivity at wavelengths where low device currents were expected. The photon flux for each incident wavelength was measured by using calibrated Si and InGaAs photodiodes as samples.

UV-Vis reflectance spectroscopy was performed on the solar cells with a Perkins Elmer Lambda 750 spectrometer with an integrating sphere to obtain the fraction of incident light absorbed by each solar cell, since all of the incident light is either absorbed or reflected. IQE was calculated by dividing the measured EQE by the fraction of light absorbed by the device. IQE' was calculated by dividing the measured EQE by the fraction of light absorbed by the active layers (the pure BP layer and the PCBNB or heterojunction layer). This fraction was found following the method of Burkhard et al.[22] We took

the measured fraction of incident light absorbed by the solar cell, which includes active layer absorption and parasitic absorption by the electrodes, and subtracted the parasitic absorption, which was calculated using transfer matrix model software[23] from the real and imaginary indices of refraction of each layer from literature and the approximate thickness of each layer in the solar cells.

4.3 Results and discussion

4.3.1 Physical characterization

The BP/BP:PCBNB samples were soaked in toluene to remove the PCBNB but not the insoluble BP. We show that this process removes all the PCBNB by comparing 2-D GIWAXS diffraction patterns of the samples before and after soaking (see SI). Before soaking, diffraction from both crystalline phases are seen, and after soaking, the diffraction from crystalline PCBNB is no longer present while diffraction from BP is unchanged.

Cross-sectional SEM on the samples with PCBNB removed show that in the films with 30 wt% BP in the heterojunction layer, BP forms column-like structures about 20 nm in width (Fig. 4.2), similar to the morphology observed in the literature.[70] In the films with a pure PCBNB layer (0 wt% BP), a much flatter morphology is observed. It is clear that larger interfacial areas results in more intense CT peaks. AFM on the samples with PCBNB removed shows the same behavior, and also shows that the samples annealed at

150°C have more interfacial area than those annealed at 200°C (Fig. 4.3). The nominal surface areas of the AFM scans correlate with the CT peak intensities, but the resolution attained by AFM is not sufficient to capture true interfacial areas and there a relatively small variation in measured interfacial area, compared to over an order of magnitude in CT peak intensity (Table 4.3).

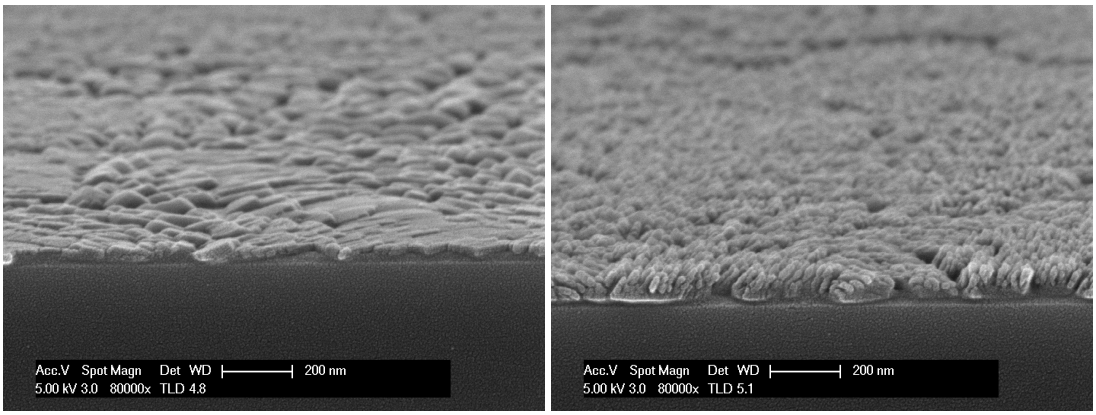

(a) (b)

Figure 4.2: Cross-sectional SEM images of BP/BP:PCBNB samples with PCBNB removed: (a) 0 wt% BP annealed at 200°C, (b) 30 wt% BP annealed at 200°C.

2-D GISAXS on the samples with PCBNB removed show that the 30 wt% BP samples have an in-plane peak somewhere along the Yoneda peak (Fig. 4.4). The peak centers are at a d-spacing of about 20 nm, corresponding to the width of the BP columnar domains. In general, samples which have larger interfacial areas as observed by AFM and SEM also have a higher intensity in-plane peak, which is expected. In some cases it is possible to obtain absolute or relative surface area measurements with small-angle scattering, but

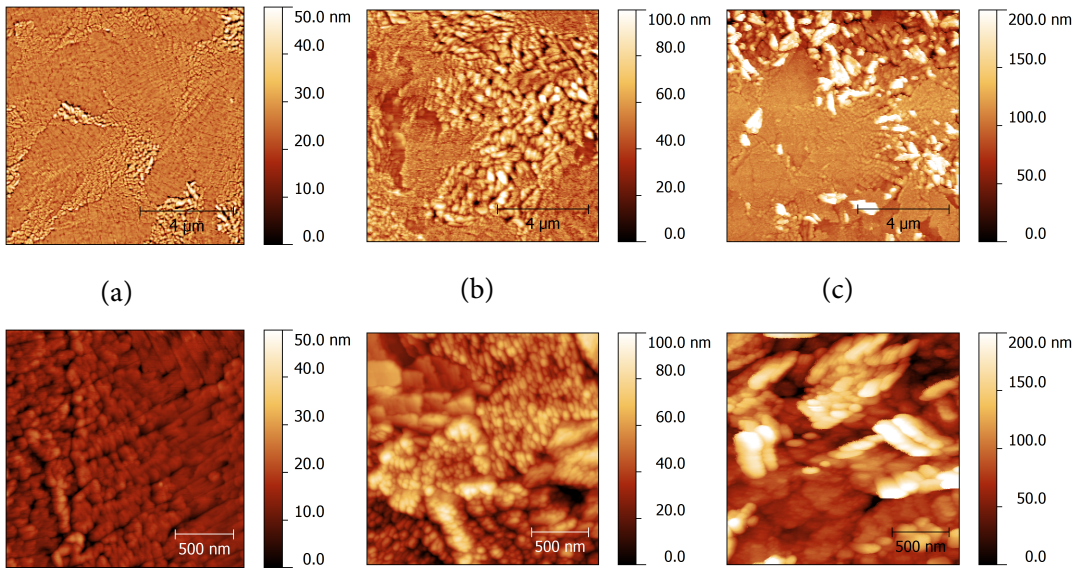

Figure 4.3: 10 µm and 2 µm AFM images of BP/BP:PCBNB samples with PCBNB removed: (a,d) 0 wt% BP annealed at 200°C, (b,e) 30 wt% BP annealed at 200°C, (c,f) 30 wt% BP annealed at 150°C.

this is not the case for our data. For example, the Porod equation cannot be used because the samples are not isotropic; we find that Porod exponent is about 3.3 instead of 4.0 in the case of isotropic samples.

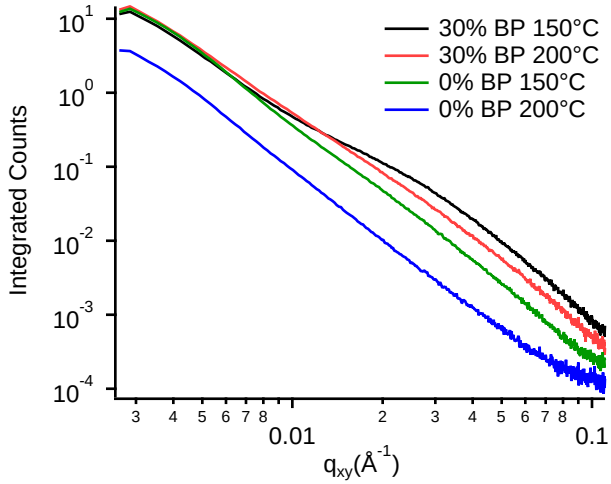

Figure 4.4: Line scan along q_{xy} on the Yoneda peak of BP/BP:PCBNB samples with PCBNB removed (counts produced by integrating 2-D GISAXS at q_z between 0.040 and 0.044 Å^{-1}).

4.3.2 Electrical characterization

Device characterization shows that PCE and J_{sc} increase with the amount of BP in the heterojunction layer, up to 30 wt% BP, and then decrease (Fig. 4.5 and Table 4.1). For the 0 wt% and 10 wt% samples, the PCE and J_{sc} are higher for devices annealed at 200°C, while for the 20 wt%, 30 wt%, and 40 wt% devices, these parameters are higher for devices annealed at 150°C. (Note that slightly higher PCEs were obtained in another batch with only 0 wt% and 30 wt% samples.) These data are for a 14 mg/mL bottom BP layer; no clear trend was found when comparing 7 mg/mL and 14 mg/mL bottom layers. The fill factors

of all the devices were about the same, which is important for analyzing EQE because this means that EQE should not vary with bias too differently for each sample.

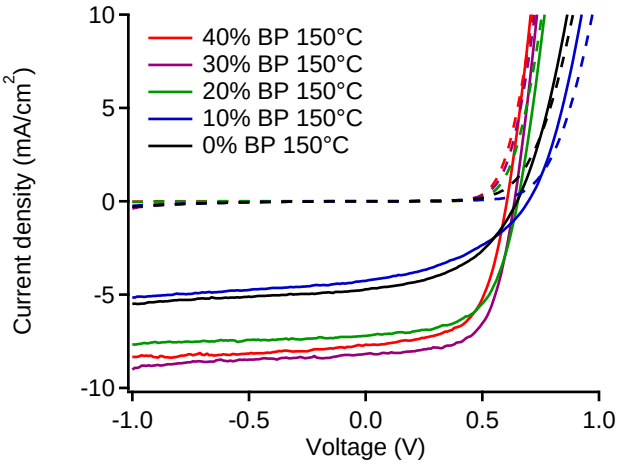

(a)

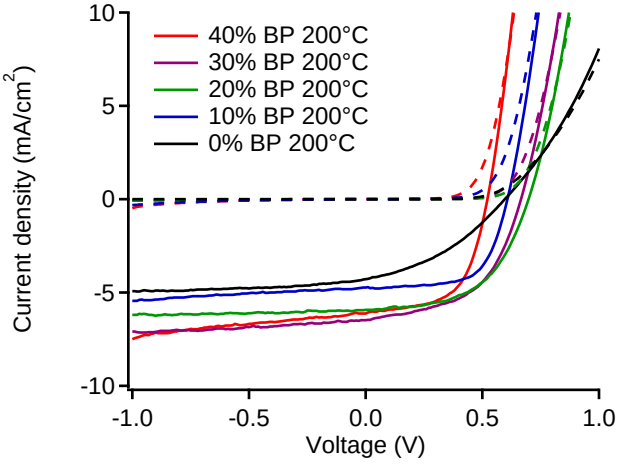

(b)

Figure 4.5: Light (solid lines) and dark (dashed lines) current density-voltage curves of BP/BP:PCBNB solar cells with varied wt% of BP in the BP:PCBNB layer: (a) BP:PCBNB layer annealed at 150°C for 4 hours, (b) BP:PCBNB layer annealed at 200°C for 20 minutes.

Device	V_{oc} [V]	J_{sc} [mA/cm^2]	FF	PCE [%]
0% BP 150°C	0.65	4.72	0.46	1.42
0% BP 200°C	0.60	4.28	0.37	0.95
10% BP 150°C	0.70	4.26	0.41	1.22
10% BP 200°C	0.61	4.73	0.65	1.87
20% BP 150°C	0.65	7.21	0.59	2.77
20% BP 200°C	0.70	5.92	0.54	2.23
30% BP 150°C	0.64	8.18	0.63	3.29
30% BP 200°C	0.67	6.48	0.52	2.26
40% BP 150°C	0.61	7.68	0.60	2.79
40% BP 200°C	0.52	6.12	0.58	1.86

Table 4.1: Device parameters of BP/BP:PCBNB solar cells with varied annealing temperature and wt% of BP in the BP:PCBNB layer.

The dark current of each device was fit with the following diode equation[145] using orthogonal regression, where J_0 is the dark saturation current, q is the elementary charge, n is the ideality factor, k is the Boltzmann constant, T is the absolute temperature, R_{se} is the dark series resistance, and R_{sh} is the dark shunt resistance:

$$J_d(V) = J_0\left[\exp\left(\frac{q(V - J_d(V)R_{se})}{nkT}\right) - 1\right] + \frac{V}{R_{sh}} \tag{4.1}$$

This equation fits all of the dark current curves very well. The fitting coefficients are shown in Table 4.2.

Device	R_{sh} [$\Omega\,cm^2$]	R_{se} [$\Omega\,cm^2$]	J_0 [mA/cm^2]	n	$J_d(V_{oc})$ [mA/cm^2]
0% BP 150°C	4.28×10^4	9.21	1.91×10^{-4}	2.88	1.23
0% BP 200°C	2.21×10^{11}	38.88	2.46×10^{-5}	2.25	0.62
10% BP 150°C	1.45×10^4	10.50	1.41×10^{-5}	2.54	0.70
10% BP 200°C	1.67×10^4	7.59	3.30×10^{-5}	2.05	2.69
20% BP 150°C	8.70×10^5	6.72	6.07×10^{-6}	1.90	3.11
20% BP 200°C	8.26×10^4	8.76	9.16×10^{-6}	2.24	1.68
30% BP 150°C	1.67×10^4	5.65	1.28×10^{-5}	1.95	3.47
30% BP 200°C	6.29×10^4	9.32	7.62×10^{-6}	2.07	1.83
40% BP 150°C	7.59×10^5	6.62	5.97×10^{-6}	1.79	2.60
40% BP 200°C	2.15×10^4	5.67	5.73×10^{-5}	1.89	2.46

Table 4.2: Fitting coefficients of the dark current of the BP/BP:PCBNB solar cells to the diode equation, and experimental J_d at V_{oc}.

Typically an equation for V_{oc} is derived by saying that at V_{oc}, J_d is equal to the photocurrent J_{ph}, which is assumed to be independent of applied voltage and equal to J_{sc}. However, this is not the case, as $J_d(V_{oc}) \neq J_{sc}$ (Table 4.2). Since Eq. (4.1) is a transcendental equation for V, in order to solve for V_{oc} we state this equation at $V = V_{oc}$ in terms of the Lambert W function and use the following approximation: for large real x, $W_0(x) \approx \ln(x) - \ln(\ln(x))$. We also ignore the negligible -1 term and assume $R_{sh} > R_{se}$ and $J_d(V_{oc}) > J_0$, which lets us simplify to obtain:

$$V_{oc} = \frac{nkT}{q} \ln\left(\frac{J_d(V_{oc})}{J_0}\right) \tag{4.2}$$

From this equation, which predicts the actual V_{oc} very accurately, we can see that the differences in V_{oc} between the samples are due to differences in n, J_0, and $J_d(V_{oc})$, and that changes in R_{sh} and R_{se} do not affect V_{oc}.

The above-bandgap EQE plot (Fig. 4.6a) contain three peaks: one at 3.6 eV (340 nm) corresponding to the absorption of the PCBNB, and two at 2.6 eV (480 nm) and 1.8 eV (690 nm) corresponding to the absorption of the BP. The BP peak at 1.8 eV is composed of three humps, also seen in the absorption of pure BP.[143] In the log EQE plot (Fig. 4.6b), the EQE from the absorption of the two components starts to drop off at 1.75-1.80 eV, and a broad CT peak is clearly visible at 1.1 to 1.5 eV. PCBNB absorbs almost identically to PCBM, and in EQE studies involving P3HT and PCBM there is always a bump at 1.75 from the absorption of PCBM.[142] In our case this bump is difficult to see in the EQE

because the bandgap absorption peak of BP and PCBNB are very close in energy. But from UV-vis absorption of BP and PCBNB separately (see SI), we find that the BP peak is at 1.80 eV and the small PCBNB peak is at 1.75 eV.

There is a much greater difference in sub-bandgap EQE (EQE_{CT}) between sample types than there is in above-bandgap EQE (EQE_{bg}), as the CT peak heights vary by over an order of magnitude (Fig. 4.7 and Table 4.3). Both of these EQEs follow the same trend as the PCE and J_{sc}, increasing with the amount of BP in the heterojunction layer. The one difference is that EQE_{CT} continues to increase going from 30 to 40 wt% BP annealed at 150°C, while EQE_{bg} and J_{sc} drop slightly. This may indicate that there is a greater interfacial area at 40 wt% BP, but poorer charge collection.

From UV-vis reflectance spectroscopy, the fraction of incident light absorbed by each solar cell does not vary much with sample type (Fig. 4.8a). The absorption of sub-bandgap light is not shown because the measurement is not sensitive enough. The IQE of the devices (Fig. 4.8b) is calculated from the EQE and from the total absorption, and is relatively flat but the presence of peaks is thought to be due to constructive and destructive interference depending on wavelength and the thickness of each layer of the devices. We also attempted to calculate the IQE' using only the calculated absorption of the active layer (see SI) which was obtained through transfer matrix calculations. The IQE' is not as flat as might be expected, due to the simplifying assumptions in the transfer matrix

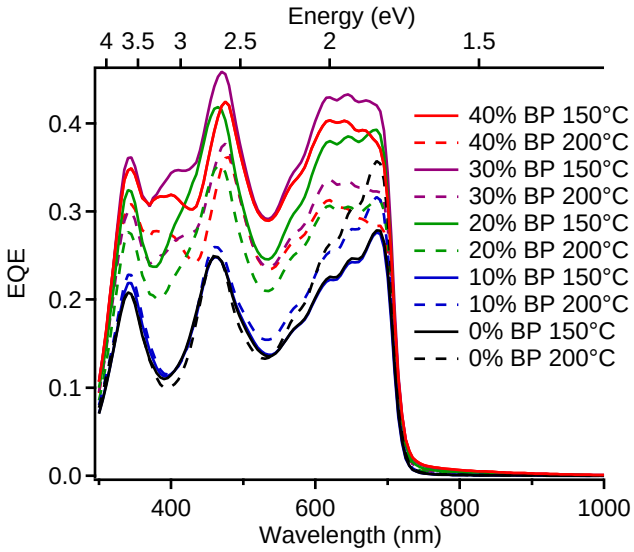

(a)

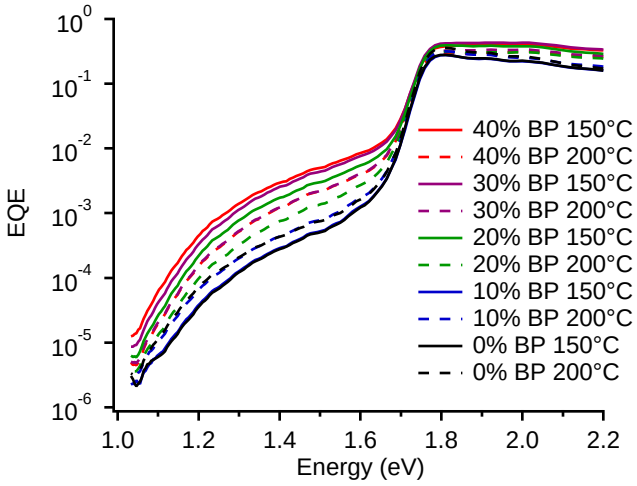

(b)

Figure 4.6: EQE of BP/BP:PCBNB solar cells: (a) versus wavelength, (b) on a log scale versus photon energy.

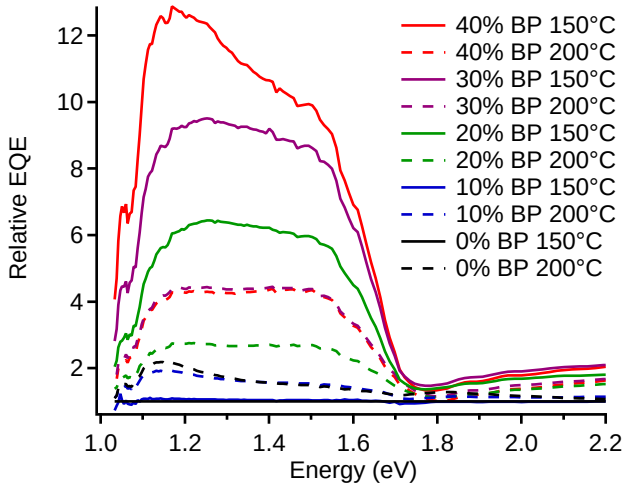

Figure 4.7: EQE of BP/BP:PCBNB solar cells, normalized to the 0% BP 150°C cell.

calculations, namely that BP/BP:PCBNB is treated as one layer and that each layer is homogeneous and perfectly flat.

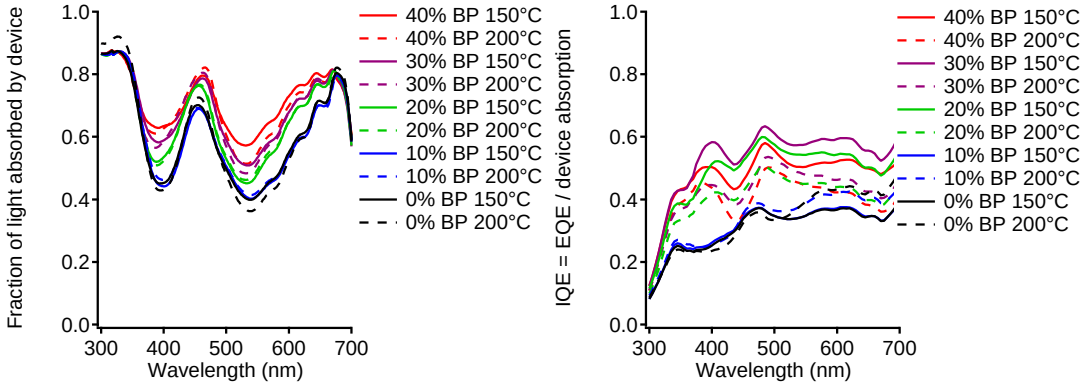

(a) (b)

Figure 4.8: Parameters of BP/BP:PCBNB solar cells: a) total fraction of incident light absorbed by device, b) IQE from total absorption.

Device	EQE_{bg}	EQE_{CT}	AFM area
0% BP 150°C	1.00	1.00	-
0% BP 200°C	1.27	2.03	1.03
10% BP 150°C	0.99	1.07	-
10% BP 200°C	1.13	1.84	-
20% BP 150°C	1.39	6.16	-
20% BP 200°C	1.13	2.74	-
30% BP 150°C	1.49	9.25	1.42
30% BP 200°C	1.16	4.39	1.12
40% BP 150°C	1.33	12.60	-
40% BP 200°C	1.02	4.27	-

Table 4.3: EQE values of BP/BP:PCBNB solar cells at 1.8 eV (EQE_{bg}) and at 1.2 eV (EQE_{CT}), normalized to the 0% BP 150°C cell, and interfacial areas calculated from 2 μm AFM scans of the cells with PCBNB removed, normalized to the area of a flat interface.

4.3.3 Fitting EQE to models

The EQE of a solar cell is a function of incident energy E depends on the IQE and the fraction of incident photons that are absorbed by the device or active layer A. The IQE is the product of the efficiency of exciton migration to a donor-acceptor interface EM, the

charge separation efficiency CS which includes formation of the CT state and dissociation into the charge separated state, and the charge collection efficiency CC. EM is by definition 1 for CT absorption but otherwise does not vary with energy. A recent study has found that the IQE is approximately constant with energy for various material systems including polymer-fullerene, polymer-polymer and all-small-molecule, suggesting that EM is close to 1 at all energies.[146]

$$EQE(E) = A(E)\, IQE(E) \tag{4.3}$$

$$= A(E)\, EM\, CS(E)\, CC \tag{4.4}$$

The probability of absorption A can be calculated using a transfer matrix function of the complex indices of refraction of each layer in the device as a function of energy and the thickness of each layer in the device.[22] In the case of CT absorption which is low and not affected much by the non-active layers, A can be approximated as the product of the density of CT states in the active layer N_{CT}, twice the thickness of the active layer d, and the absorption cross section of a CT state σ_{CT}.

$$EQE_{CT}(E) = [N_{CT} 2d\sigma_{CT}(E)]\, IQE_{CT} \tag{4.5}$$

Several models are used to fit and analyze EQE_{CT}, with some representative fits shown in the SI. The disorder/density of states model developed by Street et al.[141] includes an expo-

nential Urbach tail below the zero-phonon CT state energy E_{CT} and a parabolic*1/energy curve well above this energy, from the assumption of parabolic bands. E_0 is the inverse of the slope of the Urbach tail, C_P is a fitting coefficient combining several terms, and $C_{P\sigma}$ is a coefficient proportional to the absorption cross section. We plot these two components as separate fits. This model fits most of the sub-bandgap energies well, but does not fit the part of the curve near 1.2 eV.

$$EQE_{\text{Urbach}}(E) = \exp\left(\frac{E - E_{CT}}{E_0}\right) EQE_{\text{Urbach}}(E_{CT}) \tag{4.6}$$

$$EQE_{\text{Parabolic}}(E) = \frac{C_P}{E}(E - E_{CT})^2 \tag{4.7}$$

$$C_P = N_{CT} 2d C_{P\sigma} IQE_{CT} \tag{4.8}$$

The Marcus theory model developed by Vandewal et al.[138] is a Gaussian*1/energy curve centered at the zero-phonon CT state energy plus the coupling or reorganizational energy E_λ. C_M is a combined fitting coefficient, and $C_{M\sigma}$ is a coefficient proportional to the absorption cross section. This model fits the sub-bandgap energies well but does not extend to energies as high as the disorder model does.

$$EQE_{\text{Marcus}}(E) = \frac{C_M}{E\sqrt{4\pi k T E_\lambda}} \exp\left(\frac{-(E - E_{CT} - E_\lambda)^2}{4kTE_\lambda}\right) \tag{4.9}$$

$$C_M = N_{CT} 2d C_{M\sigma} IQE_{CT} \tag{4.10}$$

Finally, the empirical model developed by Presselt et al.[142] is the sum of an exponential for disorder and three Gaussians for the absorption of the CT state and for the donor and acceptor. Since the donor and acceptor have very similar band gaps in our case, we use one Gaussian for both. This model fits the entire curve quite well from low energies up to energies above the absorption of the donor and acceptor, but this is expected because there are more terms in the equation.

$$EQE_{\text{Empirical}}(E) = C_{bg}\exp\left(-\frac{(E-E_{bg})^2}{b_{bg}^2}\right) + C_{CT}\exp\left(-\frac{(E-E_{CT})^2}{b_{CT}^2}\right) + \exp\left(\frac{E-E_{\text{disorder}}}{b_{\text{disorder}}}\right) \tag{4.11}$$

The zero-phonon CT state energies E_{CT} resulting from both the disorder and the Marcus fits do not change significantly with sample morphology, ranging from 1.11 to 1.17 eV (Table 4.4). This is surprising because if the molecules at the interface are oriented in the way that GIWAXS indicates, then there should be significant differences in the orientation of donor and acceptor molecules with respect to another with varying interfacial area. Different crystal surfaces would be expected to face each other depending on whether a PCBNB crystallite is adjacent to the top or the side of a BP crystallite. One explanation may be that the molecules at the interface are not part of crystallites but rather are amorphous. As each model can only fit a limited range of energies, the energy range used slightly affects the reported CT state energy. In the disorder model this varies by +/-

0.04 eV and in the Marcus model it varies by +/- 0.02 eV. Both models predict similar CT state energies for each sample. The Marcus model also predicts similar reorganizational energies E_λ for each sample ranging from 0.30 eV to 0.39 eV. In the empirical model, the CT state Gaussian is centered at 1.47 eV, similar to the sum of the zero-phonon CT energy and the reorganizational energy, and the primary absorption Gaussian is centered at 1.78 eV.

Despite the small differences in E_{CT} (0.06 eV spread) in the different samples, the V_{oc} of these samples does differ significantly, with a spread of 0.18 V. There is no trend observed between E_{CT}/q and V_{oc}, in contrast to literature where a linear relationship with a slope of 1 was observed.[147] However, an equation in more recent literature[138] indicates that other parameters also affect V_{oc}, namely temperature, J_{sc}, C_M, E_λ, and the electroluminescence quantum efficiency EQE_{EL}. We derive a similar equation but with the inclusion of the ideality factor by starting with the following equation:

$$J_0 = \frac{2\pi q C_M}{h^3 c^2 EQE_{EL}} (E_{CT} - E_\lambda) \exp\left(\frac{-E_{CT}}{kT}\right) \tag{4.12}$$

and combining with Eq. (4.2) to obtain:

$$V_{oc} = \frac{nE_{CT}}{q} + \frac{nkT}{q} \ln EQE_{EL} + \frac{nkT}{q} \ln\left(\frac{J_d(V_{oc}) h^3 c^2}{2\pi q C_M (E_{CT} - E_\lambda)}\right) \tag{4.13}$$

Although we did not see a trend between E_{CT}/q and V_{oc}, we do observe a strong trend between V_{oc} and nE_{CT}/q with a slope of 3.9 (a large change in nE_{CT}/q causes a

	Marcus			Urbach		Parabolic	
Device	E_{CT} [eV]	E_λ [eV]	C_M [eV^2]	E_{CT} [eV]	E_0 [eV]	E_{CT} [eV]	C_P [eV^{-1}]
0% BP 150°C	1.13	0.39	0.2×10^{-3}	1.17	6.7×10^{-2}	1.16	0.7×10^{-2}
0% BP 200°C	1.11	0.38	0.3×10^{-3}	1.13	4.9×10^{-2}	1.13	0.9×10^{-2}
10% BP 150°C	1.13	0.39	0.2×10^{-3}	1.16	5.9×10^{-2}	1.16	0.7×10^{-2}
10% BP 200°C	1.12	0.38	0.3×10^{-3}	1.14	5.2×10^{-2}	1.15	1.0×10^{-2}
20% BP 150°C	1.17	0.30	0.9×10^{-3}	1.13	4.3×10^{-2}	1.14	3.5×10^{-2}
20% BP 200°C	1.15	0.35	0.4×10^{-3}	1.15	4.9×10^{-2}	1.15	1.7×10^{-2}
30% BP 150°C	1.16	0.32	1.4×10^{-3}	1.13	4.3×10^{-2}	1.13	4.9×10^{-2}
30% BP 200°C	1.16	0.34	0.7×10^{-3}	1.15	4.5×10^{-2}	1.14	2.7×10^{-2}
40% BP 150°C	1.14	0.33	1.6×10^{-3}	1.12	4.3×10^{-2}	1.12	5.2×10^{-2}
40% BP 200°C	1.16	0.34	0.7×10^{-3}	1.15	4.4×10^{-2}	1.15	2.7×10^{-2}

Table 4.4: EQE fit parameters of BP/BP:PCBNB solar cells using several different models.

small change in V_{oc}). In our samples temperature is constant and the only piece of data we are missing is EQE_{EL}. This lets us obtain a calculated EQE_{EL} for each sample from Eq. (4.13), which range from 5×10^{-13} to 1×10^{-10} but do not follow any particular trend with V_{oc}. These numbers are several orders of magnitude smaller than measured EQE_{EL} in the literature.[138] When this same analysis was done neglecting the ideality factor, we

obtained EQE_{EL} ranging from 3×10^{-8} to 3×10^{-5}, which is on the same order as the literature.

In the disorder model, the slope $1/E_0$ of the Urbach edge is associated with the slope of the exponential density of states in the band gap of the donor and acceptor. This slope does vary with sample morphology, and appears to be slightly steeper in samples with greater interfacial areas. This suggests that in these samples there is less disorder and fewer deep trap states. E_0 is similar to other OPV systems and ranges from 43-67 meV, compared to about 38 meV for P3HT:PCBM at room temperature[141] and 35-69 meV in a study of small molecule solar cells.[148]

The parameter that changes the most with sample processing is the height of the sub-bandgap EQE, which is associated with the term C_M in the Marcus theory model and the term C_P in the parabolic portion of the disorder model. As discussed previously, the height closely tracks the approximate interfacial area from AFM. The numbers for C_M we obtain here are similar to those of a few polymers in the literature at room temperature, but about an order of magnitude higher than that of P3HT:PCBM.[138]

We can now form a more complete picture of the energy transitions that occur in BP:PCBNB solar cells (from the point of view of the Marcus model) (Fig. 4.9). The optical band gap of BP and PCBNB are 1.74 eV and 1.67 eV respectively, from fitting the absorption spectra onsets. These band gaps determine the initial energies of the excitons. During charge transfer at a donor-acceptor interface, if the charge transfer excitons relax

to the lowest CT state instead of undergoing "hot" exciton dissocation, they decrease in energy to E_{CT}, about 1.15 eV. Charge transfer excitons can also be formed by direct excitation at energies centered at $E_{CT} + E_{\lambda}$, about 1.5 eV. After charge separation, the energy of the separated charges depends on the difference between the HOMO of BP (4.9 eV) and the LUMO of PCBNB (4.0 eV)[75] which is the same as that of PCBM. This difference is about 0.9 eV. Finally the charges are collected at the electrodes with a small energy loss to obtain V_{oc}, which is 0.64 eV in the highest efficiency sample.

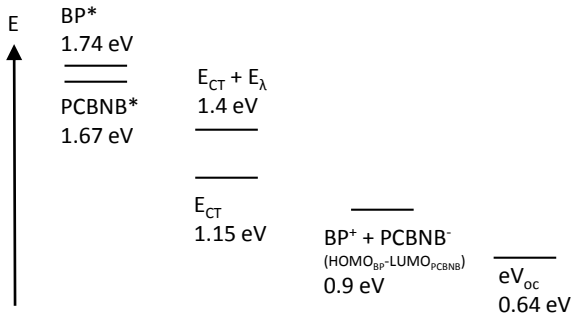

Figure 4.9: Energy levels of the BP:PCBNB solar cell.

4.3.4 Density and oscillator strength of CT states

From the heights of the CT peaks in the EQE and Eq. (4.10), we calculate the density of CT states and an average oscillator strength of the CT state in the BP:PCBNB system. Several assumptions are required: first we assume that the IQE_{CT} of each sample is equal to its above-bandgap IQE. This was recently found to be approximately the case for

two polymer-fullerene BHJ systems.[146] For IQE_{CT} we take the average of IQE from 320 to 675 nm. EM and the CT state formation efficiency component of CS are assumed to be 1 at energies both above and below the band gap, and $C_{M\sigma}$ is assumed to be a constant in this system. Finally, one additional piece of data is needed. We assume that the interfacial area from AFM of the 0% BP 200C sample (which is smoothest and therefore the determination of surface area by AFM is likely the most accurate on this sample) is the actual interfacial area of that sample.

Using the definition of C_M in the Marcus model in Eq. (4.10) and the number of CT states per unit interfacial area (calculated from the known crystal structures of BP[49] and PCBNB,[149] we use the number of BP molecules per unit interfacial area, as BP has the lower areal molecular density) we find that $C_{M\sigma} = 3.85 \times 10^{-18}$ eV^2 cm^2. This lets us calculate N_{CT} for each sample (Table 4.5). Note that the number of CT states per unit interfacial area varies depending on the face of the BP unit cell that is closest to the PCBNB unit cell, so the average is taken. More informative than the CT state volume density N_{CT} is the CT state area density $N_{CT}d$, which correlates with the EQE peak height and varies over half an order of magnitude with sample processing. This confirms that simple sub-bandgap EQE measurements are a good non-destructive measure of the CT state density.

We then use $C_{M\sigma}$ to calculate the absorption cross section of a CT state from the Marcus model $\sigma_{CT_{\text{Marcus}}}$. The oscillator strength of a CT state f is then calculated by integrating

Device	IQE_{CT}	d [nm]	N_{CT} [cm^{-3}]	$N_{CT}d$ [cm^{-2}]
0% BP 150°C	0.44	85	0.7×10^{19}	0.6×10^{14}
0% BP 200°C	0.47	83	0.9×10^{19}	0.7×10^{14}
10% BP 150°C	0.46	72	0.8×10^{19}	0.6×10^{14}
10% BP 200°C	0.46	98	0.8×10^{19}	0.8×10^{14}
20% BP 150°C	0.65	122	1.5×10^{19}	1.8×10^{14}
20% BP 200°C	0.54	98	1.1×10^{19}	1.1×10^{14}
30% BP 150°C	0.68	131	2.0×10^{19}	2.6×10^{14}
30% BP 200°C	0.55	115	1.5×10^{19}	1.7×10^{14}
40% BP 150°C	0.59	125	2.7×10^{19}	3.4×10^{14}
40% BP 200°C	0.52	112	1.6×10^{19}	1.8×10^{14}

Table 4.5: IQE_{CT}, total active layer thickness (pure BP layer plus mixed layer), CT state density, and CT state areal density of BP:PCBNB solar cells. The pure BP layer thickness by itself is approximately 42.8 nm.

the absorption cross section over its energy band.[150,151] Here h is the Planck constant, m_e is the mass of the electron, ε_0 is the vacuum permittivity, and c is the speed of light. We obtain $f_{CT} = 0.024$.

$$\sigma_{CT_{\text{Parabolic}}}(E) = \frac{C_{P\sigma}}{E}(E - E_{CT})^2 \tag{4.14}$$

$$\sigma_{CT_{\text{Marcus}}}(E) = \frac{C_{M\sigma}}{E\sqrt{4\pi kTE_\lambda}} \exp\left(\frac{-(E - E_{CT} - E_\lambda)^2}{4kTE_\lambda}\right) \tag{4.15}$$

$$f = \frac{4m_e\varepsilon_0 c}{hq^2} \int_E \sigma(E)dE \tag{4.16}$$

The oscillator strength of the CT state is about an order of magnitude smaller than that of BP, which is $f_D = 0.32$. The latter was obtained by integrating the absorption cross section of a pure BP layer σ_D in the lowest energy absorption band, 1.6 eV to 2.3 eV in Eq. (4.16). σ_D was obtained from the decadic absorbance a_D, thickness d, and density of BP chromophores N_D:

$$\sigma_D(E) = \frac{2.303a_D(E)}{N_D d} \tag{4.17}$$

4.3.5 Simulation of exciton diffusion

Instead of assuming that the IQE_{CT} of each sample is equal to its above-bandgap IQE, we now calculate upper and lower bounds for the exciton migration efficiency EM and charge collection efficiency CC. Based on these bounds and results from a kinetic Monte-Carlo simulation of exciton diffusion in a bilayer, we estimate an exciton diffusion length for both the BP and PCBNB. Unlike the previous section, we do not use the AFM interfacial area. However we do need to assume that the charge separation efficiency CS = 1.

The efficiency of a solar cell is determined by the efficiencies of exciton collection, charge separation, and charge collection. We begin by assuming assuming EQE is given by Eq. (4.4) so $IQE(E) = EMCS(E)CC$. Using the measured EQE and IQE, we can estimate the values of EM and CC for the donor and acceptor phases as well as approximate the exciton diffusion lengths of the materials and the number of charge transfer states at the interfaces.

We can use the donor and acceptor regions in the IQE to define upper and lower bounds on the values of EM and CC (donor and acceptor are designated by subscripts D and A). The probability of charge separation, CS, is assumed to be 1, and so IQE is independent of photon energy. The upper bound of the exciton collection efficiency is $EM \leq 1$, so the lower bound on CC is given by $CC_D \geq IQE_D$ and $CC_A \geq IQE_A$. If we assume that CC is the same for charges generated from excitations on the donor and on the acceptor, then $CC \geq \max(IQE_D, IQE_A)$. Now we define l to match the subscript of the larger value of IQE and s to match the subscript of the smaller value of IQE. Then the upper bound on EM_l is still 1, but the upper bound on EM_s is now $IQE_s/\min(CC)$ and $\min(CC)$ will be IQE_l.

The other bounds can be determined similarly, assuming that $CC \leq 1$. Then $EM_D \geq IQE_D$ and $EM_A \geq IQE_A$.

To summarize:

$$IQE_l \leq CC \leq 1 \tag{4.18}$$

$$IQE_l \leq EM_l \leq 1 \tag{4.19}$$

$$IQE_s \leq EM_s \leq \frac{IQE_s}{IQE_l} \tag{4.20}$$

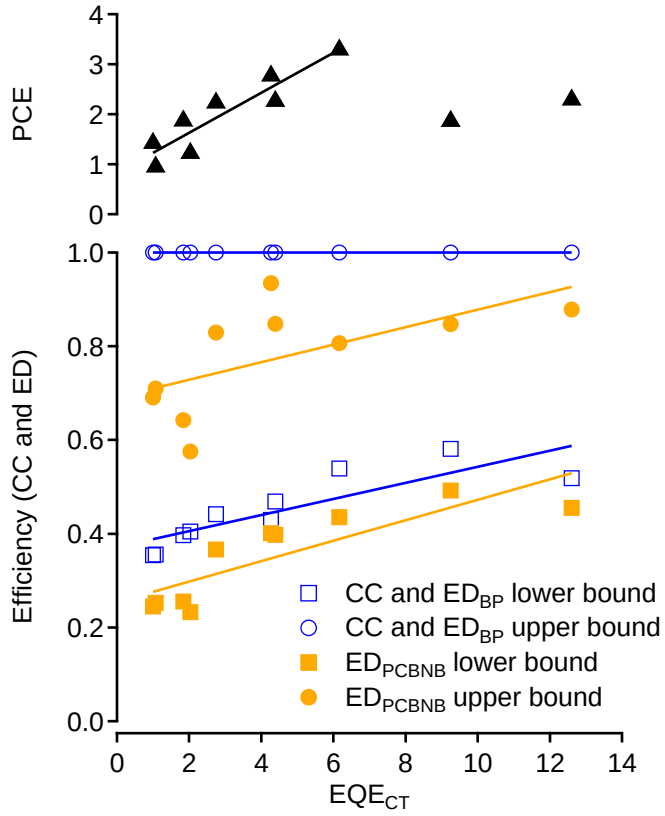

Figure 4.10: PCE versus normalized CT peak height and upper and lower bounds on CC, EM_{BP} and EM_{PCBNB} versus normalized CT. The markers show data for each sample and the solid lines show a best fit curve to guide the eye.

From these equations, we can estimate values for upper and lower bounds on CC, EM_D, and EM_A in our samples by taking the average value of IQE for the regions of donor and acceptor absorbance (from 475 to 700nm for BP and from 325 to 425 nm for PCBNB).

In all samples, $IQE_l = IQE_D$ and $IQE_s = IQE_A$. A plot of these efficiencies derived from IQE versus the normalized height of the CT peak (Fig. 4.10) shows increasing lower bounds on efficiencies with increasing CT peak height. This trend roughly tracks the increases in PCE for the samples up until the two samples with the highest CT peaks.

Using this information we can also put upper and lower bounds on A_{CT} from Eq. (4.4) which we could not determine exactly from experiment.

$$EQE_{CT}(s_1) = A_{CT}(s_1) IQE_{CT}(s_1) \tag{4.21}$$

$$= A_{CT}(s_1) EM(s_1) CC(s_1). \tag{4.22}$$

We know that $EM(s_1)$ should be 1 for CT states so the equation becomes

$$EQE_{CT}(s_1) = A_{CT}(s_1) CC(s_1). \tag{4.23}$$

And we can use the upper and lower bounds of CC to set the bounds on A_{CT}

$$EQE_{CT}(s_1) \leq A_{CT}(s_1) \leq \frac{EQE_{CT}(s_1)}{IQE_l(s_1)}. \tag{4.24}$$

So for s_1 = 0% BP 200°C, $A_{CT}(s_1)$ is between 1×10^{-4} and 2×10^{-4} and for s_2 = 30% BP 200°C, $A_{CT}(s_2)$ is between 4×10^{-4} and 6×10^{-4}. Which means the upper and lower bounds on the ratio of A_{CT} is given by

$$IQE_l(s_2) \frac{EQE_{CT}(s_1)}{EQE_{CT}(s_2)} \leq \frac{A_{CT}(s_1)}{A_{CT}(s_2)} \leq \frac{1}{IQE_l(s_1)} \frac{EQE_{CT}(s_1)}{EQE_{CT}(s_2)} \tag{4.25}$$

Then for s_2 and s_1, $2 \leq \frac{A_{CT}(s_1)}{A_{CT}(s_2)} \leq 8$ (EQE ratio at E_{CT} alone gives 4.6).

Additional measurements could allow for a more accurate determination of A_{CT} (PDS, surface area[1]) or EM (fluorescence quenching). Based on our measurements of SA by AFM, N_{CT} changes by ~ 40% while the ratio of EQEs at the CT energy change by nearly an order of magnitude (Table 4.3). The maximum possible increase in CC (which is bounded by 100% efficiency) is not large enough to account for the increase in EQE, which suggests that our measurement of surface area by AFM does not give an accurate estimate in the actual molecular interfacial area where CT states form, especially for samples with rougher interfaces.

We also estimate the exciton diffusion length of both materials using a kinetic Monte-Carlo simulation of exciton diffusion. Exciton diffusion is treated as Förster resonance energy transfer between chromophores within our active layer films and we are able to simulate the exciton diffusion length and the efficiency of exciton migration to the interface. We compare simulated results for a bilayer to the device data from the 0% BP 200°C because it is the closest to a true bilayer (RMS roughness by AFM is 3.5 nm). The films are treated as square lattices of BP or PCBNB with the appropriate chromophore densities (giving square lattice unit cell parameters of a = 0.84 nm and 1.04 nm, respectively). We assume a square lattice will give no more than a 20% error in L_D because it is known

[1] Attempts at photothermal deflection spectroscopy failed because the technique is not sensitive enough to measure the absorption of the CT state of our samples and determinations of surface area by atomic force microscopy and small angle X-ray scattering did not provide accurate estimates of the intermolecular interfaces.

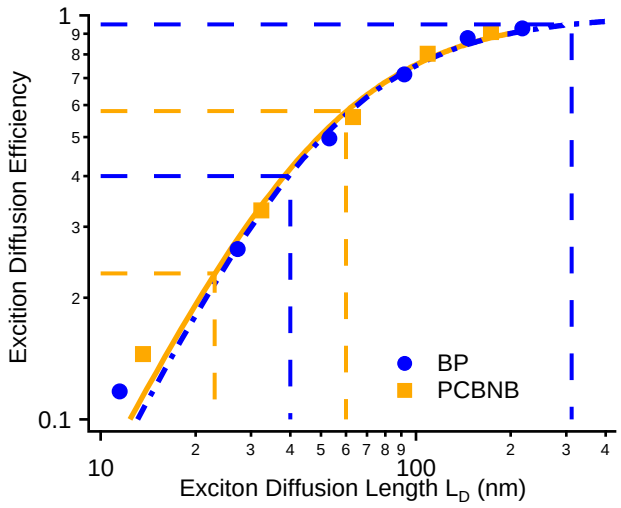

Figure 4.11: Exciton migration efficiency as a function of exciton diffusion length L_D. The markers show the simulated efficiency of migration of excitons to the bilayer interface for the BP and PCBNB layers in the bilayer device. The solid lines are best fit lines to the simulated data. The dashed lines show the upper and lower bounds of EM and L_D for BP and PCBNB.

analytically that the difference in L_D between a square lattice and randomly distributed chromophores of the same number density is only 20%.[152]

Based on the upper and lower bounds of EM for the flattest sample (0% BP 200°C) and the simulated EM (Fig. 4.11), the exciton diffusion length of BP in our polycrystalline samples is between 40 and 380 nm (EM between 0.40 and 0.95) and the exciton diffusion length of amorphous PCBNB is between 23 and 60 nm (EM between 0.23 and 0.58). The range we determined for L_D of BP compares favorably with the published literature value

of 100 to 400 nm (for different directions in the lattice plane of single crystals of BP) calculated by DFT.[153]

4.4 Conclusion

In this work, we have examined CT states at interfaces between the small molecule donor BP and acceptor PCBNB. By varying annealing temperature and the donor-acceptor ratio in the mixed layer, we have been able to control the columnar morphology and interfacial area between the donor and acceptor. We demonstrate that the height of the CT peak in EQE spectra can be used as a non-destructive method for approximating interfacial area. We have observed that the height of this peak varies over an order of magnitude with processing, while the energy of the CT peak remains relatively constant despite differences in the interface at the molecular level. The Urbach energy of the CT peak is slightly lower for samples with more interfacial area suggesting that in these samples there is less disorder. With the assumption that the sub-bandgap IQE is similar to the above-bandgap IQE we calculated the oscillator strength of a CT state. Finally, using a simulation of Förster resonance energy transfer between chromophores within our active layer films, we have calculated bounds for the components of EQE and for the exciton binding energy.

4.5 Supporting Information

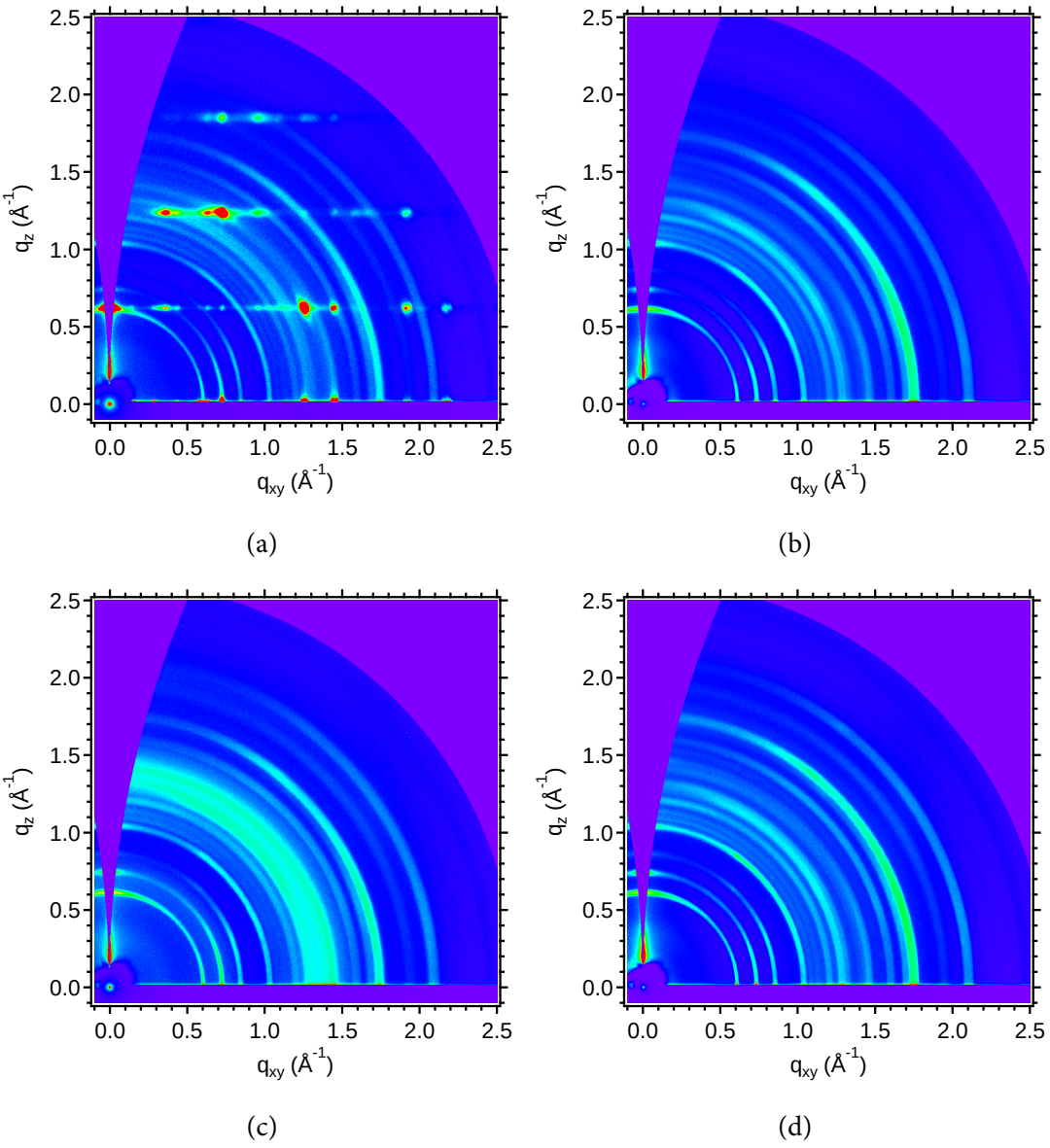

Figure 4.12: 2-D GIWAXS of BP/BP:PCBNB films a) annealed at 150°C before rinsing, b) after rinsing with toluene; c) annealed at 200°C before rinsing, d) after rinsing with toluene.

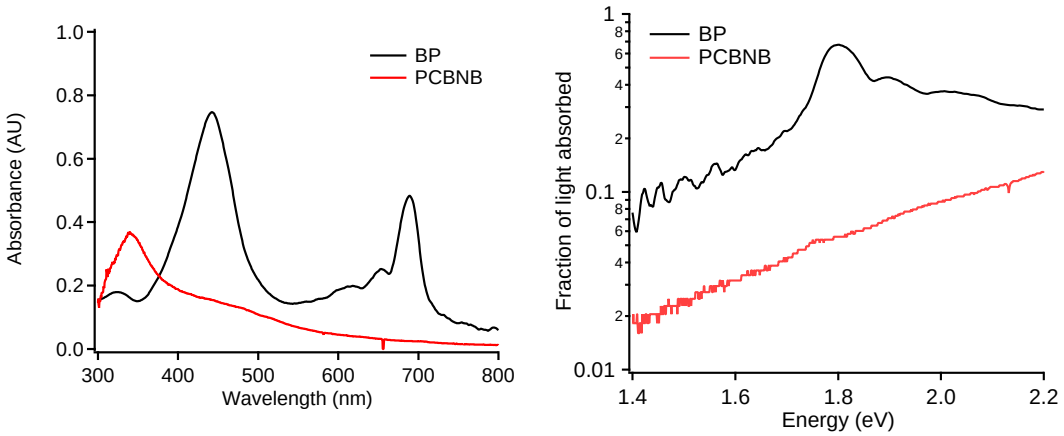

Figure 4.13: a) Decadic absorbance of spin-coated BP and PCBNB films annealed at 150°C, b) fraction absorbed on a log scale.

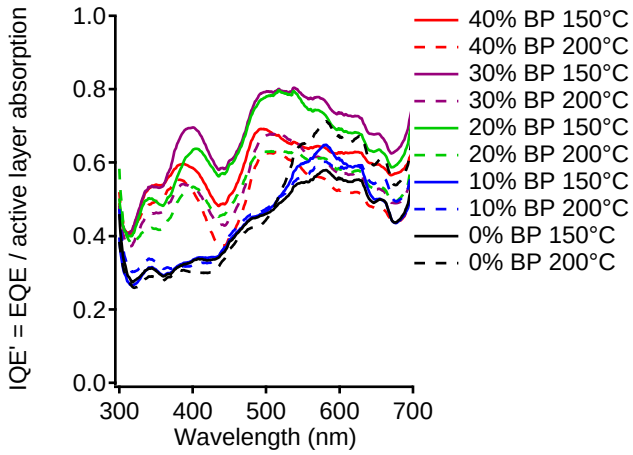

Figure 4.14: IQE' (IQE calculated from active layer absorption) of BP/BP:PCBNB solar cells.

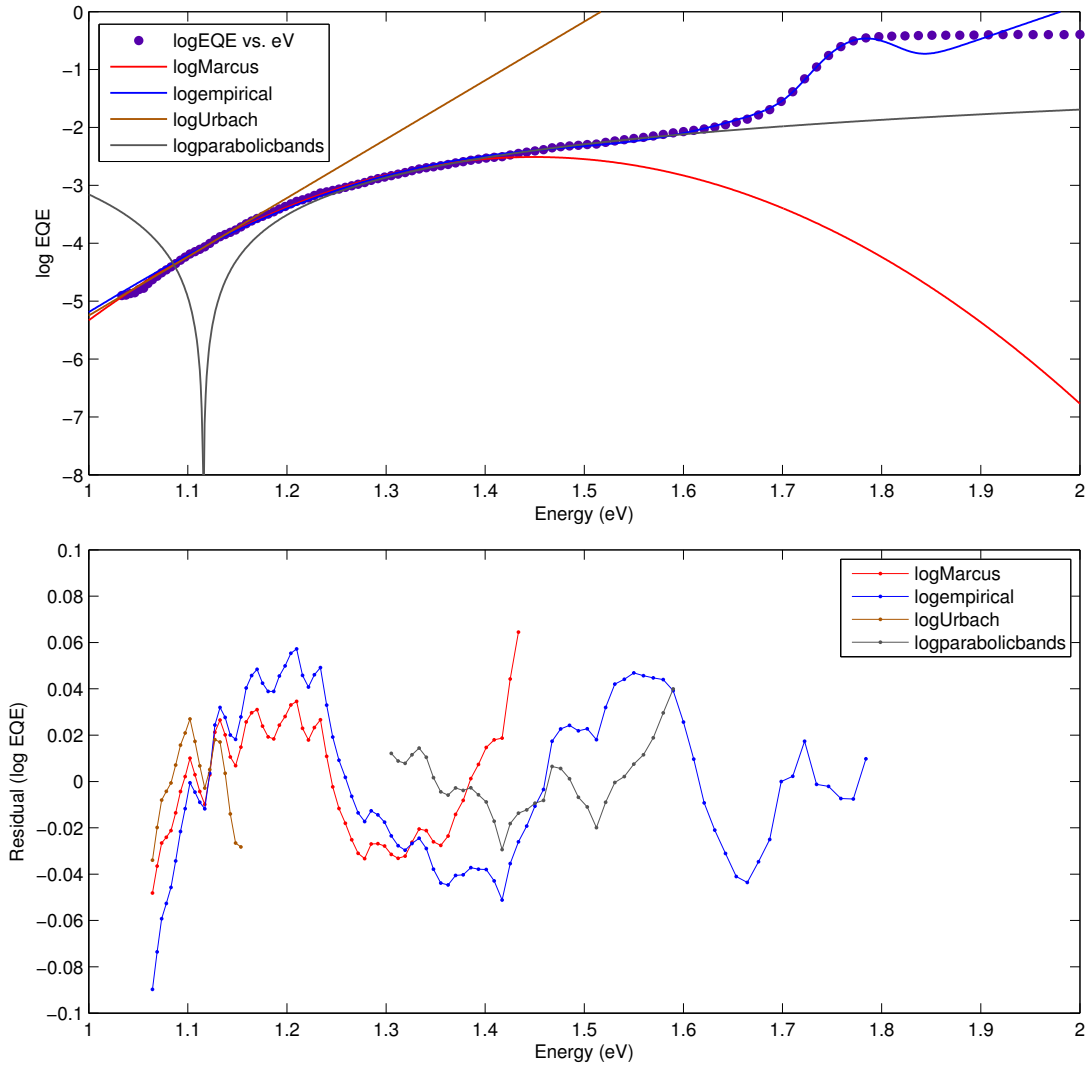

Figure 4.15: Log EQE of the sample with the highest CT peak (40 wt% BP, 150°C), fits of the data using various models, and residuals of the fits.

Chapter 5

Characterization of Solution-Processed Electronic Devices

Many of the relationships between structure, properties, and performance found in organic photovoltaics are also useful in studying organic semiconductors for other applications, as well as solution-processed photovoltaics and other electronic devices in general. Additionally, many of the thin film fabrication and characterization techniques also apply to these other applications. In this section we discuss several projects in which solution-processed electronic devices are characterized. First, the phenomenon of ionic photoconductivity in amorphous ZnO (a-ZnO) thin films is studied by impedance measurements and by studying the behavior of photodetectors and TFTs. Then, the fabrication and characterization of organic solar cells using novel π-A-π donor polymers is discussed. Finally, the use of fullerene derivatives for thermoelectric applications is briefly discussed.

5.1 UV-induced ionic photoconductivity in *a*-ZnO photodetectors and transistors

We investigate the mechanism for persistent photoconductivity after UV exposure in solution processed *a*-ZnO thin films by measuring the impedance of MIS capacitors. We find that the impedance behavior cannot be explained only by an increase in free electrons after UV exposure, but is a result of mobile positive ions generated by UV exposure. We then explore how persistent photoconductivity and ionic conductivity affect the behavior of *a*-ZnO TFTs and hybrid *a*-ZnO/P3HT:PCBM photodetectors. These effects may be utilized to create UV photodetectors that do not require constant polling, reducing power consumption.

5.1.1 Introduction

ZnO is a wide bandgap semiconductor that has attracted attention for potential applications in thin film devices such as UV photodetectors,[154–156] solar cells,[157] thin film transistors (TFTs),[158–165] and sensors.[166,167] ZnO has been used as an oxygen[166] and hydrogen sensor,[167] as the presence of these gases greatly affects photoconductivity under UV illumination. ZnO spun from a precursor solution,[158–161] ZnO nanoparticles[162–164] and ZnO nanowires[165] have been used as the semiconductor in n-type TFTs. In some of these

devices,[161,164] UV exposure has been used to convert precursors to ZnO in order to yield higher mobility at lower temperatures.

It is well known that UV exposure causes persistent conductivity (PPC) in crystalline ZnO. This fact is commonly used to improve device performance. For example, ZnO has been used as an hole blocking layer in solar cells, and often requires some amount of light soaking to turn on the PPC before reaching maximum efficiency.[168–172] It is important to better understand the stability of ZnO with light exposure in these devices.

PPC in crystalline[154,167,170,173] ZnO is typically explained by the following processes: i) Atmospheric oxygen adsorbs onto the ZnO surface, trapping electrons and creating a non-conducting depletion layer. UV exposure above the ZnO band gap generates holes and electrons, and the holes react with the adsorbed oxygen, desorbing it from the surface and increasing conductivity. ii) Additionally, UV exposure may also cause photolysis of ZnO[173,174] and the desorption of lattice oxygen, which is possibly catalyzed by surface hydrocarbons. This generates oxygen vacancies, which may become positively charged.[154,175] When the ZnO is exposed to ambient conditions, oxygen again adsorbs to the surface and fills the oxygen vacancies in the lattice, decreasing conductivity. iii) Finally, hydrogen ions and molecules in interstitial sites and in oxygen vacancies may dope the ZnO and contribute to PPC.[176,177] In contrast to its crystalline phase, there is no literature focused on studying PPC in *a*-ZnO but we start with the assumption that these processes occur to a certain extent in this material. In one study dealing with *a*-ZnO,[159] it was found

that TFTs exposed to oxygen when the ZnO was previously annealed in hydrogen have decreased current due to the formation of OH groups that act as electron acceptors.

While most studies that investigate PPC focus on crystalline ZnO films and nanowires, we investigate this effect in *a*-ZnO by analyzing the impact of UV radiation on the impedance of metal-insulator-semiconductor (MIS) capacitors and the dark current of organic solar cells with a transparent hole blocking ZnO layer. From our analysis, we find a third aspect of the PPC behavior in *a*-ZnO, in that UV exposure creates mobile ions that not only contribute to conductivity, but also significantly alter device characteristics in a way that cannot be explained by the previous two mechanisms alone. PPC has been observed to be much stronger in solution processed *a*-ZnO[158] than in crystalline ZnO, and stronger in devices with a surface-to-volume ratio such as nanorods[178] or very thin films.

Solution processed ZnO is of particular interest for lower cost and large area processing. There are several approaches to fabricating solution processed ZnO. Here we use an ammonium hydroxide precursor[179] which has the advantage of a single synthesis step and lets one use annealing temperatures between 120°C and 135°C. At these low temperatures the resulting film is amorphous.[180]

Most solution based ZnO precursor processes, including the one we use, yield thin films on the order of a few tens of nm at most.[159–161] This is not thick enough to act as an effective UV photodetector by charge generation from absorbed photons; about 200

nm of ZnO are needed to absorb about 80% of 350 nm light. Nevertheless, we utilize the PPC/ionic conductivity property of ZnO to enable low-power UV detection in devices with photodetector and TFT structures.

5.1.2 Experimental section

Solutions

Poly(3-hexylthiophene) (P3HT), brand name Sepiolid P200, was obtained from Rieke Metals. [6,6]-phenyl-C61-butyric acid methyl ester (PCBM) was obtained from NanoC. A blend solution with 20 mg/mL of P3HT and 16 mg/mL of PCBM in o-dichlorobenzene (ODCB) was prepared for photodetectors. A solution of 10 mg/mL of P3HT in ODCB was created for TFTs. ZnO thin films were made from an ammonia based precursor solution of 0.1M $ZnO \cdot nH_2O$ in 19% NH_3(aq). Additional information can be found in previous publications.[160,181]

Photodetectors

Indium tin oxide (ITO) substrates were sonicated in acetone, deionized water and Alconox detergent, deionized water, and isopropanol, then cleaned with air plasma. 50 nm of Al was deposited with a thermal evaporator through a mask with several pixels to form the cathode. On some samples, a 5 nm layer of ZnO was spin coated and annealed at 130°C for 30 minutes. About 220 nm of P3HT:PCBM was spin coated in a nitrogen

glovebox, dried under a petri dish, and annealed at 150°C for 5 minutes. A 10 nm MoO_3 electron blocking layer followed by a 10 nm semitransparent Ag anode was thermally deposited (Fig. 5.1a). Current density vs. voltage curves of the photodetectors were measured in a nitrogen glovebox using a 300 W xenon arc lamp to closely match the AM 1.5 solar spectrum. External quantum efficiency was measured using the same lamp, a monochromator, and a lock-in technique in which the incident light and device current were chopped. For higher precision testing of UV exposure, a UV LED was pulsed at 2 Hz for several hours while the device current at -0.5 V on the Ag electrode was continuously measured. The current was then measured during recovery in the dark for several days. The LED had emission centered at 365 nm and a FWHM of 10 nm. Transfer matrix model software[23] was used to calculate the approximate fraction of photons incident on the photodetector active area that are absorbed by the ZnO layer.

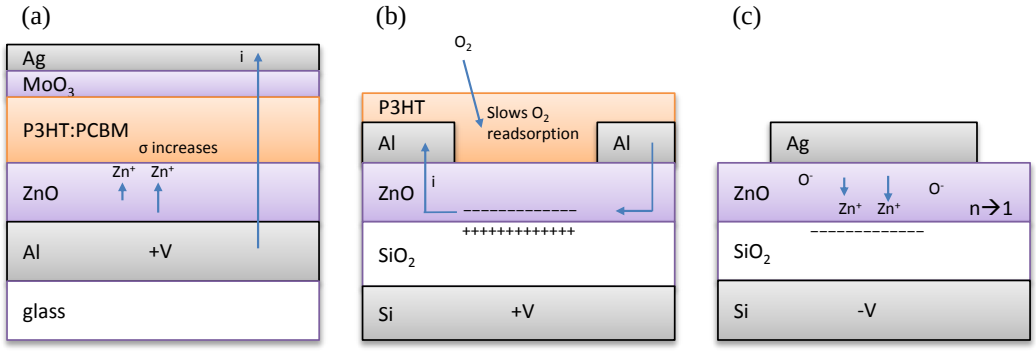

Figure 5.1: Device structures of (a) organic photodetectors with ZnO blocking layer, (b) ZnO TFTs, and (c) ZnO MIS capacitors.

TFTs and MIS capacitors

Bottom-gate top-contact thin film transistors were fabricated as follows: antimony-doped n-type Si with a 200 nm thermal oxide was sonicated in acetone, isopropanol, and deionized water, then cleaned with oxygen plasma. A ~ 5 nm layer of ZnO was spin coated and annealed at 150°C for 30 minutes. 140 nm of Al was thermally deposited for the source and drain electrodes. On some samples, approximately 50 nm of P3HT was spin coated on top of the electrodes, and on others only the solvent, ODCB, was spin coated on top (Fig. 5.1b).

MIS capacitors were fabricated as follows: boron-doped p-type Si with a 100 nm thermal oxide and a conductivity of 0.001–0.005 Ω−cm (translates to a dopant concentration of 1.5×10^{19}–1.5×10^{20} cm^{-3})[182] was sonicated in acetone, isopropanol, and deionized water, then cleaned with oxygen plasma. A ~ 5 nm layer of ZnO was spin coated and annealed at 130°C for 30 minutes. This step was repeated 3-4 times to form about 15 or 20 nm thick films. Control samples with no ZnO were also fabricated. 120 nm of Ag was thermally deposited with a circular mask (Fig. 5.1c).

The TFTs and MIS capacitors were measured in a probe station, both in the dark and after exposure to a low-pressure mercury-vapor lamp at 254 nm through the quartz window of the probe station. A diamond scribe was used to scratch through the back oxide layer, and silver paste was used to connect the Si to the bias-controlled probe station chuck. TFTs were tested under vacuum, and MIS capacitors were tested under nitrogen.

Impedance magnitude and phase of the MIS capacitors were measured with a Solartron 1260 Impedance/Gain-Phase Analyzer with alternating voltage at frequencies of 5 Hz to 1 MHz and an amplitude of 0.1 V on top of a direct voltage from -40 to 40 V. In the MIS capacitors, although light is blocked from directly reaching the ZnO layer under the Ag (the active area), the SiO_2 not covered by Ag acts as a waveguide and allows light to reach the ZnO active area. UV light at angles greater than 3.14° will be totally reflected and coupled to the ZnO which has a higher refractive index than SiO_2.

5.1.3 Results and discussion

Impedance spectroscopy reveals ion migration

To investigate the mechanisms behind PPC in *a*-ZnO, we conduct impedance measurements of a MIS capacitors (Fig. 5.1c) with *a*-ZnO as the semiconductor layer before and after UV exposure. Before UV exposure, the Nyquist plot shows nearly ideal capacitive behavior with Z" > Z' (Fig. 5.2a). We fit the pre-UV impedance behavior with an equivalent circuit composed of a series resistor and capacitor for the ZnO, R_{ZnO} and C_{ZnO} (Fig. 5.2b). These are in series with the resistor and capacitor for the contacts and the SiO_2 dielectric, whose values were obtained by measuring the control sample. The calculated capacitance of the ZnO layer C_{ZnO} varies with applied DC bias. When the device is in the depletion regime (negative bias on Si), electrons in the ZnO are pushed away from the

SiO_2/ZnO interface, decreasing C_{ZnO}. When the device is in the accumulation regime (positive bias on Si), electrons are attracted to the interface, increasing C_{ZnO} (Fig. 5.2c).

Using the second harmonic of the C-V measurement in Fig. 5.2c with Eq. (5.1)[183] yields the density of trap states in the active layer N dependent on the distance W from the interface. From this we find that the trap states in the ZnO before UV exposure are evenly distributed as a function of depth (Fig. 5.2d).

$$N(W) = \frac{2}{q\varepsilon_s}\left(\frac{\Delta\left[1/C^2(\omega)\right]}{\Delta V_{bias}}\right)^{-1}, W = \frac{\varepsilon_s}{C(\omega)} \tag{5.1}$$

After a 1 minute UV exposure, the impedance of the same device changes drastically: the magnitude of the impedance decreases and the real part becomes significant (Fig. 5.3a blue points). The Nyquist plot is composed of two partial semicircles, one of which is centered off of the x-axis (commonly called a depressed semicircle), indicating the presence of a constant phase element (CPE). This indicates that UV exposure generates mobile ions in the ZnO layer. To fit this behavior, we must change the equivalent circuit dramatically: the capacitance component of the ZnO layer is short circuited by a resistor R_p, and a second component composed of a parallel CPE Q_{ps} and resistor R_{ps} appears (Fig. 5.3c). The impedance of the CPE Z_{CPE} is defined by Eq. (5.2), where $n = 1$ is an ideal capacitor and $n = 0$ is an ideal resistor, and Q_{ps} is the magnitude of the admittance.

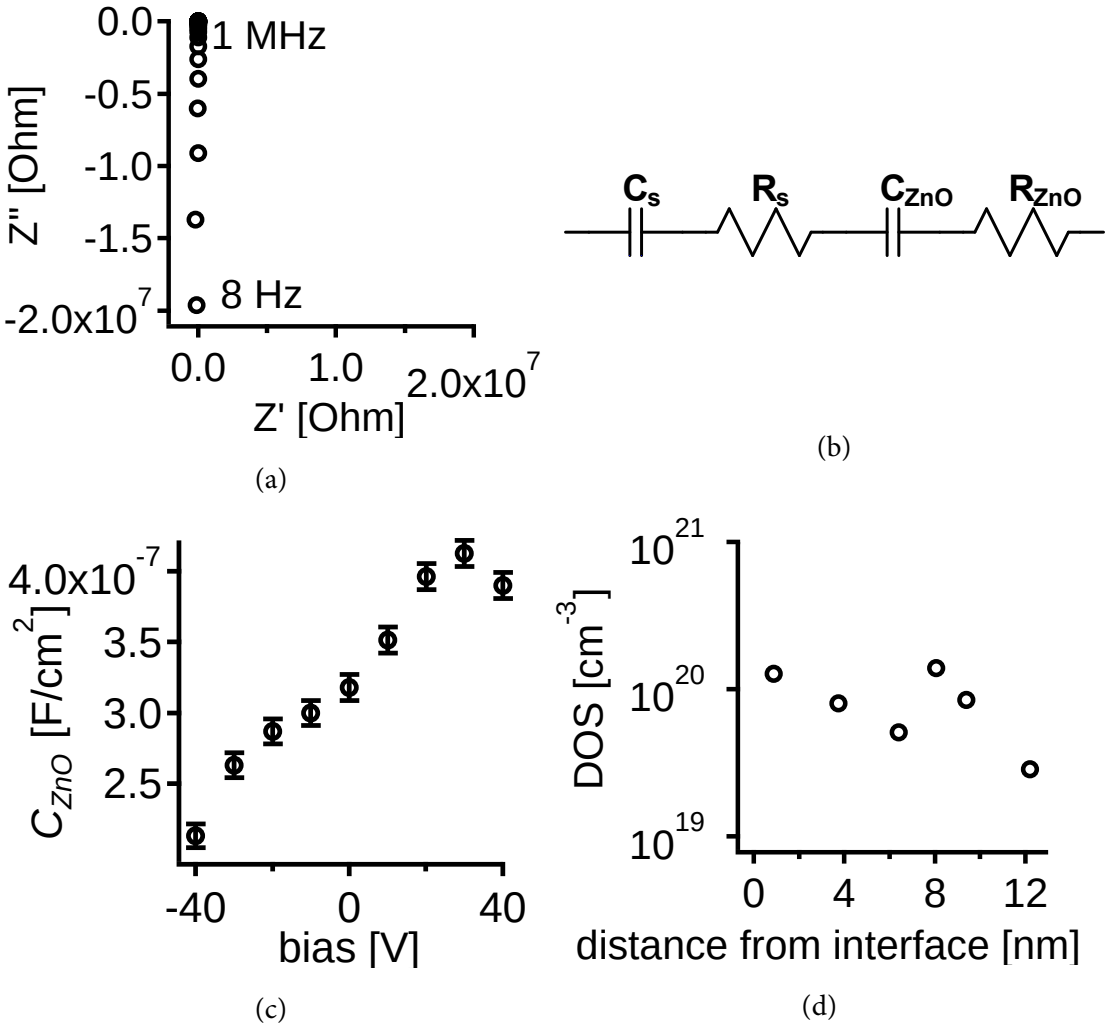

Figure 5.2: (a) Nyquist plot of $Si^{++}/SiO_2/ZnO/Ag$ device at zero bias before UV exposure. (b) Equivalent circuit before UV exposure. (c) Modeled parameter C_{ZnO} as a function of applied bias. (d) Density of trap states in ZnO as a function of distance from the SiO_2/ZnO interface at zero bias before UV exposure.

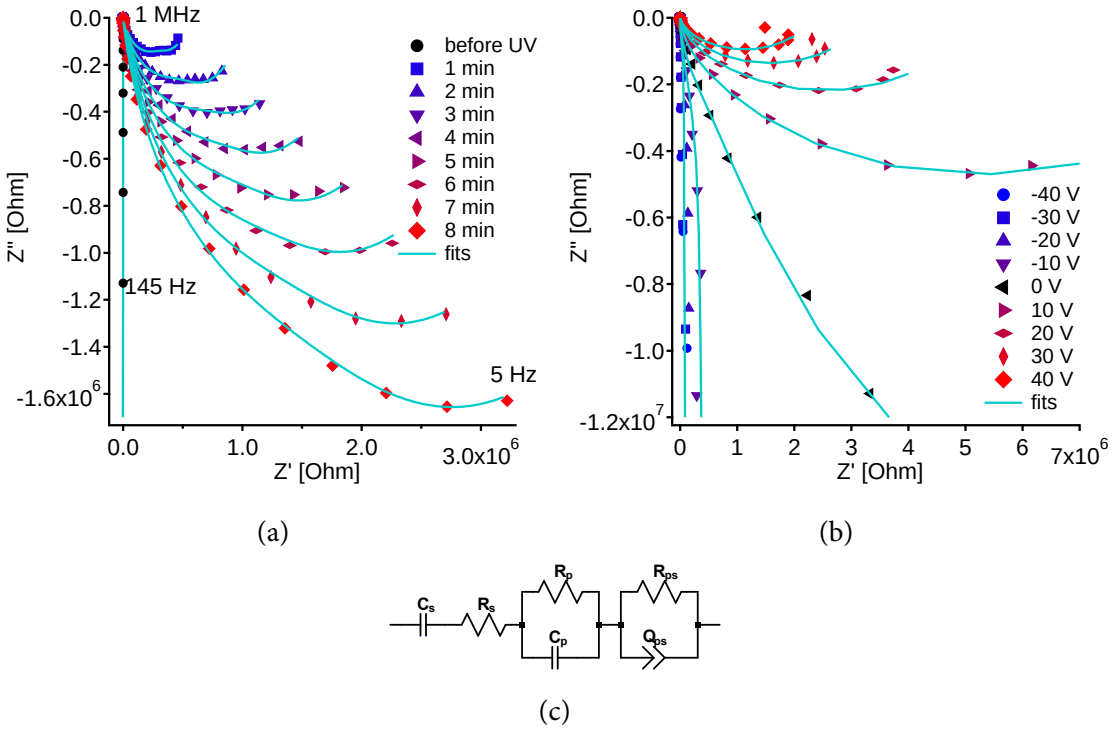

Figure 5.3: (a) Nyquist plots of $Si^{++}/SiO_2/ZnO/Ag$ after UV exposure, at zero direct bias after exposure to 254 nm light and recovery for various amounts of time. (b) Nyquist plots at various direct biases on Si after exposure to 254 nm light and recovery for 40 minutes. (c) Equivalent circuit used to fit impedance behavior.

$$Z_{CPE} = \frac{e^{-\frac{\pi}{2}ni}}{Q_{ps}\,\omega^{n}} \tag{5.2}$$

When the sample is left in the dark over time, the device approaches its pre-UV behavior with Z" > Z' (Fig. 5.3a). The circuit parameters as a function of time after UV

exposure (Fig. 5.4a) show that the ionic conduction disappears as oxygen is readsorbed, n approaches 1, while Q_{ps}, R_p, and R_{ps} increase.

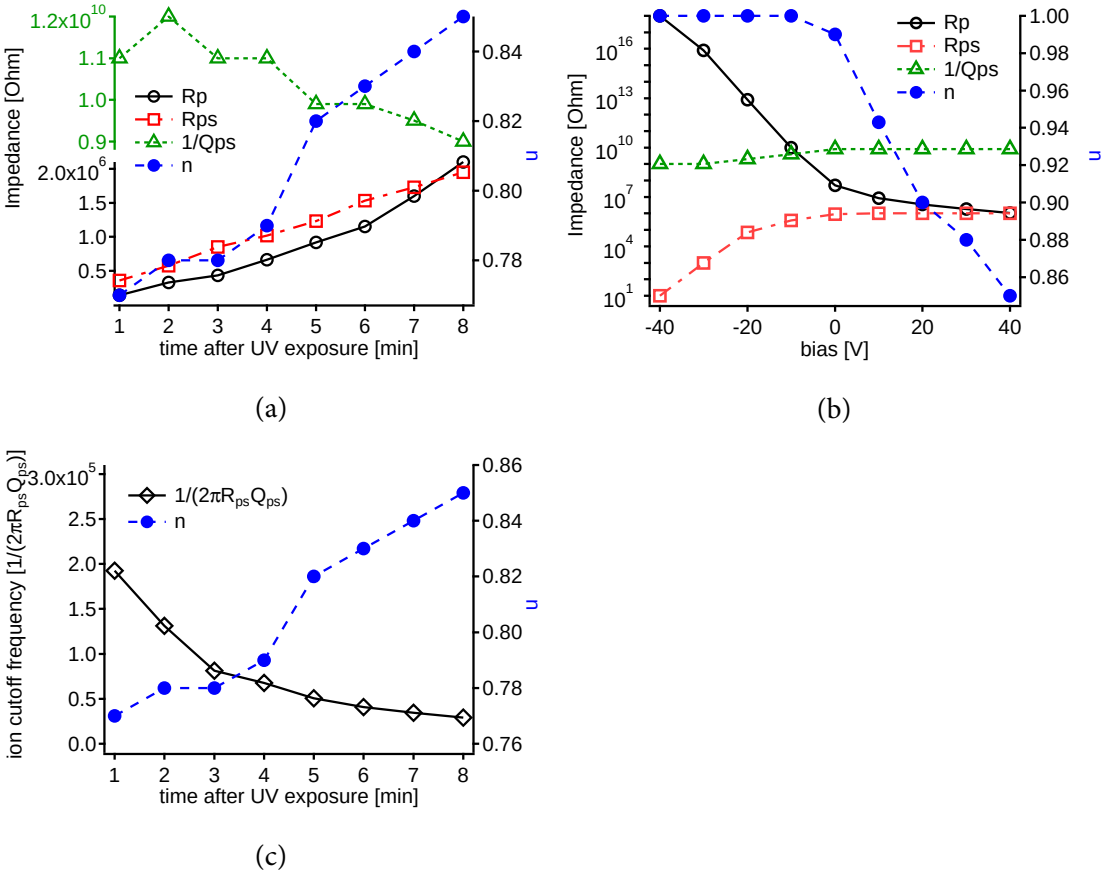

Figure 5.4: (a) Equivalent circuit parameters of $Si^{++}/SiO_2/ZnO/Ag$ devices from fits of impedance at zero direct voltage after exposure to 254 nm light and recovery for various amounts of time, (b) at various direct voltages after exposure to 254 nm light and recovery for 40 minutes. (c) RC cutoff frequency after recovery for various amounts of time.

After a recovery period of 40 minutes, a positive bias on the Si side of the device increases ionic conduction and a negative bias decreases it (Fig. 5.3b). The equivalent circuit parameters as a function of bias reveal information about the mobile ions (Fig. 5.4b). If negative bias is applied to the Si, n is close to 1, while if positive bias is applied, n decreases. The CPE can be thought of as many capacitors in parallel with different inter-charge distances, and in our samples these charges could be Zn and O ions. Possible causes for n to move closer to 1 are: i) the disappearance of mobile ions or ii) the movement of the ions due to the direct bias so that they all have the same inter-charge distance, allowing them to be treated as one large capacitor. When negative bias is applied to the Si, positively charged ions would be expected to move towards the SiO_2/ZnO interface while negatively charged ions would be expected to move away from this interface. Since Q_{ps} increases with negative bias, it is likely that the ions are approaching the interface rather than receding from it or disappearing. As *a*-ZnO exhibits negligible hole mobilities, we believe that the positive ions are mobile af f > 5 Hz while the negative ions are not. The PPC due to mobile ions likely occurs concurrently with the previously mentioned known mechanisms for PPC. It seems likely that these are Zn^{2+} and Zn^{1+} ions which have a low formation enthalpies and migration barriers in crystalline ZnO of less than 1.7 eV[184] but possibly also protons which originate from bulk hydrogen intersitials[176] or from interfacial hydroxide adsorbates.

Fig. 5.4c reveals more information about the rebonding behavior of the ions. The alternating field brings the photogenerated zinc and oxygen (and possibly other) ions closer and further apart, and if these ions come close enough for a long enough time they will reform ZnO. At field frequencies below the ion cutoff frequency $1/(2\pi R_{ps} Q_{ps})$, the reaction rate is fast, while at frequencies above it the reaction rate is slow. The cutoff frequency decreases as a function of time after UV exposure, while n increases. The decreasing cutoff frequency tells us that the oxygen does not only exist as one type of ion homogeneously distributed in the film. One explanation is that oxygen has accumulated at one side of the ZnO film, likely atmospheric oxygen at the exposed surface. Right after UV exposure, there is enough oxygen next to the zinc ions so even at relatively high frequencies, reactions are occurring rapidly. But over time this oxygen is depleted and the alternating field has to move ions from further away to have them react. It is also possible that the various ions have different reaction rates, and the ones with faster rates are depleted faster, decreasing the cutoff frequency.

Photodetectors with persistent photoconductivity in interfacial layer

We take advantage of PPC to build organic bulk heterojunction photodetectors with an additional *a*-ZnO layer, which causes the dark current to stay high for some time after UV exposure, potentially allowing for low power sensors that have a long, and as we will explain later, adjustable, polling interval (Fig. 5.1a). As with our previously published

work on photodetectors,[185] we use an inverted structure in which the incident light goes through the top Ag anode instead of going through the glass/ITO as in typical organic solar cells. This prevents absorption of UV light by the glass/ITO and improves the figures of merit at UV wavelengths. The inverted design also allows for easier integration with circuit boards on arbitrary substrates.

Before UV exposure, both the dark and the light current for devices with and without the *a*-ZnO layer are very similar (red and black lines in Figs. 5.5a and 5.5b). Two figures of merit typically used to evaluate the performance of photodetectors are responsivity and detectivity. Responsivity R_λ as a function of wavelength λ is calculated by:

$$R_\lambda = \frac{\eta e \lambda}{hc} \tag{5.3}$$

and specific detectivity D^*_λ is calculated by:

$$D^*_\lambda = \frac{R_\lambda}{\sqrt{2eJ_{\text{dark}}}} \tag{5.4}$$

assuming that shot noise is the dominant noise source. η is the external quantum efficiency, J_{dark} is the dark current density, e is the elementary charge, h is Planck's constant, and c is the speed of light. Because the thin ZnO layer does not absorb much UV light, the absorbance of devices with and without ZnO are very similar, and the responsivities are also very similar. For a device on which external quantum efficiency was measured, the device without ZnO has a slightly higher light current in reverse bias (-0.5 V on the Ag electrode) and thus slightly better responsivity (Fig. 5.6 inset). The specific de-

tectivities (calculated using the initial dark current) are also almost identical (Fig. 5.6), but in this case the initial dark current of the device with ZnO is lower and thus its detectivity is slightly better. These figures of merit are comparable in the UV to other organic photodetectors[185,186] and to Si photodetectors, but lower than purely inorganic ZnO photodetectors.[155]

However, because the dark current of devices with ZnO increases by several orders of magnitude after exposure to above-band gap light (Fig. 5.5d), the specific detectivity calculated using the post-UV dark current is much lower. The previously mentioned causes for PPC in ZnO, including ionic photoconductivity, likely contributes to this increase in dark current. Also, the applied bias may cause the mobile positive ions in ZnO to move to the interface with P3HT:PCBM, causing holes to be injected into the P3HT:PCBM (see arrows in Fig. 5.1a). Finally, as ZnO has a low density of states (about 1×10^{19} cm^{-3}), a small change in the density of states due to UV exposure can move the Fermi energy a significant amount. The dark current of devices without ZnO does not change post-UV.

The dark current of photodetectors with ZnO recovers much faster in ambient conditions than when stored in a nitrogen glovebox. After exposure to the xenon arc lamp approximating AM 1.5 for about 1 minute with about 7×10^{15} photons cm^{-2} s^{-1} incident on the active area, it takes about 2 days for devices in nitrogen to mostly recover (Fig. 5.5b), while in air the devices are already mostly recovered immediately after exposure and recover further after 1 day in air (Fig. 5.5c).

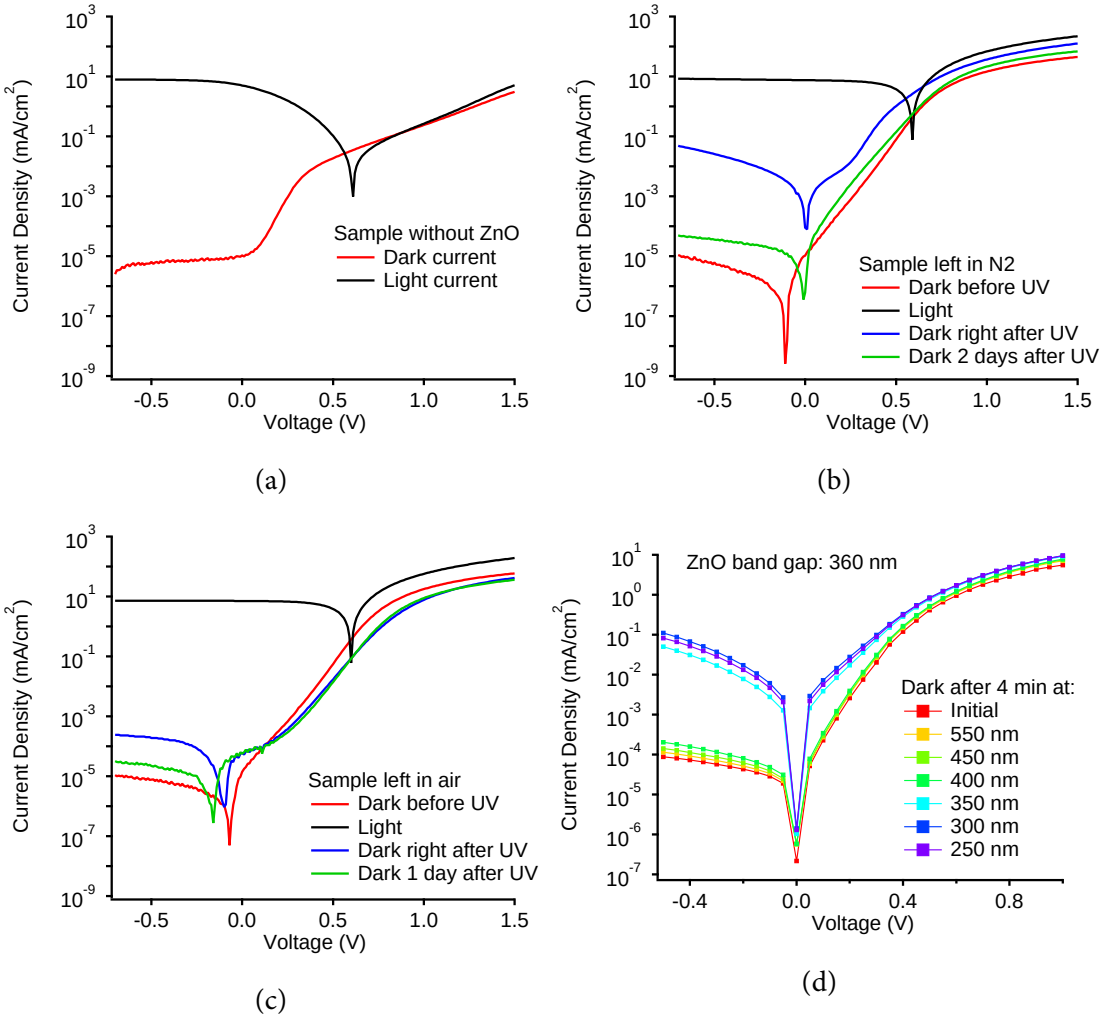

Figure 5.5: Current density of glass/Al/ZnO/P3HT:PCBM/MoO_3/Ag photodetectors, (a) without ZnO in nitrogen, (b) with ZnO in nitrogen dependent on light exposure and time, (c) with ZnO in ambient atmosphere, (d) dark current with ZnO in nitrogen after excitation at various wavelengths.

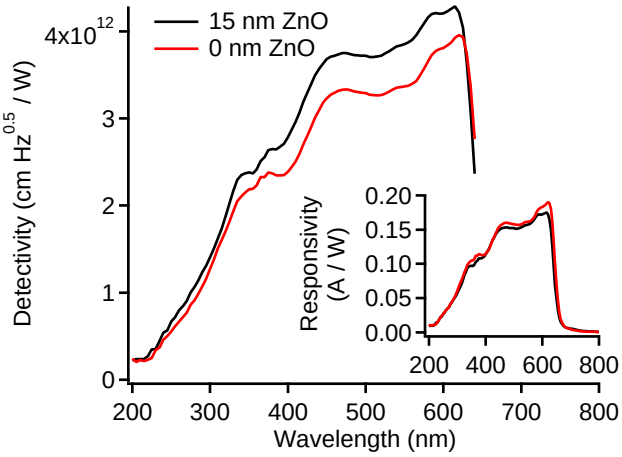

Figure 5.6: Specific detectivity (calculated using initial dark current) of glass/ZnO/P3HT:PCBM/MoO_3/Ag photodetectors at -0.5 V applied bias.

To better quantify the effect of UV exposure on the ZnO photodetectors, the light and dark current was measured at -0.5 V on the Ag electrode during exposure to a UV LED pulsed at 2 Hz (Fig. 5.7). The dark current recovery after the LED was shut off was also measured. This measurement provides a lower incident intensity than the xenon arc lamp and more control over exposure time. The emitted power of the LED was 1.26 mW cm^{-2} at the sample location, and we calculate that about 2% of the photons incident on the active area of each pixel are absorbed by the ZnO layer. In a nitrogen environment, both the dark and light current increase with the amount of time the device is exposed to UV, with an additional minor effect that some recovery is likely taking place during the dark intervals. But under ambient conditions, the dark current remains steady with UV exposure.

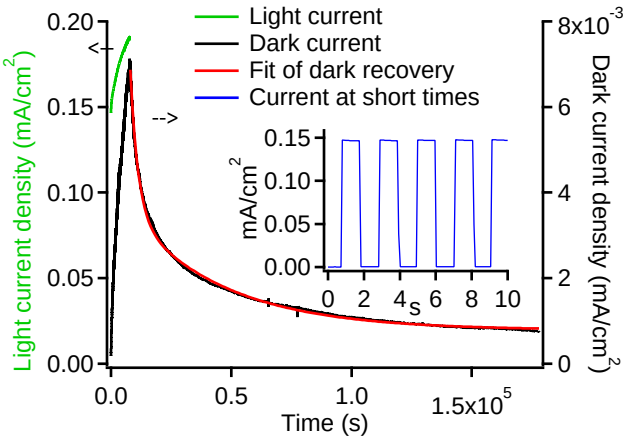

Figure 5.7: ZnO photodetector current densities in nitrogen, under pulsed UV LED illumination and after LED is shut off, at -0.5V applied bias.

After the UV LED was shut off, it took a little less than two days for the dark current of the photodetector under nitrogen to return to 110% of its initial value. Empirically, the light and dark current rise and dark current decay all fit several functions relatively well: the sum of two exponentials, a stretched exponential, or a power law function. We propose that in our system the oxygen readsorption to the surface and the reformation of Zn-O bonds are responsible for the two time constants. Similar behavior has been seen in the literature. Liu et al. found that the sum of two exponentials fits the dark current decay of ZnO photoconductive detectors[187] (although in our case the decay is much slower because of the ZnO is amorphous and much thinner). They concluded that slow detrapping of holes was responsible for the decay time, but also suspected that oxygen adsorption at the surface might affect the decay time. Reemts et al. found that

electrodeposited porous ZnO films had a light current rise and a dark current decay that both fit stretched exponential fits, and they attribute this to lattice relaxation of surface states as the cause of PPC.[188] Finally, Su et al. found that simple exponential decay fits the dark current decay of ZnO photoconductive detectors.[178]

The PPC behavior of our photodetectors means that they can be used as low-power UV photodetectors in a non-traditional fashion, especially if low time resolution is not a problem. The device should be kept in an oxygen-free environment and the initial dark current measured. When the device is polled, based on the measured current and its history one can determine whether the device is presently exposed to light, or is now in the dark but recently was exposed to UV light, or none of the above. If low time resolution is not a problem, the device can be polled at intervals of up to a couple of days, which will reveal whether it was exposed to UV light at any time during this period. Furthermore, while the light current is sensitive to both UV and visible light, the dark current is only sensitive to UV light, making it unnecessary to use a filter to block visible light. For this use it would be beneficial to protect the device against oxygen to increase the minimum polling interval required. But once UV exposure has been read out, it would be favorable to expose the devices to oxygen to reset them and allow them to detect again. In the next section we explore another device structure that could be used for UV photodetectors as well as the use of an oxygen hindering layer.

Thin film transistors with persistent photoconductivity

We now investigate the effect of PPC on TFTs with an *a*-ZnO semiconducting layer and show that a reduction in onset voltage can be used to sense UV light (Fig. 5.1b). We also investigate the use of a polymer oxygen-hindering layer to change the recovery behavior of the TFTs after UV exposure. We chose P3HT as this layer for an initial study in order to relate TFT behavior to the bulk heterojunction photodetectors. This device geometry allows us to alter the *a*-ZnO top interface to hinder oxygen without altering charge injection in the device.

Before UV exposure, adsorbed oxygen ions (and possibly other species such as hydroxide or water) on the top surface of the ZnO film at the TFT back channel trap electrons, depleting the film and making it insulating. This necessitates a large positive gate voltage to displace the back channel field and fill the trap states in order to accumulate mobile electrons towards the gate and create a conductive channel (Fig. 5.8a). The onset voltage increases with further measurements possibly because the positive gate field is not completely screened at the back channel surface, which causes more oxygen to be adsorbed.

According to the aforementioned mechanisms for PPC, directly after UV exposure, oxygen is desorbed and electrons are no longer trapped, so the channel is conductive at zero gate voltage, and negative gate voltage is required to deplete the channel (Fig. 5.8b). Also, UV exposure may break Zn-O bonds and increase the number of free electrons.

Finally, breaking Zn-O bonds creates mobile ions that are free charge carriers, further decreasing onset voltage. The on-off ratio is decreased, possibly because of the mobile ions. In subsequent measurements, the onset voltage and on-off ratio starts to recover to their previous values, as oxygen is readsorbed/rebonded and mobile ions disappear (Fig. 5.8c). The effect of UV exposure on the onset voltage means that these TFTs could be used as UV photodetectors.

A change in onset voltage was also seen in InGaZnO and InZnO TFTs where light and negative bias generated positive and negative ions at the gate interface and the back channel respectively,[189] but our findings suggest an alternative explanation, that the ions were produced everywhere and transported to the interfaces by the bias.

The presence of a P3HT layer covering the ZnO surface affects the TFT behavior (Fig. 5.8c). Before UV exposure, devices with a P3HT layer have a lower onset voltage that changes less with further measurements compared to devices without. This is likely because the P3HT layer has blocked some oxygen from adsorbing to the ZnO and because the P3HT causes accumulation due to a band offset at the interface between the ZnO back channel and the P3HT. Band offsets in TFTs at a nanoparticle ZnO/polymer interface[190] and for *a*-ZnO[179] are discussed in previous literature.

After UV exposure, devices with the P3HT layer continue to have a lower onset voltage compared to devices without P3HT, because oxygen reuptake is slowed. Transfer curves of the other device types (reference devices with ODCB surface treatment as well as those

with a P3HT layer annealed at a lower temperature of 80°C) are in the SI. This behavior shows that a more effective oxygen blocking layer could be used to slow the recovery rate in both the photodetector and TFT UV photodetectors. This layer would allow for a reduction in the required polling time for these photodetectors in order to save power, especially under ambient conditions. Finally, a reset of the ZnO layer after UV exposure and readout could be achieved with an oxygen blocking layer which releases the oxygen upon applying a bias.

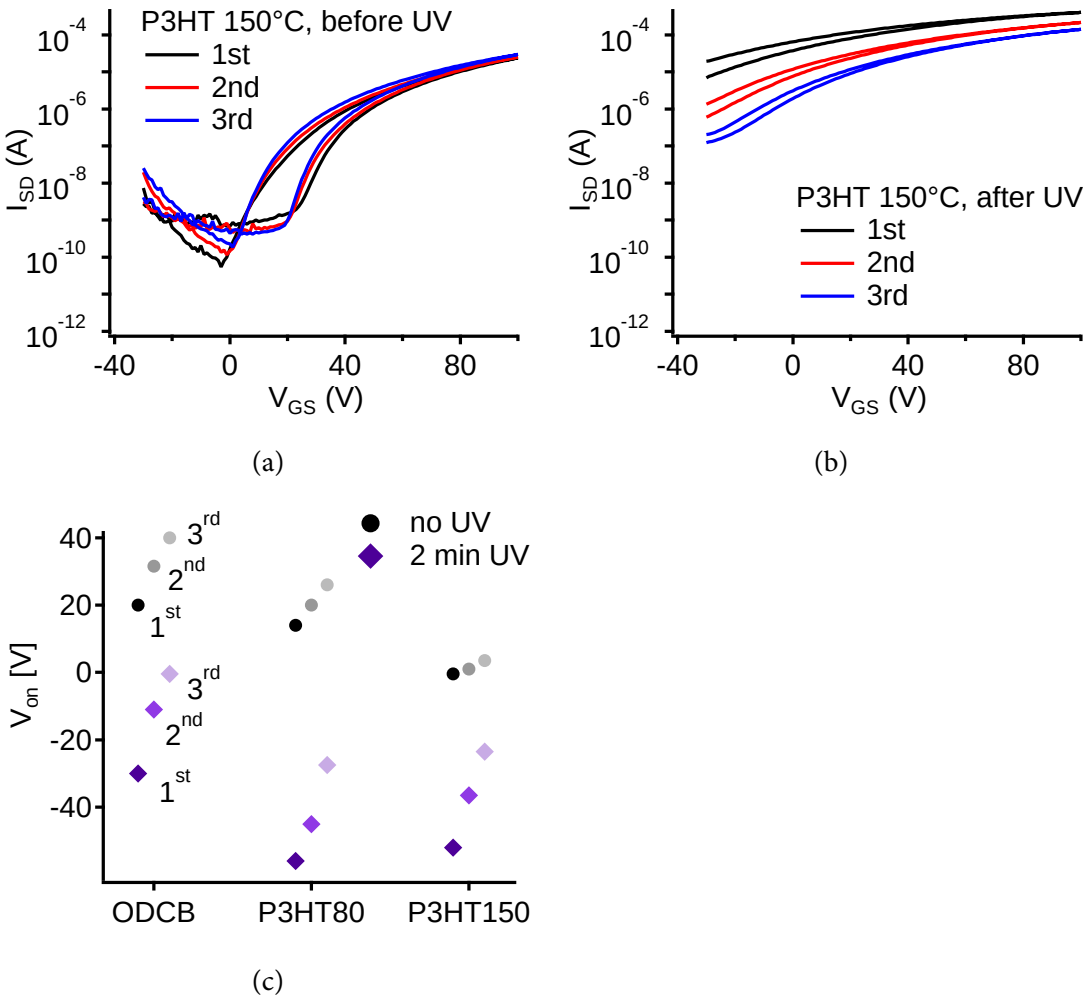

Figure 5.8: Three consecutive measurements of transfer curves of Si/SiO_2/ZnO/Al/P3HT(150°C), (a) before and (b) after UV exposure at 254 nm for 2 minutes, and (c) onset voltages for devices with ODCB, P3HT annealed at 80°C, and P3HT annealed at 150°C on top of the Al.

5.1.4 Conclusion

In this work, we have demonstrated through impedance measurements that UV exposure of *a*-ZnO films generates mobile positive ions which contribute to PPC, in addition to the known effects of oxygen desorption and photolysis. The PPC significantly affects the behavior of *a*-ZnO TFTs and hybrid *a*-ZnO/P3HT:PCBM photodetectors. Recovery of the pre-UV device behavior is rapid in an ambient atmosphere but slow in a nitrogen atmosphere, and is slowed by an oxygen hindering layer. These findings lead to the potential for UV- or oxygen-sensing devices that can be polled less frequently, leading to lower power consumption.

5.1.5 Supporting Information

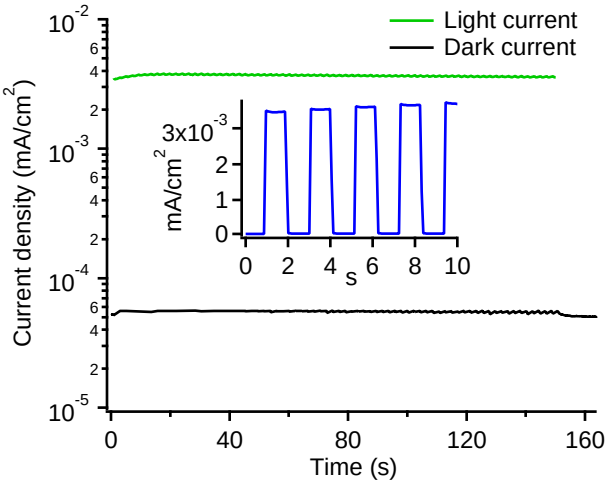

Figure 5.9: ZnO photodetector current densities in ambient atmosphere, under pulsed UV LED illumination and after LED is shut off, at -0.5V applied bias.

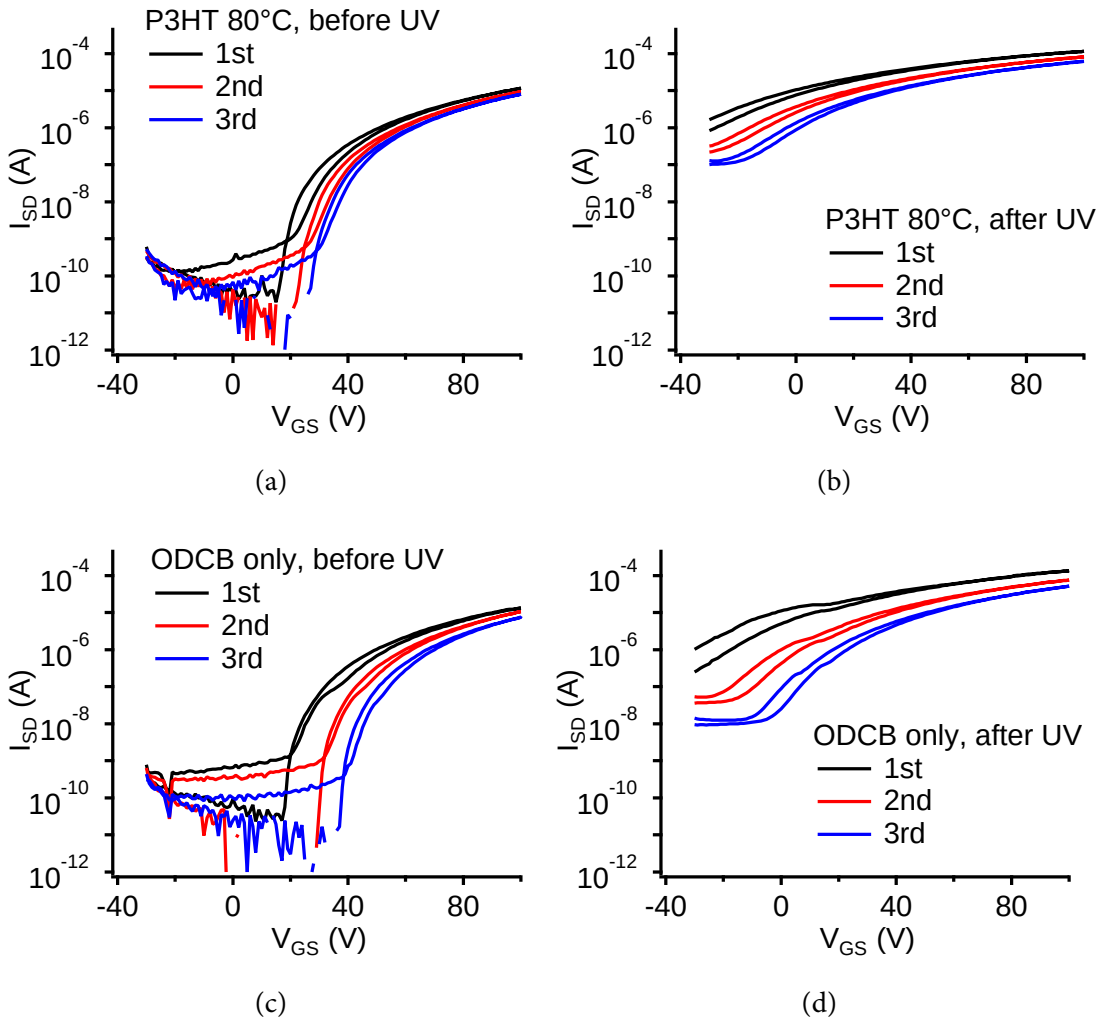

Figure 5.10: Three consecutive measurements of transfer curves of (a-b) $Si/SiO_2/ZnO/Al/P3HT(80°C)$, (c-d) $Si/SiO_2/ZnO/Al/ODCB$, before and after UV exposure at 254 nm for 2 minutes.

5.2 Characterization of Solar Cells Utilizing Low Band Gap Donor-Acceptor Copolymers

A co-author developed a facile and scalable synthetic route to a soluble dithieno[3,2-b:2′,3′-d]thiophene (DTT) unit, which utilizes a Stille-coupling reaction to efficiently synthesize the bisthienylsulfide intermediate. This simplifies the overall DTT synthesis and increases yield, facilitating the use of DTT as a donor unit in low-bandgap polymers. Solution processable alternating D-π-A-π polymers (DTTBTO and DTTDPP) have been synthesized with DTT as the donor unit and either a benzothiodiazole derivative (BTO) or fused ring 1,4-diketopyrrolo[3,4-c]pyrrole (DPP) serving as the acceptor unit. We characterized these materials and optimized solar cells using solvent additives, giving us a better understanding of structure-property relationships to be applied to the design of high performance organic solar cells.

5.2.1 Introduction

Technologies that directly convert sunlight into electricity are attractive sources of clean, renewable energy. One of the most promising of these technologies is thin film, polymer-based organic photovoltaic devices (OPV)[2] which can be fabricated by low-cost, solution processing methods over large areas and on flexible substrates. Due to recent advances in conjugated polymer design and device fabrication techniques, the

efficiencies of polymer-based photovoltaic devices are approaching 10% - the minimum often considered to make the technology commercially relevant on large scale. These advances in photoconversion efficiency directly result from more complete absorption of the solar spectrum and a greater control of the active layer morphology.[100,191,192] One of the future challenges is to develop new p-type conjugated polymers that possess (a) sufficient solubility to enable solution processing, (b) a broad and intense absorption profile across the solar spectrum and (c) a large free charge carrier mobility for facile charge transport.

Appropriate choice of monomers in the backbone of a semiconducting polymer can push their optical absorbance towards the near-infrared. One strategy is to incorporate electron-rich donor units and electron deficient acceptor segments in the polymer backbone.[193] Through the "push-pull" interaction, the energy gap of the conjugated polymers decreases thus shifting the absorption band to lower energy. Another strategy is to introduce monomer units with quinoidal character into the conjugated system, which can reduce the band gap and enhance π-π stacking.[194] Fused thiophene ring systems are well-known to stabilize this quinoidal structure[195,196] and alternating polymers containing fused thiophene units, such as thieno[3,4-b]thiophene,[120,121,197] and dithieno[3,2-b:2',3'-d]silole,[198] have achieved efficiencies of about 7%.

Recently, oligomers that incorporate a new donor building block - the dithieno[3,2-b:2',3'-d]thiophene (DTT) unit - have demonstrated high mobility due to the planarity

and favorable sulfur-sulfur interactions for the fused DTT repeat unit.[199–201] However, the synthesis of DTT-based monomers is plagued by low yields resulting from inefficient reactions over a dozen steps. One such example is reported by He and coworkers, which utilized a ketone-based ring closure procedure for the synthesis of DTT.[201] This strategy requires double annulation reactions, which are often low-yielding and unreliable. Li et al. used an alternative method to synthesize DTT based on a single ketone-based ring closure procedure.[202] However, this method requires a greater number of synthetic steps, which limits its scalability and significantly lowers the overall yield. As a result, the development of a simple and efficient method to synthesize the DTT unit is a necessity for further investigation of this promising electron-rich unit.

In this report, a reliable and scalable synthetic route to the DTT building block is demonstrated. This synthetic route utilizes a Stille-coupling reaction to efficiently synthesize the bisthienylsulfide intermediate and simplifies the overall strategy (four steps with a yield of 44%). This facilitates the use of DTT as a donor unit to construct low-bandgap polymers with two different acceptors: a benzothiodiazole derivative (BTO)[203] and the fused ring 1,4-diketopyrrolo[3,4-c]pyrrole (DPP).[204,205] A D-π-A-π alternating copolymer strategy was utilized by introducing a thiophene π-spacer between the donor and acceptor to relieve steric hindrance and achieve increased conjugation. Through this strategy, soluble, high molecular weight D-π-A-π alternating copolymers with broad,

near infrared absorption were prepared and employed in the fabrication of efficient photovoltaic devices.

5.2.2 Results and Discussion

Material Synthesis

The D-π-A-π polymers DTTBTO and DTTDPP were synthesized by Sung-Yu Ku in Prof. Craig Hawker's group. The details will not be discussed here except to say that the notable characteristics of the synthesis route are better yields with fewer steps than the previously used approaches. The DTT intermediate is formed by Stille coupling on 3-bromo-4-dodecylthiophene to form the bisthienylsulfide intermediate and then ring closure to form DTT, instead of the previously used double annulation approach on a diketothiophene intermediate. DTT was successfully synthesized in four steps with an overall yield of 44% from commercial available 3-dodecylthiophene. This represents a significant improvement over previous strategies[201,202] and now allows multi-gram (10+ g) quantities of DTT to be routinely prepared.

The successful development of a facile and scalable route to DTT-based monomers now permits the exploration of this fused ring system in the synthesis of conjugated polymers, an area that has received little attention. From the limited literature, it is apparent that the main challenge for DTT-based copolymers is a relatively large energy gap, resulting in inefficient utilization of the solar spectrum. For example, an alternating

D-A copolymer consisting of DTT and benzothiadiazole (BT) has a narrow absorption spectrum (absorption onset of 600 nm) that does not utilize the majority of the solar spectrum.[206] In order to broaden the absorption spectrum, Patil et al. reported D-π-A conjugated copolymers based on DTT and 2,3-bis((4-octyloxy)phenyl)-5,8-dithien-2-ylquinoxaline that increased the absorption edge to 700 nm through the introduction of thiophene π-spacer groups.[207] The success of this π-spacer strategy promoted the use of a similar strategy in the design of DTT monomers. The conjugation length of the DTT is extended with thiophene units, and a benzothiodiazole derivative (BTO) and the fused ring 1,4-diketopyrrolo[3,4-c]pyrrole (DPP) were chosen as two different acceptors to construct low-band-gap polymers.

Significantly, all polymers showed good solubility (greater than 20 mg/mL) in chlorinated solvents, which is essential for high quality film formation using solution processing. The molecular weight and polydispersity index (PDI) of the polymers were measured by GPC and calculated using polystyrene standards with DTTBTO having a number-average molecular weight, M_n, of 12 000 amu (PDI = 2.1) and DTTDPP having a significantly higher number-average molecular weight (M_n = 114000 amu; PDI = 1.6). The increase in M_n for DTTDPP is proposed to be a result of the decreased steric interactions due to the two flanking thiophenes which have no substituents in the 3 and 4-positions when compared to DTTBTO which has a phenyl ring with alkyloxy substituents in the 5 and 6-positions.

Physical properties

Thin films (about 55nm) were prepared by dissolving the polymers in o-DCB followed by spin coating. The absorption spectrum of the resulting thin films is reported in Fig. 5.11 with the DTTBTO showing a broad absorption from 400 to 700 nm with maximum absorption peaks at 425 nm and 595 nm from the second and first excited states respectively. The absorption onset of DTTBTO is 701 nm, and the optical band gap (E_g^{opt}) can be calculated as 1.77 eV. Significantly, substituting the DPP acceptor for the BTO acceptor to form DTTDPP resulted in a shift of the absorption edge from 700 nm to 891 nm and associated lowering of the optical band gap to 1.39 eV.

Electrochemical properties

The frontier energy levels of semiconducting polymers are significant parameters for the design and modification of the polymeric repeat units in order to optimize photovoltaic devices. In this way, the energy gap between the HOMO of the p-type polymer and the LUMO of the n-type fullerene set an upper bound for the open circuit voltage (Voc). The LUMO level of the p-type polymer must be offset, above that of the fullerene, to prevent charge trapping. The LUMO energy levels for the copolymers described above were obtained by cyclic voltammetry in o-DCB solution (Fig. 5.12). We obtain LUMO levels for DTTBTO and DTTDPP of 3.35 eV and 3.60 eV, respectively. The HOMO levels were estimated by subtracting the value for the optical bandgap (determined from the

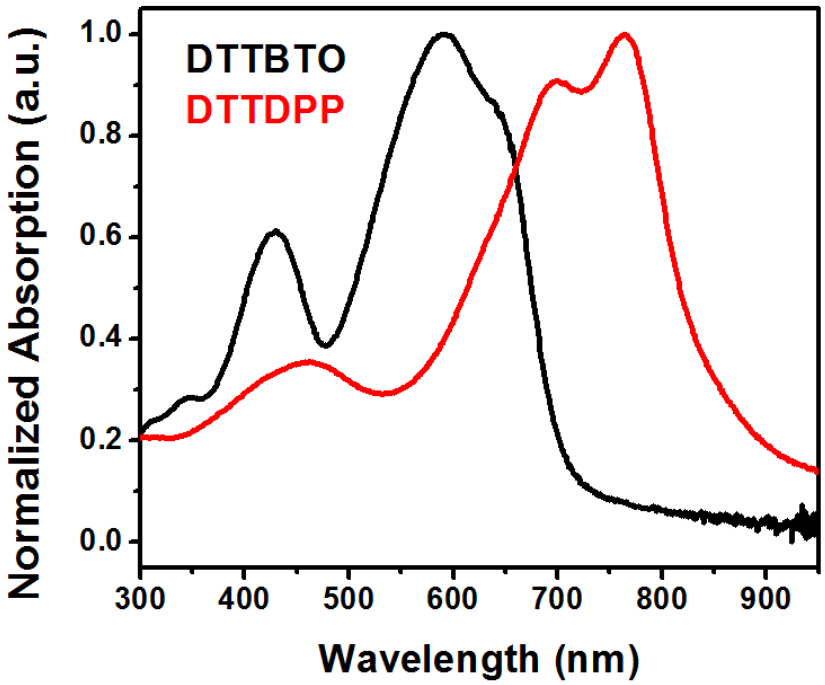

Figure 5.11: Thin film absorption spectra for the DTTBTO and DTTDPP D-π-A-π copolymers.

absorption edge in the thin films) from the LUMO energy levels; these values have the uncertainty of the exciton binding energy, which is about 0.4 eV in many cases, and are likely underestimates.[208] The estimated HOMO values still allow relative trends in Voc to be predicted. The polymers' HOMO levels (DTTDPP ~ 4.99 eV, DTTBTO ~ 5.12 eV) are ~ 0.3 eV and ~ 0.4 eV deeper than that of P3HT (4.72 eV)[18] respectively. The polymers' LUMO levels (DTTDPP: 3.60 eV, DTTBTO: 3.35 eV) are ~ 0.6 eV and ~ 0.55 eV deeper than that of P3HT (2.81 eV)[18] respectively, resulting in increased absorption without a

corresponding loss in Voc. A summary of the optical and electrochemical properties for the donor-acceptor copolymers is shown in Table 5.1.

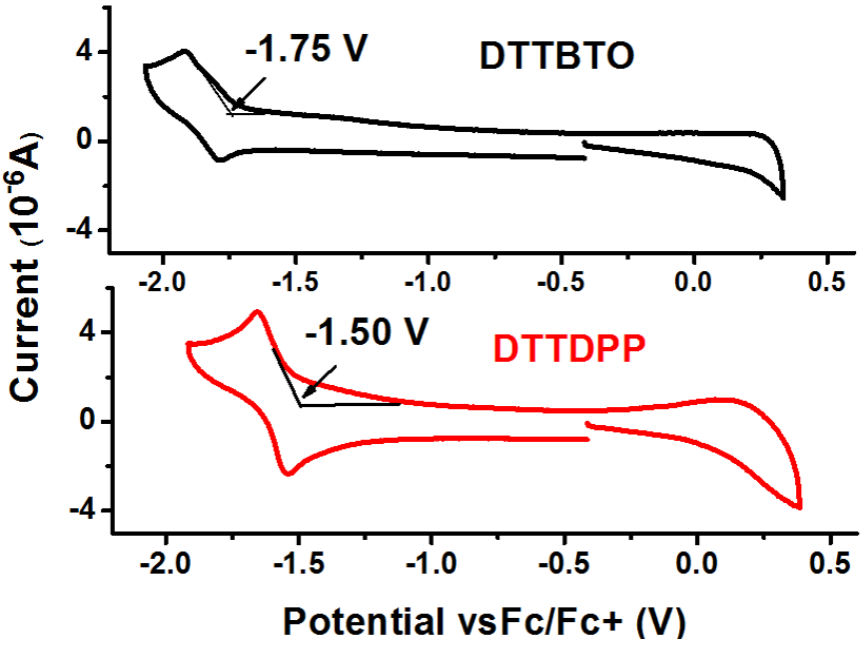

Figure 5.12: Cyclic voltamograms for the donor-acceptor copolymer, DTTBTO and DTTDPP ~ 1mg/mL o-DCB; working electrode: carbon electrode; counter electrode: Pt, reference electrode: Ag; 0.1M nBu4NClO4.

Electrical Performance

Thin Film Transistors. The electrical performance of these materials were initially examined as p-type thin film transistors (TFTs). Both as-cast and annealed films of DT-TBTO and DTTDPP where the annealing temperature was chosen as 150°C based on

Film	Onset [nm]	E_g^{opta} [eV]	E_{red}^{b} [eV]	LUMO [eV]	HOMO [eV]
DTTBTO	701	1.77	-1.75	3.35±0.4	5.12±0.4
DTTDPP	891	1.39	-1.50	3.60±0.4	4.99±0.4

Table 5.1: Summary of optical and electrochemical properties of D-π-A-π polymers. (a) $E_g^{opt} = 1239/\lambda^{\text{onset}}$; (b) potential determined by cyclic voltammetry in 0.1M Bu4NClO4–o-DCB vs. ferrocene/ferrocene+; (c) LUMO = E_{red} + 5.1 [eV]; d. HOMO = LUMO + E_g^{opt}.

the solvent boiling point (details of device processing and raw current-voltage data are presented in S. I.) were examined. As-cast films of DTTBTO were poorly conductive, but after annealing at 150°C for 30 min under nitrogen, improved current-voltage characteristics were observed with average saturation mobilities of 5.1×10^{-4} cm^2 V^{-1} s^{-1}, threshold voltages, V_T, of -13.0 V, and current on-off ratios $I_{on/off}$ of 10^2. In contrast, both the as-cast and annealed films of DTTDPP showed conventional current-voltage characteristics. As-cast devices possessed average saturation mobilities of 2.8×10^{-2} cm^2 V^{-1} s^{-1}, V_T of -1.6 V, and $I_{on/off}$ of 10^3. Annealed devices showed a slight increase in average saturation mobility to 3.3×10^{-2} cm^2 V^{-1} s^{-1}, a negative shift in V_T to -4.8 V, and comparable $I_{on/off}$, 10^3.

Photovoltaic properties. Bulk heterojunction solar cells were fabricated using DTTDPP and DTTBTO as the donors and PC71BM as the acceptor. Solar cells were fabricated us-

ing DTTDPP:PC71BM in 1:1, 1:2 and 1:3 weight ratios with Ca/Al electrodes (fabrication details and structure are presented in the SI). The best devices that contained no additives were composed of DTTDPP:PC71BM (1:2), yielding an efficiency of 1.01% with a Voc of 0.64 V, Jsc of 2.39 mA cm^{-2} and FF of 0.67 (Fig. 5.13a (black trace)). Significantly, the photovoltaic devices consistently had fill factors higher than other low bandgap polymers,[120,121,197,198] suggesting efficient free charge carrier transport and collection. However, the low photocurrent for the DTTDPP:PC71BM device leads to lowered efficiency with the high fill factor suggests that inefficient charge generation is limiting the short circuit current. Atomic force microscopy (AFM) analysis of the BHJs processed from o-DCB revealed large domains of polymer and fullerene likely leading to inefficient generation due to the relatively low interfacial area, (Fig. 5.14a and c). High boiling point additives, such as 1,8-diiodoctane (DIO) and 1-chloronaphthalene (CN), were then used to modify the polymer:fullerene phase separation and increase interfacial area.[121,209] As expected, the active layer from the 1:1 and 1:2 blends processed with 9 vol.% CN additive in o-DCB show finer morphological features and increased interfacial area (Fig. 5.14b and d) leading to an increased efficiency of 2.35% with a Voc of 0.61 V, Jsc of 6.10 mA cm^{-2} and FF of 0.67 (Fig. 5.13a (red trace)). Similarly, addition of 3% vol. DIO gave finer nanoscale morphology with a corresponding improvement in Jsc to 5.28 mA cm^{-2} and efficiency to 1.77%.

DTTDPP:PC71BM	Additive	V_{oc} [V]	J_{sc} [mA/cm^2]	FF	PCE [%]
1:1	none	0.64	3.10	0.66	1.30
1:2	none	0.64	2.39	0.67	1.01
1:3	none	0.63	2.38	0.67	1.01
1:2	9% CN	0.61	6.09	0.63	2.35
1:2	3% DIO	0.59	5.28	0.57	1.77

Table 5.2: Device parameters for DTTDPP:PC71BM solar cells.

Despite the use of additives to give nanoscale phase morphologies and more intimate mixing of polymer and fullerene domains, the Jsc is still relatively low in these devices. Absorption spectroscopy shows that the extinction coefficient of DTTDPP:PC71BM is comparable to that of P3HT:PCBM (about 5×10^4 cm^{-1}),[210] but with a wider absorption range. External quantum efficiency (EQE) measurements suggest that the relatively low Jsc may be due to low charge generation from photons absorbed in the DTTDPP (Fig. 5.13b). This hypothesis is supported by the observation that at longer wavelengths (650 - 800 nm), where the polymer absorbs more strongly, the EQE is lower than at shorter wavelengths where the fullerene absorbance is stronger. As a result, excitons that are being generated in the polymer have a lower probability of being converted into free charge carriers which is in contrast to the behavior seen for P3HT:PC61BM solar cells, where it has been sug-

gested that less efficient exciton harvesting takes place in PC61BM compared to P3HT, due to the smaller exciton diffusion length in the fullerene phase.[17] The behavior observed for the DTTDPP:PC71BM devices is similar to literature reports for other DPP-based polymers and has been attributed to a morphological effect based on solvent-induced ordering.[210] The cells studied here have higher fill factors and suggest that the origin of this behavior may be due to charge generation rather than charge extraction although further study will be required to determine the detailed mechanism of loss.

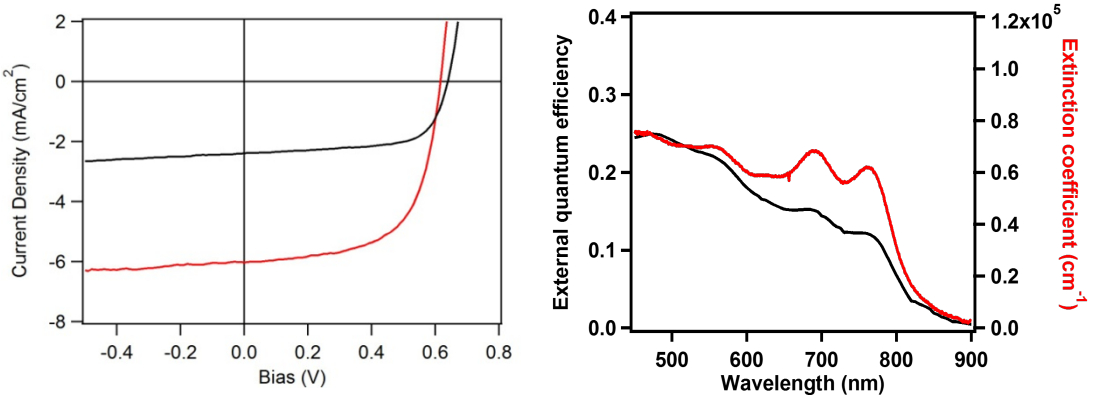

(a) (b)

Figure 5.13: (a) Solar cell J-V curve for DTTDPP:PC71BM (1:2) without additive (black) and with 9 vol.% CN additive (red); (b) EQE (black) and thin film extinction coefficient (red) for DTTDPP:PC71BM (1:2) solar cell device with 9 vol.% CN additive.

Solar cells were also fabricated using DTTBTO for comparison with the DTTDPP systems. In this case, the optimum active layer composition was a 1:3 weight ratio of DTTBTO:PC71BM with cells being processed using 2% vol. of CN as an additive and

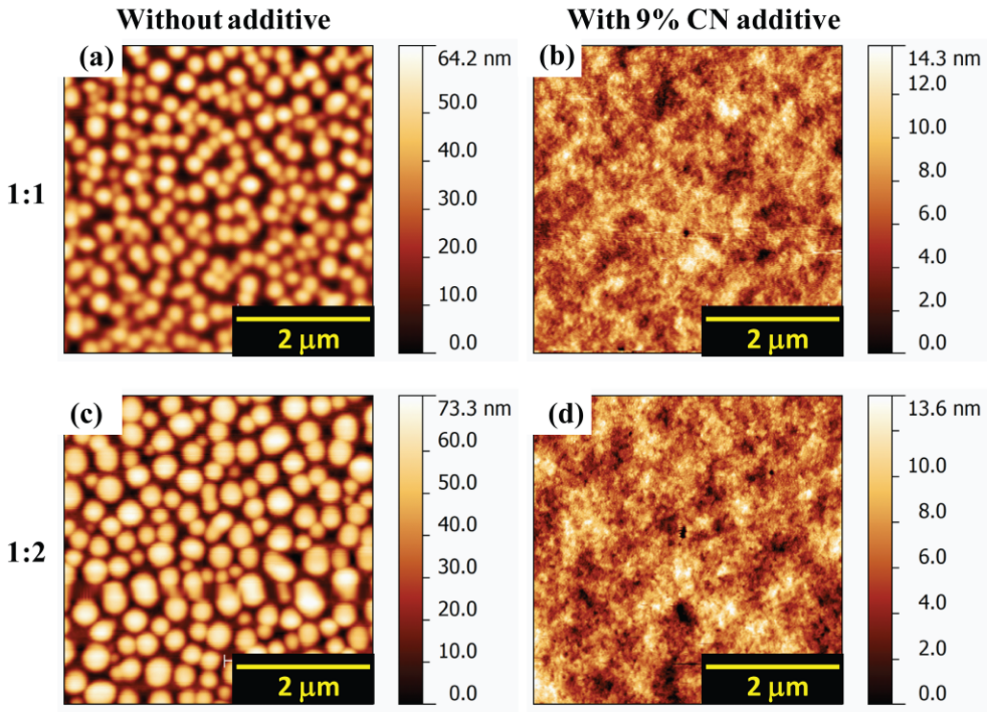

Figure 5.14: AFM topography images of DTTDPP:PC71BM (1:1) composite film(a) spin coated from o-DCB solution; ((b) spin coated from o-DCB solution with 9 vol.% CN additive; AFM topography images of DTTDPP:PC71BM (1:2) composite film (c) spin coated from o-DCB solution; (d) spin coated from o-DCB solution with 9 vol.% CN additive.

LiF/Al as the cathode. This device structure yielded an efficiency of 2.2% with a Voc of 0.72 V, Jsc of 6.59 mA cm^{-2}, and FF of 0.46 (Fig. 5.14a). The ability of the DTTBTO based devices to give an increased Voc when compared to the DTTDPP is in agreement with the deeper values for the HOMO level measured by CV. However, the lower FF

(resulting from inefficient charge extraction) limited the overall device performance relative to DTTDPP. Despite the wider optical gap of DTTBTO than DTTDPP, the short circuit current was still higher in DTTBTO due to a higher extinction coefficient and thus exciton generation in the wavelengths that it absorbs.

DTTBTO:PC71BM	Additive	V_{oc} [V]	J_{sc} [mA/cm^2]	FF	PCE [%]
1:2	none	0.70	3.51	0.37	0.91
1:2	none	0.69	4.11	0.37	1.06
1:3	2% CN	0.72	6.59	0.46	2.18

Table 5.3: Device parameters for DTTBTO:PC71BM solar cells.

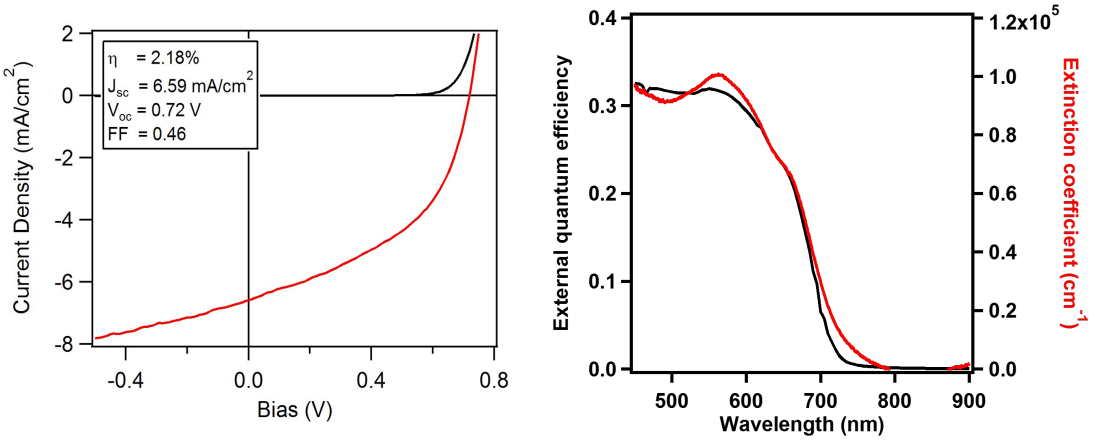

(a) (b)

Figure 5.15: (a) Solar cell J-V curve for DTTBTO:PC71BM (1:3) solar cell device with 2 vol.%CN additive; (b) EQE (black) and thin film extinction coefficient (red) for DTTBTO:PC71BM (1:3) solar cell device with 2 vol.%CN additive.

5.2.3 Conclusions

We have developed a simple and scalable route to synthesize the fused thiophene building block, DTT, which has enabled the preparation of D-π-A-π low-bandgap copolymers with two different acceptors (BTO and DPP). The ability to tailor the structure of these materials permits design rules for these donor-acceptor systems to be demonstrated. The use of thiophene spacers allows DTTDPP to have a broader absorption spectrum (λ_{max} near 800 nm), while DTTBTO has a deeper HOMO energy level yielding a higher Voc. The efficient charge transport and collection in DTTDPP devices suggests that optimiza-

tion of the polymer/fullerene phase separation may lead to further increases in efficiency and to high performance organic solar cells.

5.2.4 Supporting Information

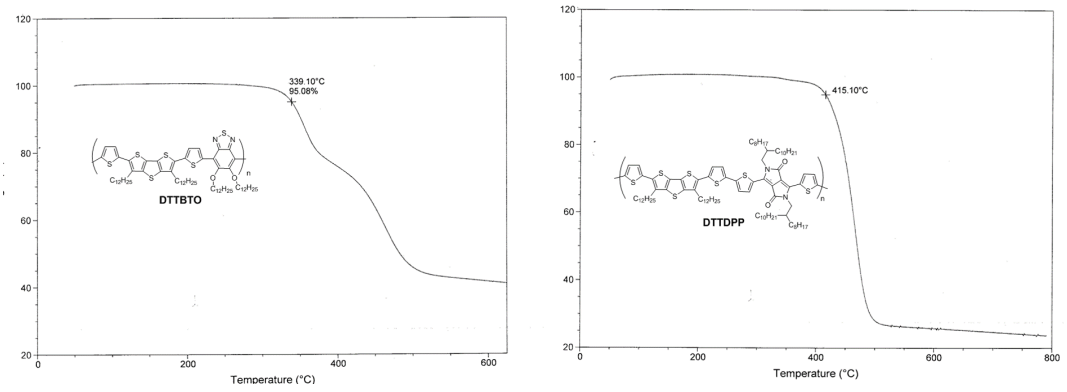

(a) (b)

Figure 5.16: TGA of DTTBTO and DTTDPP.

Cyclic voltammetry was performed in ODCB solutions (1.0mg polymer /1ml ODCB) containing 0.1 M tetra-n-butylammonium perchlorate (0.1M nBu4NClO4) as the supporting electrolyte at a scan rate of 100 mV/s. A glassy carbon electrode and a platinum wire were used as the working and counter electrodes, respectively. All potentials were recorded versus Ag as a reference electrode. The ferrocenium/ferrocene redox couple in ODCB/ nBu4NClO4 occurs at a value of Eo' of +0.42V, with respect to Ag electrode.

Photovoltaic device fabrication and characterization. In a glove box, solutions of DTTDPP:PC71BM or DTTBTO:PC71BM in 1:1, 1:2, and 1:3 ratios in chlorobenzene or

o-dichlorobenzene were prepared, resulting in total concentrations of 20 mg/mL. An additive of between 0-9 vol% chloronapthalene was added to the solutions in o-dichlorobenzene, and an additive of between 0-6 vol% diiodooctane was added to the solutions in chlorobenzene. The solutions were stirred at 80°C before cooling to room temperature. Glass/ITO substrates were sonicated with acetone and isopropanol for 20 minutes each, spin-coated with 40 nm of PEDOT:PSS (Clevios P VP AI 4083), annealed for 20 minutes at 150°C, and transferred to a glove box. The active layer solution was filtered with a 0.45 μm PTFE filter and spin-coated on top of the PEDOT:PSS to form a 90-150 nm layer. On one side of each sample, the active layer and PEDOT:PSS were rubbed off to allow for a bottom contact to the ITO. 25 nm of Ca and 75 nm of Al were thermally evaporated using a mask, creating 5 top contact pixels and a bottom contact to the ITO. The devices were placed in a solar simulator in a glovebox and PCE measurements were taken under 1 sun AM 1.5 light. EQE measurements were taken using a filter wheel. Absorption spectra of the non-metal covered portions of the devices were taken, and film thicknesses were measured using a DEKTAK profilometer.

OTFT device fabrication and characterization. Transistors were fabricated using a top contact, bottom gate geometry. Gold was used for the source-drain contacts and antimony doped silicon was used as the gate contact. An octyltrichlorosiliane (OTS) modified 200 nm thermal oxide silicon substrate was used as the dielectric. The OTS layer was solution deposited by placing the air plasma cleaned substrates in a solution of

20 mL dry toluene and 20 μL OTS for 10 minutes followed by washing in hexane, acetone, and isopropanol. Synthesized polymers were dissolved in a 5 mg/mL solution of dry chlorobenzene:o-dichlorobenzene (1:1 ratio), purchased from Sigma-Aldrich. Solutions were heated to 100°C for 30 mins then filtered with a 13 mm Whatman 0.45 μm PTFE filter. Films were spun under nitrogen from a room temperature solution at 300 rpm/3 s then 1000 rpm/40 s. Film thickness averaged 50 nm, measured using a DEKTAK profilometer. 35 nm of thermally evaporated gold was placed on top through a shadow mask to form the source-drain contacts. Films were annealed under nitrogen on a hot plate calibrated to 150°C for 30 minutes. A back gate was formed by scribing the back of the silicon substrate and applying a small quantity of silver conducting grease to form a conducting pathway to the probe station chuck. Samples were characterized under vacuum, about 10-5 torr, at room temperature; negative voltages were applied to measure polymer hole mobilities for the materials in question. A Lakeshore TTP5 probe station using 2 Kiethley 2400 SMU run under a Lab View routine was used to perform all transistor measurements.

Theoretical calculations. The geometry of model monomers were optimized at the HF/6-31G* level of theory using Spartan (Wavefunction Inc).

Molecular geometry. To gain insights into the electronic structure differences for the DTTBTO and DTTDPP repeat units, molecular geometries were calculated at the HF/6-31G* level. The lowest energy conformation of DTTBTO shows that the BTO acceptor unit rotates out of the plane of the co-planar thiophene units with a dihedral angle of

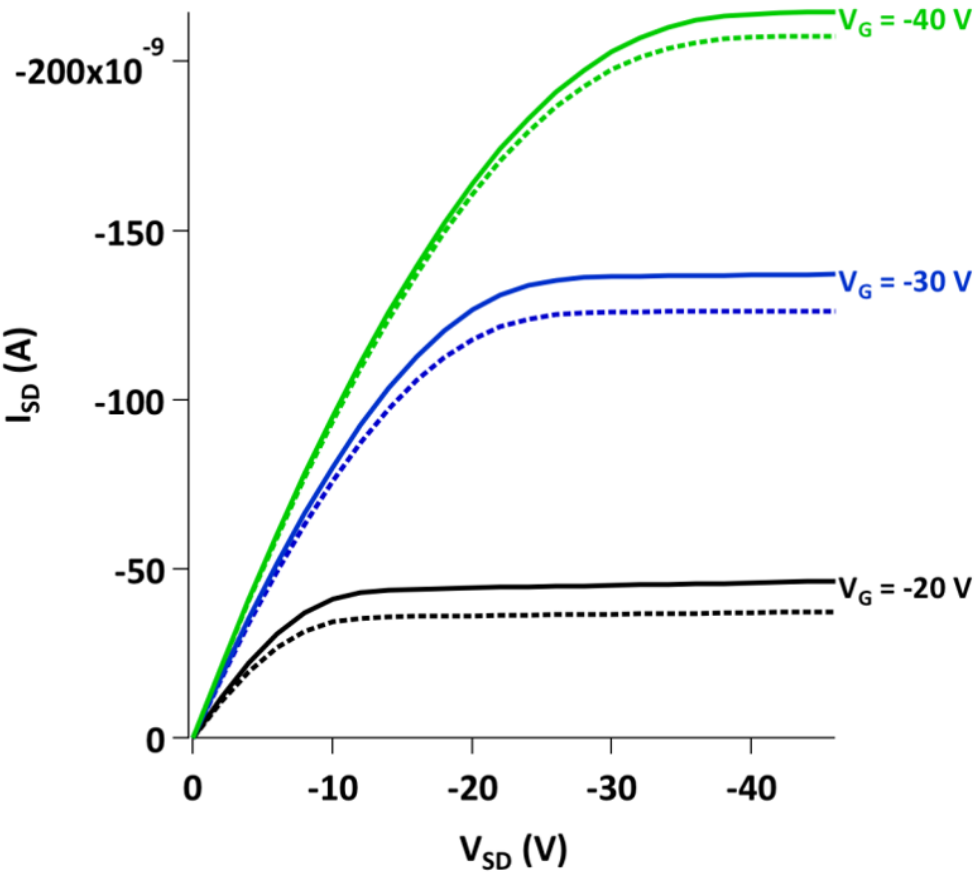

Figure 5.17: Normalized output curves for DTTDPP as cast (dashed lines) and annealed (solid lines) films at VG = -20, -30, -40 V.

35°. In contrast, the DPP unit is rotated by 17° out of the plane of the thiophene units in DTTDPP. The larger dihedral angle between the donor and acceptor in DTTBTO limits π-conjugation along the backbone when compared to the more coplanar DTTDPP. The frontier orbitals reflect these differences showing strong localization of the HOMO on the

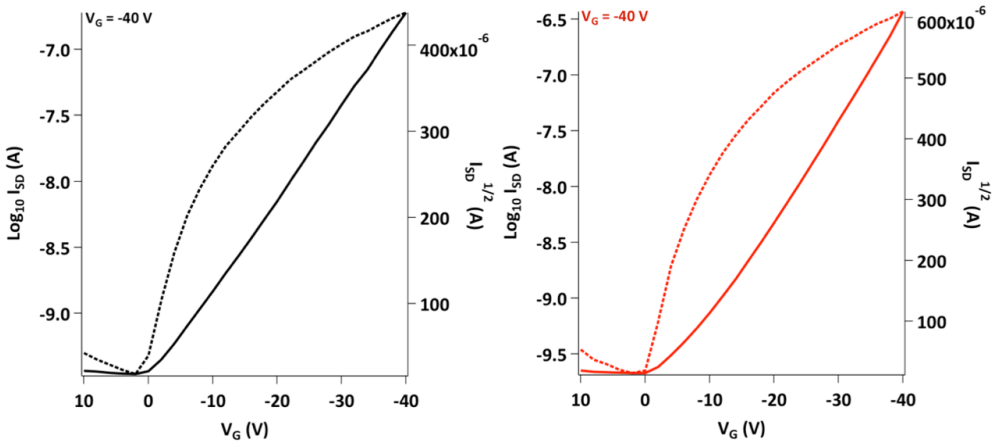

Figure 5.18: Normalized transfer curves for DTTDPP as cast (black lines) and annealed (red lines) films at a VG = -40 V.

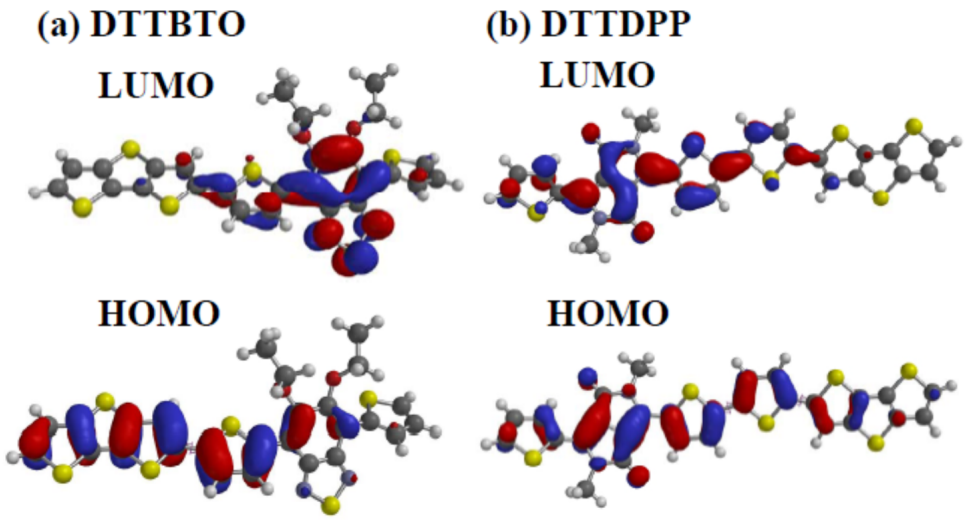

Figure 5.19: The HOMO and LUMO calculation for DTTBTO and DTTDPP polymers.

DTT and the LUMO on BTO for DTTBTO whereas only partial localization is observed for DTTDPP.

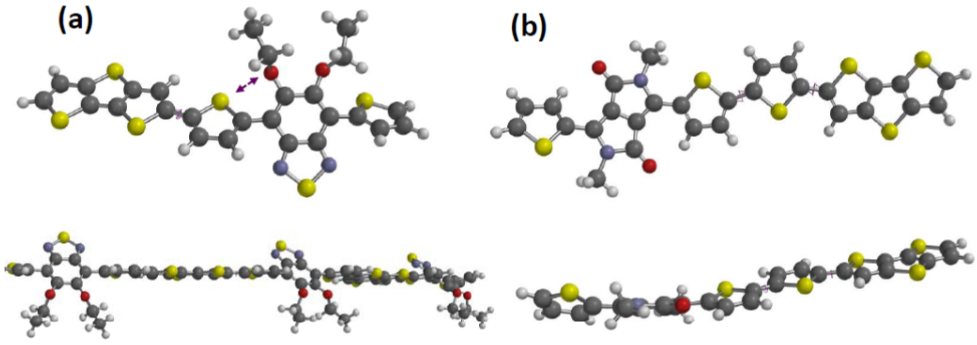

Figure 5.20: Molecular geometry from DFT calculations on (a) DTTBTO and (b) DTTDPP at the HF/6-31G* level.

2-D grazing incidence wide angle X-ray scattering (GIWAXS) experiments were performed on the 11-3 beamline at the Stanford Synchrotron Radiation Lightsource (SSRL) on films of DTTDPP and DTTBTO on top of Si substrates.

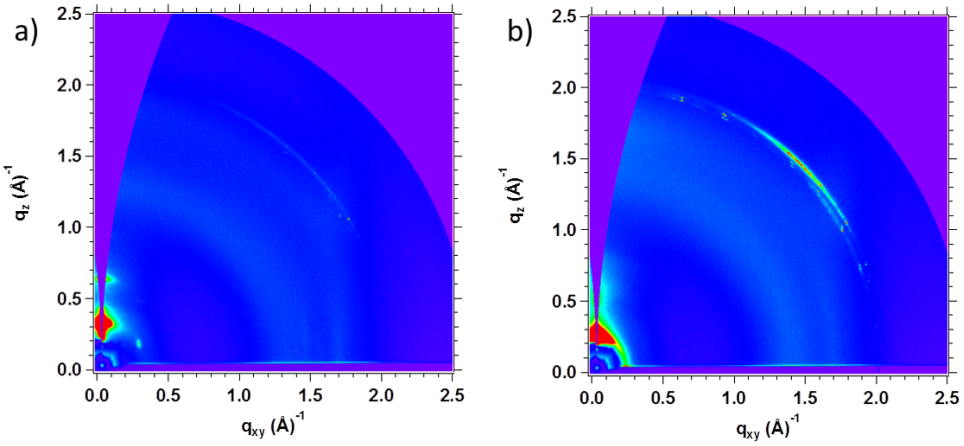

Figure 5.21: (a) 2-D GIWAXS image of DTTDPP; (b) 2-D GIWAXS image of DTTBTO.

DTTDPP:PC71BM	Additive	Electrode	V_{oc} [V]	J_{sc} [mA/cm²]	FF	PCE [%]
1:1	none	Ca/Al	0.64	3.10	0.66	1.30
1:2	none	Ca/Al	0.64	2.39	0.67	1.01
1:3	none	Ca/Al	0.63	2.38	0.67	1.01
1:1	3% DIO	Ca/Al	0.61	4.90	0.51	1.51
1:2	3% DIO	Ca/Al	0.59	5.28	0.57	1.77
1:3	3% DIO	Ca/Al	0.61	3.73	0.53	1.21
1:2	1.5% CN	Ca/Al	0.63	4.18	0.65	1.70
1:2	3% CN	Ca/Al	0.62	5.48	0.63	2.15
1:2	9% CN	Ca/Al	0.61	6.09	0.63	2.35
DTTBTO:PC71BM	Additive	Electrode	V_{oc} [V]	J_{sc} [mA/cm²]	FF	PCE [%]
1:2	none	Ca/Al	0.70	3.51	0.37	0.91
1:3	none	Ca/Al	0.69	4.11	0.37	1.06
1:2	2% CN	Ca/Al	0.71	4.41	0.43	1.24
1:3	2% CN	Ca/Al	0.70	4.86	0.43	1.47
1:2	6% CN	Ca/Al	0.72	4.28	0.40	1.24
1:3	6% CN	Ca/Al	0.72	4.44	0.42	1.34
1:3	2% CN	LiF/Al	0.72	6.59	0.46	2.18

Table 5.4: Device parameters for more conditions of DTTDPP:PC71BM and DTTBTO:PC71BM solar cells.

5.3 Fullerene Derivatives with Low Thermal Conductivity for Thermoelectric Applications

Recently, Duda et al.[211] reported that the fullerene derivative [6,6]-phenyl-C61-butyric acid methyl ester (PCBM) has the lowest thermal conductivity Λ ever observed in a fully dense solid, $\Lambda \approx 0.03$ W m^{-1} K^{-1}. We prepared a variety of phases and microstructures of PCBM and the closely related compound [6,6]-phenyl-C61-butyric acid n-butyl ester (PCBNB) and found that the thermal conductivities of PCBM and PCBNB films are mostly limited to the range $0.05 < \Lambda < 0.06$ W m^{-1} K^{-1} with a few samples having slightly higher Λ. The conductivities we observe are ≈ 70% larger than reported by Duda et al. but are still "ultralow" in the sense that the thermal conductivity is a factor of ≈ 3 below the conductivity predicted by the minimum thermal conductivity model using an estimate of the thermally excited modes per molecule.

PCBNB was used as received from Solenne. PCBNB was dissolved in chlorobenzene at concentrations of 16 mg/mL and 20 mg/mL and stirred at 90°C for more than 3 hours in a N2 environment. Silicon substrates were washed sequentially with acetone, 2 wt.% soap:DI water solution, DI water, and isopropanol in an ultrasonic bath for 5 minutes respectively. PEDOT:PSS (Clevios P VP AI 4083 as received from Heraeus) was brought to room temperature, and filtered through a 0.45 μm PVDF filter onto some of the clean Si substrates. Spin coating was performed at 4000 rpm for 45 seconds, producing films

35 nm thick. The samples were annealed on a hot plate at 150°C for 20 minutes, and transferred into a N2 glovebox. The PCBNB solutions were cooled to room temperature and passed through a 0.45 μm PTFE filter onto the substrates. The 16 mg/mL solution was spin coated on the substrates at rates of 700 or 1000 rpm for 60 seconds in the first step and 2000 rpm for 5 seconds in the second step, producing films 50-100 nm thick as measured by profilometry. The 20 mg/mL solution was spin coated on the clean substrates at a rate of 600 rpm for 60 seconds in the first step and 2000 rpm for 5 seconds in the second step, producing films 110 nm thick as measured by profilometry. Some films were annealed on a hot plate at temperatures ranging from 80-180 °C for 30 minutes.

Xiaojia Wang in Prof. David Cahill's group at UIUC used time-domain thermoreflectance (TDTR) to study the thermal conductivity of thin films of C60, PCBM, and PCBNB. The fabrication conditions, substrate types, sample thicknesses, and polymorphs do not have significant impacts on the thermal conductivities of PCBM and PCBNB. This class of samples made from fullerene derivatives have ultralow thermal conductivities close to the lowest value of fully dense solids.

Chapter 6

Conclusion

In this work, we have discussed the relationships between morphology and charge transfer states in organic solar cells. We focused on studying a small molecule system composed of BP donor and PCBNB acceptor, which, in contrast to most BHJ solar cells, has only pure domains. We first characterized the crystal structures and textures of the polymorphs of BP and PCBNB. Changes in the unit cell, π-π stacking, crystallite orientation and size, and blend morphology can lead to differences in charge transport and device performance. Pure films of both materials exhibit multiple polymorphs at room temperature depending on annealing temperature and time. In-situ 2-D GIWAXS was used to rapidly examine the two polymorphs of BP which have drastically different degrees of texture. In PCBNB, electron microscopy shows that the crystal structures of the two crystalline polymorphs are based on the same simple hexagonal lattice, but one polymorph exhibits a superlattice consisting of a regular deficiency of fullerene molecules. In the future, studying the phase transformations of these materials with greater time

resolution, for example using in-situ GIWAXS measurement setups where diffraction patterns are collected more rapidly, can provide greater insight into the kinetics of the transformations.

We then described a method of using a thermally degradable binder polymer, poly(propylene carbonate), to control the interfacial morphology of solar cells composed of BP and PCBNB without mixing them in a blend layer. This was possible due to the property of BP that it is insoluble while its precursor is soluble, enabling the sequential deposition of layers. When the BP precursor layer is annealed, it transforms into BP while the binder polymer decomposes into gaseous products, leaving fixed gaps in the film which are then filled with PCBNB. Therefore, unlike the morphology of a blend layer, the interfacial morphology is independent of the choice of acceptor, allowing for the possibility of optimizing the morphology and the choice of acceptor independently. Using different acceptors with this method would be a promising avenue for future exploration. Furthermore, the increased viscosity of the solution containing BP precursor and binder polymer increases its large area fabrication processability.

Going back to the blend morphology of BP and PCBNB, we varied the donor-acceptor ratio and annealing temperature of the blend film and obtained morphologies ranging from mostly flat to column-like features of BP and PCBNB. The charge transfer state density, which is proportional to the donor-acceptor interfacial area, was examined non-destructively using sub-bandgap external quantum efficiency measurements. By combin-

ing these measurements with AFM topography and a simulation of Förster resonance energy transfer, we were able to gain valuable insights about the photophysics in this system, including the oscillator strength of CT states and the exciton binding energy. Future electroluminescence measurements would enhance the analysis of CT states, and it would be interesting to apply our methods to other materials systems with either pure domains, or both pure and mixed domains.

Finally, we showed that many of the insights and techniques used to study the BP:PCBNB system are also useful in studying other systems of organic or solution-procesed semiconductors. We optimized the morphology and performance of OPVs made with novel low-bandgap donor-acceptor copolymers. We then found that ionic photoconductivity plays an important role in the behavior of photodetectors made with solution processed amorphous ZnO and their interaction with organic semiconductors. It is hoped that these and further advances in the characterization of organic semiconductors will allow for increased understanding and commercialization of these materials.

Bibliography

(1) U.S. Department of Energy, *2010 Solar Technologies Market Report*, tech. rep. November, 2010 (see p. 1).

(2) S. Günes, H. Neugebauer, and N. S. Sariciftci, "Conjugated polymer-based organic solar cells." *Chem. Rev.*, 2007, **107**, 1324–38 (see pp. 2, 166).

(3) H. Hoppe and N. S. Sariciftci, "Organic solar cells: An overview", *J. Mater. Res.*, 2004, **19**, 1924–1945 (see p. 2).

(4) Y.-W. Su, S.-C. Lan, and K.-H. Wei, "Organic photovoltaics", *Mater. Today*, 2012, **15**, 554–562 (see p. 2).

(5) National Renewable Energy Laboratory, *Research Cell Efficiency Records*, 2014 (see p. 3).

(6) X.-Y. Zhu, Q. Yang, and M. Muntwiler, "Charge-transfer excitons at organic semiconductor surfaces and interfaces", *Acc. Chem. Res.*, 2009, **42**, 1779–87 (see p. 4).

(7) J.-L. Brédas, D. Beljonne, V. Coropceanu, and J. Cornil, "Charge-transfer and energy-transfer processes in pi-conjugated oligomers and polymers: a molecular picture." *Chem. Rev.*, 2004, **104**, 4971–5004 (see p. 5).

(8) Y. Lin, Y. Li, and X. Zhan, "Small molecule semiconductors for high-efficiency organic photovoltaics." *Chem. Soc. Rev.*, 2012, **41**, 4245–72 (see p. 6).

(9) G. Chamberlain, "Organic solar cells: A review", *Sol. Cells*, 1983, **8**, 47–83 (see p. 6).

(10) C. W. Tang, "Two-layer organic photovoltaic cell", *Appl. Phys. Lett.*, 1986, **48**, 183 (see pp. 6, 21).

(11) Z. He, C. Zhong, S. Su, M. Xu, H. Wu, and Y. Cao, "Enhanced power-conversion efficiency in polymer solar cells using an inverted device structure", *Nat. Photonics*, 2012, 1–5 (see p. 7).

(12) Y. Sun, G. C. Welch, W. L. Leong, C. J. Takacs, G. C. Bazan, and A. J. Heeger, "Solution-processed small-molecule solar cells with 6.7% efficiency", *Nat. Mater.*, 2011, **11**, 44–48 (see pp. 7, 20).

(13) J. Roncali, "Molecular Bulk Heterojunctions: An Emerging Approach to Organic Solar Cells", *Acc. Chem. Res.*, 2009, **42**, 1719–1730 (see pp. 7, 20, 75).

(14) P. W. M. Blom, V. D. Mihailetchi, L. J. A. Koster, and D. E. Markov, "Device Physics of Polymer:Fullerene Bulk Heterojunction Solar Cells", *Adv. Mater.*, 2007, **19**, 1551–1566 (see p. 9).

(15) L. A. A. Pettersson, L. S. Roman, and O. Inganäs, "Modeling photocurrent action spectra of photovoltaic devices based on organic thin films", *J. Appl. Phys.*, 1999, **86**, 487 (see pp. 10, 12).

(16) P. Peumans, A. Yakimov, and S. R. Forrest, "Small molecular weight organic thin-film photodetectors and solar cells", *J. Appl. Phys.*, 2003, **93**, 3693 (see pp. 10, 12).

(17) G. F. Burkhard, E. T. Hoke, S. R. Scully, and M. D. McGehee, "Incomplete Exciton Harvesting from Fullerenes in Bulk Heterojunction Solar Cells", *Nano Lett.*, 2009, **9**, 4037–4041 (see pp. 10, 177).

(18) D. Veldman, S. C. J. Meskers, and R. A. J. Janssen, "The Energy of Charge-Transfer States in Electron Donor-Acceptor Blends: Insight into the Energy Losses in Organic Solar Cells", *Adv. Funct. Mater.*, 2009, **19**, 1939–1948 (see pp. 10, 172).

(19) M. Muntwiler, Q. Yang, W. Tisdale, and X.-Y. Zhu, "Coulomb Barrier for Charge Separation at an Organic Semiconductor Interface", *Phys. Rev. Lett.*, 2008, **101**, 1–4 (see p. 11).

(20) J. Lee, K. Vandewal, S. R. Yost, M. E. Bahlke, L. Goris, M. A. Baldo, J. V. Manca, and T. V. Voorhis, "Charge Transfer State Versus Hot Exciton Dissociation in Polymer-Fullerene Blended Solar Cells", *J. Am. Chem. Soc.*, 2010, **132**, 11878–11880 (see p. 11).

(21) S. Park, A. Roy, S. Beaupré, S. Cho, N. Coates, J. S. Moon, D. Moses, M. Leclerc, K. Lee, and A. J. Heeger, "Bulk heterojunction solar cells with internal quantum efficiency approaching 100%", *Nat. Photonics*, 2009, **3**, 297–302 (see p. 11).

(22) G. F. Burkhard, E. T. Hoke, and M. D. McGehee, "Accounting for Interference, Scattering, and Electrode Absorption to Make Accurate Internal Quantum Efficiency Measurements in Organic and Other Thin Solar Cells", *Adv. Mater.*, 2010, **22**, 3293–3297 (see pp. 12, 106, 119).

(23) S. J. Byrnes, *tmm*, 2012 (see pp. 12, 107, 144).

(24) D. S. Germack, C. K. Chan, R. J. Kline, D. A. Fischer, D. J. Gundlach, M. F. Toney, L. J. Richter, and D. M. DeLongchamp, "Interfacial Segregation in Polymer/Fullerene Blend Films for Photovoltaic Devices", *Macromolecules*, 2010, **43**, 3828–3836 (see p. 13).

(25) K. N. Winzenberg, P. Kemppinen, G. Fanchini, M. Bown, G. E. Collis, C. M. Forsyth, K. Hegedus, T. B. Singh, and S. E. Watkins, "Dibenzo[b , def]chrysene Derivatives: Solution-Processable Small Molecules that Deliver High Power-Conversion Efficiencies in Bulk Heterojunction Solar Cells", *Chem. Mater.*, 2009, **21**, 5701–5703 (see p. 20).

(26) S. Loser, C. J. Bruns, H. Miyauchi, R. P. Ortiz, A. Facchetti, S. I. Stupp, and T. J. Marks, "A naphthodithiophene-diketopyrrolopyrrole donor molecule for efficient solution-processed solar cells." *J. Am. Chem. Soc.*, 2011, **133**, 8142–5 (see p. 20).

(27) J. E. Anthony, "Functionalized acenes and heteroacenes for organic electronics." *Chem. Rev.*, 2006, **106**, 5028–48 (see p. 20).

(28) H. Minemawari, T. Yamada, H. Matsui, J. Tsutsumi, S. Haas, R. Chiba, R. Kumai, and T. Hasegawa, "Inkjet printing of single-crystal films." *Nature*, 2011, **475**, 364–7 (see p. 20).

(29) J. Smith, W. Zhang, R. Sougrat, K. Zhao, R. Li, D. Cha, A. Amassian, M. Heeney, I. McCulloch, and T. D. Anthopoulos, "Solution-processed small molecule-polymer blend organic thin-film transistors with hole mobility greater than 5 cm2/Vs." *Adv. Mater.*, 2012, **24**, 2441–6 (see p. 20).

(30) M. A. Green, K. Emery, Y. Hishikawa, W. Warta, and E. D. Dunlop, "Solar cell efficiency tables (version 39)", *Prog. Photovoltaics Res. Appl.*, 2012, **20**, 12–20 (see p. 20).

(31) J. Rivnay, L. H. Jimison, J. E. Northrup, M. F. Toney, R. Noriega, S. Lu, T. J. Marks, A. Facchetti, and A. Salleo, "Large modulation of carrier transport by grain-boundary molecular packing and microstructure in organic thin films." *Nat. Mater.*, 2009, **8**, 952–8 (see pp. 21, 48).

(32) M. G. Walter, A. B. Rudine, and C. C. Wamser, "Porphyrins and phthalocyanines in solar photovoltaic cells", *J. Porphyr. Phthalocyanines*, 2010, **14**, 759 (see p. 21).

(33) J. Xue, B. P. Rand, S. Uchida, and S. R. Forrest, "A Hybrid Planar-Mixed Molecular Heterojunction Photovoltaic Cell", *Adv. Mater.*, 2005, **17**, 66–71 (see pp. 21, 24, 102).

(34) W. Campbell, K. Jolley, P. Wagner, K. Wagner, P. Walsh, K. Gordon, L. Schmidt-Mende, M. Nazeeruddin, Q. Wang, M. Grätzel, and D. Officer, "Highly Efficient Porphyrin Sensitizers for Dye-Sensitized Solar Cells", *J. Phys. Chem. C*, 2007, **111**, 11760–11762 (see pp. 21, 29, 30).

(35) M. K. R. Fischer, I. López-Duarte, M. M. Wienk, M. V. Martínez-Díaz, R. A. J. Janssen, P. Bäuerle, and T. Torres, "Functionalized dendritic oligothiophenes: ruthenium phthalocyanine complexes and their application in bulk heterojunction solar cells." *J. Am. Chem. Soc.*, 2009, **131**, 8669–76 (see p. 21).

(36) H. Yamada, T. Okujima, and N. Ono, "Organic semiconductors based on small molecules with thermally or photochemically removable groups." *Chem. Commun.*, 2008, 2957–74 (see pp. 21, 48).

(37) A. Afzali, C. D. Dimitrakopoulos, and T. L. Breen, "High-Performance, Solution-Processed Organic Thin Film Transistors from a Novel Pentacene Precursor", *J. Am. Chem. Soc.*, 2002, **124**, 8812–8813 (see p. 21).

(38) H. Uno, Y. Yamashita, M. Kikuchi, H. Watanabe, H. Yamada, T. Okujima, T. Ogawa, and N. Ono, "Photo precursor for pentacene", *Tetrahedron Lett.*, 2005, **46**, 1981–1983 (see p. 21).

(39) A. R. Murphy, J. M. J. Fréchet, P. Chang, J. Lee, and V. Subramanian, "Organic thin film transistors from a soluble oligothiophene derivative containing thermally removable solubilizing groups." *J. Am. Chem. Soc.*, 2004, **126**, 1596–1597 (see p. 21).

(40) S. Ito, T. Murashima, N. Ono, and H. Uno, "A new synthesis of benzoporphyrins using 4,7-dihydro-4,7-ethano-2H-isoindole as a synthon of isoindole", *Chem. Commun.*, 1998, 1661–1662 (see p. 21).

(41) S. Ito, N. Ochi, T. Murashima, N. Ono, and H. Uno, "A new synthesis of [2,3]naphthoporphyrins", *Chem. Commun.*, 2000, 893–894 (see p. 21).

(42) Y. Shimizu, Z. Shen, T. Okujima, H. Uno, and N. Ono, "First synthesis of a series of core-modified tetrabenzoporphyrins." *Chem. Commun.*, 2004, 374–5 (see p. 21).

(43) Y. Inokuma, N. Ono, H. Uno, D. Y. Kim, S. B. Noh, D. Kim, and A. Osuka, "Enlarged pi-electronic network of a meso-meso, beta-beta, beta-beta triply linked dibenzoporphyrin dimer that exhibits a large two-photon absorption cross section." *Chem. Commun.*, 2005, 3782–4 (see p. 21).

(44) H. Yamada, K. Kushibe, T. Okujima, H. Uno, and N. Ono, "Novel one-pot synthesis of 5-alkenyl-15-alkynylporphyrins and their derivatisation to a butadiyne-linked benzoporphyrin dimer", *Chem. Commun.*, 2006, 383 (see p. 21).

(45) T. Okujima, Y. Hashimoto, G. Jin, H. Yamada, H. Uno, and N. Ono, "Synthesis of extremely soluble precursors of tetrabenzoporphyrins", *Tetrahedron*, 2008, **64**, 2405–2411 (see p. 21).

(46) P. B. Shea, J. Kanicki, L. R. Pattison, P. Petroff, M. Kawano, H. Yamada, and N. Ono, "Solution-processed nickel tetrabenzoporphyrin thin-film transistors", *J. Appl. Phys.*, 2006, **100**, 034502 (see p. 21).

(47) P. B. Shea, L. R. Pattison, M. Kawano, C. Chen, J. Chen, P. Petroff, D. C. Martin, H. Yamada, N. Ono, and J. Kanicki, "Solution-processed polycrystalline copper tetrabenzoporphyrin thin-film transistors", *Synth. Met.*, 2007, **157**, 190–197 (see p. 21).

(48) P. B. Shea, H. Yamada, N. Ono, and J. Kanicki, "Solution-processed zinc tetrabenzoporphyrin thin-films and transistors", *Thin Solid Films*, 2012, DOI: 10.1016/j.tsf.2012.01.034 (see p. 21).

(49) S. Aramaki and J. Mizuguchi, "29H,31H-Tetrabenzo[b,g,l,q]porphin", *Acta Crystallogr. Sect. E Struct. Reports Online*, 2003, **59**, 1556–1558 (see pp. 22, 25, 33, 80, 102, 126).

(50) S. Aramaki, Y. Sakai, and N. Ono, "Solution-processible organic semiconductor for transistor applications: Tetrabenzoporphyrin", *Appl. Phys. Lett.*, 2004, **84**, 2085–2087 (see pp. 22, 24, 25, 102).

(51) W. Chen, M. P. Nikiforov, and S. B. Darling, "Morphology characterization in organic and hybrid solar cells", *Energy Environ. Sci.*, 2012, **5**, 8045 (see p. 22).

(52) A. Mayer, A. Kazimirov, and G. Malliaras, "Dynamics of Bimodal Growth in Pentacene Thin Films", *Phys. Rev. Lett.*, 2006, **97**, 105503 (see p. 22).

(53) A. Mayer, R. Ruiz, H. Zhou, R. Headrick, A. Kazimirov, and G. Malliaras, "Growth dynamics of pentacene thin films: Real-time synchrotron x-ray scattering study", *Phys. Rev. B*, 2006, **73**, 205307 (see p. 22).

(54) S. Hong, A. Amassian, A. R. Woll, S. Bhargava, J. D. Ferguson, G. G. Malliaras, J. D. Brock, and J. R. Engstrom, "Real time monitoring of pentacene growth on SiO2 from a supersonic source", *Appl. Phys. Lett.*, 2008, **92**, 253304 (see p. 22).

(55) A. Amassian, V. A. Pozdin, T. V. Desai, S. Hong, A. R. Woll, J. D. Ferguson, J. D. Brock, G. G. Malliaras, and J. R. Engstrom, "Post-deposition reorganization of pentacene films deposited on low-energy surfaces", *J. Mater. Chem.*, 2009, **19**, 5580 (see p. 22).

(56) D. G. de Oteyza, E. Barrena, J. O. Ossó, S. Sellner, and H. Dosch, "Thickness-dependent structural transitions in fluorinated copper-phthalocyanine (F16CuPc) films." *J. Am. Chem. Soc.*, 2006, **128**, 15052–3 (see p. 22).

(57) T. N. Krauss, E. Barrena, T. Lohmüller, J. P. Spatz, and H. Dosch, "Growth mechanisms of phthalocyanine nanowires induced by Au nanoparticle templates." *Phys. Chem. Chem. Phys.*, 2011, **13**, 5940–4 (see p. 22).

(58) S. Kowarik, a. Gerlach, S. Sellner, F. Schreiber, L. Cavalcanti, and O. Konovalov, "Real-Time Observation of Structural and Orientational Transitions during Growth of Organic Thin Films", *Phys. Rev. Lett.*, 2006, **96**, 125504 (see p. 22).

(59) Y. Zhang, E. Barrena, X. Zhang, A. Turak, F. Maye, and H. Dosch, "New Insight into the Role of the Interfacial Molecular Structure on Growth and Scaling in Organic Heterostructures", *J. Phys. Chem. C*, 2010, **114**, 13752–13758 (see p. 22).

(60) P. Fenter, F. Schreiber, L. Zhou, P. Eisenberger, and S. Forrest, "In situ studies of morphology, strain, and growth modes of a molecular organic thin film", *Phys. Rev. B*, 1997, **56**, 3046–3053 (see p. 22).

(61) B. Krause, F. Schreiber, H. Dosch, a. Pimpinelli, and O. H. Seeck, "Temperature dependence of the 2D-3D transition in the growth of PTCDA on Ag(111): A real-time X-ray and kinetic Monte Carlo study", *Europhys. Lett.*, 2004, **65**, 372–378 (see p. 22).

(62) D. W. Breiby, F. Hansteen, W. Pisula, O. Bunk, U. Kolb, J. W. Andreasen, K. Müllen, and M. M. Nielsen, "In situ studies of phase transitions in thin discotic films." *J. Phys. Chem. B*, 2005, **109**, 22319–25 (see p. 22).

(63) R. Li, H. U. Khan, M. M. Payne, D.-M. Smilgies, J. E. Anthony, and A. Amassian, "Heterogeneous Nucleation Promotes Carrier Transport in Solution-Processed Organic Field-Effect Transistors", *Adv. Funct. Mater.*, 2013, **23**, 291–297 (see p. 23).

(64) D.-M. Smilgies, R. Li, G. Giri, K. W. Chou, Y. Diao, Z. Bao, and A. Amassian, "Look fast: Crystallization of conjugated molecules during solution shearing probed in-situ and in real time by X-ray scattering", *Phys. Status Solidi Rapid Res. Lett.*, 2013, **7**, 177–179 (see pp. 23, 46).

(65) M. Sanyal, B. Schmidt-Hansberg, M. F. Klein, C. Munuera, A. Vorobiev, A. Colsmann, P. Scharfer, U. Lemmer, W. Schabel, H. Dosch, and E. Barrena, "Effect of Photovoltaic Polymer/Fullerene Blend Composition Ratio on Microstructure Evolution during Film Solidification Investigated in Real Time by X-ray Diffraction", *Macromolecules*, 2011, **44**, 3795–3800 (see p. 23).

(66) J. T. Rogers, K. Schmidt, M. F. Toney, G. C. Bazan, and E. J. Kramer, "Time-resolved structural evolution of additive-processed bulk heterojunction solar cells." *J. Am. Chem. Soc.*, 2012, **134**, 2884–7 (see p. 23).

(67) E. Verploegen, R. Mondal, C. J. Bettinger, S. Sok, M. F. Toney, and Z. Bao, "Effects of Thermal Annealing Upon the Morphology of Polymer-Fullerene Blends", *Adv. Funct. Mater.*, 2010, **20**, 3519–3529 (see pp. 23, 64, 65).

(68) S. Lilliu, T. Agostinelli, E. Pires, M. Hampton, J. Nelson, and J. E. Macdonald, "Dynamics of Crystallization and Disorder during Annealing of P3HT/PCBM Bulk Heterojunctions", *Macromolecules*, 2011, **44**, 2725–2734 (see pp. 23, 38, 64).

(69) N. D. Treat, M. A. Brady, G. Smith, M. F. Toney, E. J. Kramer, C. J. Hawker, and M. L. Chabinyc, "Interdiffusion of PCBM and P3HT Reveals Miscibility in a Photovoltaically Active Blend", *Adv. Energy Mater.*, 2011, **1**, 82–89 (see p. 23).

(70) Y. Matsuo, Y. Sato, T. Niinomi, I. Soga, H. Tanaka, and E. Nakamura, "Columnar Structure in Bulk Heterojunction in Solution-Processable Three-Layered p-i-n Organic Photovoltaic Devices Using Tetrabenzoporphyrin Precursor and Silylmethyl[60]fullerene", *J. Am. Chem. Soc.*, 2009, **131**, 16048–16050 (see pp. 23, 75, 79, 102, 107).

(71) N. Noguchi, S. Junwei, H. Asatani, and M. Matsuoka, "Control of Morphology and Orientation of a Thin Film Tetrabenzoporphyrin (TBP) Organic Semiconductor by Solid-State Crystallization", *Cryst. Growth Des.*, 2010, **10**, 1848–1853 (see pp. 24, 36, 102).

(72) Y. Sato, T. Niinomi, M. Hashiguchi, Y. Matsuo, and E. Nakamura, Proc. SPIE, ed. Z. H. Kafafi and P. A. Lane, SPIE, San Diego, CA, USA, 2007, vol. 6656, pages (see pp. 24, 25, 27, 66, 75).

(73) M. Guide, X.-D. Dang, and T.-Q. Nguyen, "Nanoscale characterization of tetrabenzoporphyrin and fullerene-based solar cells by photoconductive atomic force microscopy." *Adv. Mater.*, 2011, **23**, 2313–9 (see pp. 24, 66).

(74) S.-Y. Ku, C. D. Liman, J. E. Cochran, M. F. Toney, M. L. Chabinyc, and C. J. Hawker, "Solution-processed nanostructured benzoporphyrin with polycarbonate binder for photovoltaics", *Adv. Mater.*, 2011, **23**, 2289–2293 (see pp. 24, 66, 102).

(75) Y. Sato, T. Niinomi, Y. Abe, Y. Matsuo, and E. Nakamura, Proc. SPIE, ed. Z. H. Kafafi and P. A. Lane, SPIE, San Diego, CA, USA, 2008, vol. 7052, pages (see pp. 25, 66, 75, 125).

(76) Z. D. Popovic, "A study of carrier generation mechanism in x-metal-free phthalocyanine", *J. Chem. Phys.*, 1983, **78**, 1552 (see p. 25).

(77) D. Placencia, W. Wang, J. Gantz, J. L. Jenkins, and N. R. Armstrong, "Highly Photoactive Titanyl Phthalocyanine Polymorphs as Textured Donor Layers in Organic Solar Cells", *J. Phys. Chem. C*, 2011, **115**, 18873–18884 (see p. 25).

(78) D.-M. Smilgies, "Geometry-independent intensity correction factors for grazing-incidence diffraction", *Rev. Sci. Instrum.*, 2002, **73**, 1706 (see p. 28).

(79) J. L. Baker, L. H. Jimison, S. C. B. Mannsfeld, S. Volkman, S. Yin, V. Subramanian, A. Salleo, A. P. Alivisatos, and M. F. Toney, "Quantification of Thin Film Crystallographic Orientation Using X-ray Diffraction with an Area Detector", *Langmuir*, 2010, **26**, 9146–9151 (see pp. 28, 50).

(80) S. C. B. Mannsfeld, M. L. Tang, and Z. Bao, "Thin film structure of triisopropylsilylethynyl-functionalized pentacene and tetraceno[2,3-b]thiophene from grazing incidence X-ray diffraction." *Adv. Mater.*, 2011, **23**, 127–131 (see p. 28).

(81) A. Boultif and D. Louër, "Indexing of powder diffraction patterns for low-symmetry lattices by the successive dichotomy method", *J. Appl. Crystallogr.*, 1991, **24**, 987–993 (see pp. 28, 34).

(82) D. W. Breiby, O. Bunk, J. W. Andreasen, H. T. Lemke, and M. M. Nielsen, "Simulating X-ray diffraction of textured films", *J. Appl. Crystallogr.*, 2008, **41**, 262–271 (see pp. 28, 33).

(83) C. C. Mattheus, A. B. Dros, J. Baas, G. T. Oostergetel, A. Meetsma, J. L. de Boer, and T. T. Palstra, "Identification of polymorphs of pentacene", *Synth. Met.*, 2003, **138**, 475–481 (see p. 33).

(84) G. Giri, E. Verploegen, S. C. B. Mannsfeld, S. Atahan-Evrenk, D. H. Kim, S. Y. Lee, H. A. Becerril, A. Aspuru-Guzik, M. F. Toney, and Z. Bao, "Tuning charge transport in solution-sheared organic semiconductors using lattice strain." *Nature*, 2011, **480**, 504–8 (see p. 33).

(85) E. Warren, *X-Ray Diffraction*, Addison-Wesley, Reading, MA, 1969 (see pp. 37, 38).

(86) D.-M. Smilgies, "Scherrer grain-size analysis adapted to grazing-incidence scattering with area detectors." *J. Appl. Crystallogr.*, 2009, **42**, 1030–1034 (see p. 37).

(87) L. H. Jimison, A. Salleo, M. L. Chabinyc, D. Bernstein, and M. F. Toney, "Correlating the microstructure of thin films of poly[5,5-bis(3-dodecyl-2-thienyl)-2,2-bithiophene] with charge transport: Effect of dielectric surface energy and thermal annealing", *Phys. Rev. B*, 2008, **78**, 1–18 (see p. 38).

(88) P. Scardi, M. Leoni, and R. Delhez, "Line broadening analysis using integral breadth methods: a critical review", *J. Appl. Crystallogr.*, 2004, **37**, 381–390 (see p. 38).

(89) K. Momma and F. Izumi, "VESTA 3 for three-dimensional visualization of crystal, volumetric and morphology data", *J. Appl. Crystallogr.*, 2011, **44**, 1272–1276 (see p. 41).

(90) D. Singhal and W. Curatolo, "Drug polymorphism and dosage form design: a practical perspective." *Adv. Drug Deliv. Rev.*, 2004, **56**, 335–47 (see p. 48).

(91) J. T. Rogers, K. Schmidt, M. F. Toney, E. J. Kramer, and G. C. Bazan, "Structural order in bulk heterojunction films prepared with solvent additives." *Adv. Mater.*, 2011, **23**, 2284–8 (see pp. 49, 64).

(92) D. M. DeLongchamp, B. D. Vogt, C. M. Brooks, K. Kano, J. Obrzut, C. A. Richter, O. A. Kirillov, and E. K. Lin, "Influence of a water rinse on the structure and properties of poly(3,4-ethylene dioxythiophene):poly(styrene sulfonate) films." *Langmuir*, 2005, **21**, 11480–3 (see p. 49).

(93) J. D. Myers and J. Xue, "Organic Semiconductors and their Applications in Photovoltaic Devices", *Polym. Rev.*, 2012, **52**, 1–37 (see p. 64).

(94) C. Deibel and V. Dyakonov, "Polymer-fullerene bulk heterojunction solar cells", *Reports Prog. Phys.*, 2010, **73**, 096401 (see p. 64).

(95) J. E. Slota, X. He, and W. T. Huck, "Controlling nanoscale morphology in polymer photovoltaic devices", *Nano Today*, 2010, **5**, 231–242 (see p. 64).

(96) J. Weickert, R. B. Dunbar, H. C. Hesse, W. Wiedemann, and L. Schmidt-Mende, "Nanostructured organic and hybrid solar cells." *Adv. Mater.*, 2011, **23**, 1810–28 (see p. 64).

(97) G. Li, R. Zhu, and Y. Yang, "Polymer solar cells", *Nat. Photonics*, 2012, **6**, 153–161 (see p. 64).

(98) J. Peet, J. Y. Kim, N. E. Coates, W. L. Ma, D. Moses, A. J. Heeger, and G. C. Bazan, "Efficiency enhancement in low-bandgap polymer solar cells by processing with alkane dithiols." *Nat. Mater.*, 2007, **6**, 497–500 (see p. 64).

(99) J. C. Hummelen, B. W. Knight, F. LePeq, F. Wudl, J. Yao, and C. L. Wilkins, "Preparation and Characterization of Fulleroid and Methanofullerene Derivatives", *J. Org. Chem.*, 1995, **60**, 532–538 (see p. 64).

(100) H. Hoppe and N. S. Sariciftci, "Morphology of polymer/fullerene bulk heterojunction solar cells", *J. Mater. Chem.*, 2006, **16**, 45 (see pp. 64, 167).

(101) X. Yang and J. Loos, "Toward High-Performance Polymer Solar Cells: The Importance of Morphology Control", *Macromolecules*, 2007, **40**, 1353–1362 (see p. 64).

(102) M. A. Ruderer and P. Müller-Buschbaum, "Morphology of polymer-based bulk heterojunction films for organic photovoltaics", *Soft Matter*, 2011, **7**, 5482 (see p. 64).

(103) R. M. Beal, A. Stavrinadis, J. H. Warner, J. M. Smith, H. E. Assender, and A. A. R. Watt, "The Molecular Structure of Polymer-Fullerene Composite Solar Cells and Its Influence on Device Performance", *Macromolecules*, 2010, **43**, 2343–2348 (see p. 64).

(104) J. H. Choi, T. Honda, S. Seki, and S. Fukuzumi, "Relationship between crystal packing and high electron mobility in the single crystal of thienyl-substituted methanofullerene." *Chem. Commun.*, 2011, **47**, 11213–5 (see p. 64).

(105) J. Nápoles-Duarte, M. Reyes-Reyes, J. Ricardo-Chavez, R. Garibay-Alonso, and R. López-Sandoval, "Effect of packing on the cohesive and electronic properties of methanofullerene crystals", *Phys. Rev. B*, 2008, **78**, 035425 (see pp. 65, 67).

(106) D. L. Cheung and A. Troisi, "Theoretical Study of the Organic Photovoltaic Electron Acceptor PCBM: Morphology, Electronic Structure, and Charge Localization", *J. Phys. Chem. C*, 2010, **114**, 20479–20488 (see p. 65).

(107) R. C. I. Mackenzie, J. M. Frost, and J. Nelson, "A numerical study of mobility in thin films of fullerene derivatives." *J. Chem. Phys.*, 2010, **132**, 064904 (see p. 65).

(108) M. T. Rispens, A. Meetsma, R. Rittberger, C. J. Brabec, N. S. Sariciftci, and J. C. Hummelen, "Influence of the solvent on the crystal structure of PCBM and the efficiency of MDMO-PPV:PCBM 'plastic' solar cells", *Chem. Commun.*, 2003, 2116–2118 (see p. 65).

(109) X. Yang, J. K. J. van Duren, M. T. Rispens, J. C. Hummelen, R. A. J. Janssen, M. A. J. Michels, and J. Loos, "Crystalline Organization of a Methanofullerene as Used for Plastic Solar-Cell Applications", *Adv. Mater.*, 2004, **16**, 802–806 (see p. 65).

(110) L. Zheng, J. Liu, Y. Ding, and Y. Han, "Morphology evolution and structural transformation of solution-processed methanofullerene thin film under thermal annealing." *J. Phys. Chem. B*, 2011, **115**, 8071–7 (see p. 65).

(111) L. Zheng and Y. Han, "Solvated crystals based on [6,6]-phenyl-C61-butyric acid methyl ester (PCBM) with the hexagonal structure and their phase transformation." *J. Phys. Chem. B*, 2012, **116**, 1598–604 (see pp. 65, 67).

(112) D. L. Dorset and M. P. McCourt, "Disorder and the molecular packing of C 60 buckminsterfullerene: a direct electron-crystallographic analysis", *Acta Crystallogr. Sect. A*, 1994, **50**, 344–351 (see p. 65).

(113) G. Van Tendeloo, C. Van Heurck, J. Van Landuyt, S. Amelinckx, M. A. Verheijen, P. H. M. Van Loosdrecht, and G. Meijer, "Phase transitions in fullerene (C60) and the related microstructure: a study by electron diffraction and electron microscopy", *J. Phys. Chem.*, 1992, **96**, 7424–7430 (see p. 65).

(114) C. Elschner, A. A. Levin, L. Wilde, J. Grenzer, C. Schroer, K. Leo, and M. Riede, "Determining the C60 molecular arrangement in thin films by means of X-ray diffraction", *J. Appl. Crystallogr.*, 2011, **44**, 983–990 (see p. 65).

(115) T. Morita, W. Takashima, and K. Kaneto, "Characteristics of Field Effect Transistors based on Fullerene Derivatives", *Jpn. J. Appl. Phys.*, 2007, **46**, L256–L258 (see p. 66).

(116) L. Zheng, Q. Zhou, X. Deng, M. Yuan, G. Yu, and Y. Cao, "Methanofullerenes Used as Electron Acceptors in Polymer Photovoltaic Devices", *J. Phys. Chem. B*, 2004, **108**, 11921–11926 (see p. 66).

(117) Q. Zhu, D. E. Cox, J. E. Fischer, K. Kniaz, A. R. McGhie, and O. Zhou, "Intercalation of solid C60 with iodine", *Nature*, 1992, **355**, 712–714 (see p. 67).

(118) J. Zhang, S. Sides, and F. S. Bates, "Ordering of Sphere Forming SISO Tetrablock Terpolymers on a Simple Hexagonal Lattice", *Macromolecules*, 2012, **45**, 256–265 (see p. 67).

(119) M. L. Fornasini, P. Manfrinetti, and D. Mazzone, "Yb-Zn-Al ternary system: CaCu5-type derived compounds in the zinc-rich corner", *J. Solid State Chem.*, 2006, **179**, 2012–2019 (see p. 67).

(120) Y. Liang, Y. Wu, D. Feng, S.-T. Tsai, H.-J. Son, G. Li, and L. Yu, "Development of New Semiconducting Polymers for High Performance Solar Cells", *J. Am. Chem. Soc.*, 2009, **131**, 56–57 (see pp. 74, 167, 175).

(121) Y. Liang, Z. Xu, J. Xia, S.-T. Tsai, Y. Wu, G. Li, C. Ray, and L. Yu, "For the Bright Future-Bulk Heterojunction Polymer Solar Cells with Power Conversion Efficiency of 7.4%", *Adv. Mater.*, 2010, **22**, E135–E138 (see pp. 74, 167, 175).

(122) C. J. Brabec, N. S. Sariciftci, and J. C. Hummelen, "Plastic Solar Cells", *Adv. Funct. Mater.*, 2001, **11**, 15–26 (see p. 74).

(123) G. Dennler, M. C. Scharber, and C. J. Brabec, "Polymer-Fullerene Bulk-Heterojunction Solar Cells", *Adv. Mater.*, 2009, **21**, 1323–1338 (see p. 74).

(124) J. E. Anthony, M. Heeney, and B. S. Ong, "Synthetic Aspects of Organic Semiconductors", *MRS Bull.*, 2008, **33**, 698–705 (see p. 74).

(125) Y.-J. Cheng, S.-H. Yang, and C.-S. Hsu, "Synthesis of Conjugated Polymers for Organic Solar Cell Applications", *Chem. Rev.*, 2009, **109**, 5868–5923 (see p. 74).

(126) G. Wei, R. R. Lunt, K. Sun, S. Wang, M. E. Thompson, and S. R. Forrest, "Efficient, ordered bulk heterojunction nanocrystalline solar cells by annealing of ultrathin squaraine thin films." *Nano Lett.*, 2010, **10**, 3555–9 (see p. 75).

(127) M. Singh, H. M. Haverinen, P. Dhagat, and G. E. Jabbour, "Inkjet Printing-Process and Its Applications", *Adv. Mater.*, 2010, **22**, 673–685 (see p. 75).

(128) Y.-H. Chang, S.-R. Tseng, C.-Y. Chen, H.-F. Meng, E.-C. Chen, S.-F. Horng, and C.-S. Hsu, "Polymer solar cell by blade coating", *Org. Electron.*, 2009, **10**, 741–746 (see p. 75).

(129) C. J. Brabec and J. R. Durrant, "Solution-Processed Organic Solar Cells", *MRS Bull.*, 2008, **33**, 670–675 (see p. 75).

(130) F. C. Krebs, "Fabrication and processing of polymer solar cells: A review of printing and coating techniques", *Sol. Energy Mater. Sol. Cells*, 2009, **93**, 394–412 (see pp. 75, 77).

(131) X. Chen, Z. Shen, and Y. Zhang, "New catalytic systems for the fixation of carbon dioxide. 1. Copolymerization of carbon dioxide and propylene oxide with new rare-earth catalysts-RE(P204)3-Al(i-Bu)3-R(OH)n", *Macromolecules*, 1991, **24**, 5305–5308 (see p. 77).

(132) J. L. Hedrick, T. Magbitang, E. F. Connor, T. Glauser, W. Volksen, C. J. Hawker, V. Y. Lee, and R. D. Miller, "Application of complex macromolecular architectures for advanced microelectronic materials." *Chem. - A Eur. J.*, 2002, **8**, 3308–19 (see p. 77).

(133) T. Rajagopalan, B. Lahlouh, J. A. Lubguban, N. Biswas, S. Gangopadhyay, J. Sun, D. H. Huang, S. L. Simon, A. Mallikarjunan, H.-C. Kim, W. Volksen, M. F. Toney, E. Huang, P. M. Rice, E. Delenia, and R. D. Miller, "Supercritical carbon dioxide extraction of porogens for the preparation of ultralow-dielectric-constant films", *Appl. Phys. Lett.*, 2003, **82**, 4328 (see p. 77).

(134) B.-J. de Gans, P. C. Duineveld, and U. S. Schubert, "Inkjet Printing of Polymers: State of the Art and Future Developments", *Adv. Mater.*, 2004, **16**, 203–213 (see p. 77).

(135) J. Perelaer, P. J. Smith, M. M. P. Wijnen, E. van den Bosch, R. Eckardt, P. H. J. M. Ketelaars, and U. S. Schubert, "Droplet Tailoring Using Evaporative Inkjet Printing", *Macromol. Chem. Phys.*, 2009, **210**, 387–393 (see p. 77).

(136) R. A. Street, M. Schoendorf, A. Roy, and J. H. Lee, "Interface state recombination in organic solar cells", *Phys. Rev. B*, 2010, **81**, 205307 (see p. 85).

(137) I. R. Gould, D. Noukakis, L. Gomez-Jahn, R. H. Young, J. L. Goodman, and S. Farid, "Radiative and nonradiative electron transfer in contact radical-ion pairs", *Chem. Phys.*, 1993, **176**, 439–456 (see p. 100).

(138) K. Vandewal, K. Tvingstedt, A. Gadisa, O. Inganäs, and J. V. Manca, "Relating the open-circuit voltage to interface molecular properties of donor:acceptor bulk heterojunction solar cells", *Phys. Rev. B*, 2010, **81**, 1–8 (see pp. 100, 101, 120, 122–124).

(139) K. Vandewal, K. Tvingstedt, A. Gadisa, O. Inganäs, and J. V. Manca, "On the origin of the open-circuit voltage of polymer-fullerene solar cells." *Nat. Mater.*, 2009, **8**, 904–9 (see p. 100).

(140) K. Vandewal, Z. Ma, J. Bergqvist, Z. Tang, E. Wang, P. Henriksson, K. Tvingstedt, M. R. Andersson, F. Zhang, and O. Inganäs, "Quantification of Quantum Efficiency and Energy Losses in Low Bandgap Polymer:Fullerene Solar Cells with High Open-Circuit Voltage", *Adv. Funct. Mater.*, 2012, **22**, 3480–3490 (see p. 100).

(141) R. A. Street, K. W. Song, J. E. Northrup, and S. Cowan, "Photoconductivity measurements of the electronic structure of organic solar cells", *Phys. Rev. B*, 2011, **83**, 165207 (see pp. 101, 103, 119, 124).

(142) M. Presselt, M. Bärenklau, R. Rösch, W. J. D. Beenken, E. Runge, S. Shokhovets, H. Hoppe, and G. Gobsch, "Subbandgap absorption in polymer-fullerene solar cells", *Appl. Phys. Lett.*, 2010, **97**, 253302 (see pp. 101, 114, 121).

(143) C. D. Liman, S. Choi, D. W. Breiby, J. E. Cochran, M. F. Toney, E. J. Kramer, and M. L. Chabinyc, "Two-Dimensional GIWAXS Reveals a Transient Crystal Phase in Solution-Processed Thermally Converted Tetrabenzoporphyrin", *J. Phys. Chem. B*, 2013, **117**, 14557–14567 (see pp. 103, 114).

(144) J. Ilavsky, "Nika : software for two-dimensional data reduction", *J. Appl. Crystallogr.*, 2012, **45**, 324–328 (see p. 105).

(145) R. A. Street, A. Krakaris, and S. R. Cowan, "Recombination Through Different Types of Localized States in Organic Solar Cells", *Adv. Funct. Mater.*, 2012, n/a–n/a (see p. 112).

(146) K. Vandewal, S. Albrecht, E. T. Hoke, K. R. Graham, J. Widmer, J. D. Douglas, M. Schubert, W. R. Mateker, J. T. Bloking, G. F. Burkhard, A. Sellinger, J. M. J. Fréchet, A. Amassian, M. K. Riede, M. D. McGehee, D. Neher, and A. Salleo, "Efficient charge generation by relaxed charge-transfer states at organic interfaces." *Nat. Mater.*, 2013, **12**, 1–6 (see pp. 119, 126).

(147) K. Vandewal, A. Gadisa, W. D. Oosterbaan, S. Bertho, F. Banishoeib, I. Van Severen, L. Lutsen, T. J. Cleij, D. Vanderzande, and J. V. Manca, "The Relation Between Open-Circuit Voltage and the Onset of Photocurrent Generation by Charge-Transfer Absorption in Polymer : Fullerene Bulk Heterojunction Solar Cells", *Adv. Funct. Mater.*, 2008, **18**, 2064–2070 (see p. 122).

(148) N. D. Eisenmenger, G. M. Su, G. C. Welch, C. J. Takacs, G. C. Bazan, E. J. Kramer, and M. L. Chabinyc, "Effect of Bridging Atom Identity on the Morphological Behavior of Solution-Processed Small Molecule Bulk Heterojunction Photovoltaics", *Chem. Mater.*, 2013, **25**, 1688–1698 (see p. 124).

(149) S.-H. Choi, C. D. Liman, S. Krämer, M. L. Chabinyc, and E. J. Kramer, "Crystalline polymorphs of [6,6]-phenyl-C61-butyric acid n-butyl ester (PCBNB)", *J. Phys. Chem. B*, 2012, **116**, 13568–13574 (see p. 126).

(150) R. C. Hilborn, "Einstein coefficients, cross sections, f values, dipole moments, and all that", *Am. J. Phys.*, 1982, **50**, 982 (see p. 127).

(151) P. Yu, M. C. Beard, R. J. Ellingson, S. Ferrere, C. Curtis, J. Drexler, F. Luiszer, and A. J. Nozik, "Absorption cross-section and related optical properties of colloidal InAs quantum dots." *J. Phys. Chem. B*, 2005, **109**, 7084–7 (see p. 127).

(152) C. R. Gochanour, H. C. Andersen, and M. D. Fayer, "Electronic excited state transport in solution", *J. Chem. Phys.*, 1979, **70**, 4254 (see p. 133).

(153) H. Tamura and Y. Matsuo, "Exciton diffusion length and charge mobility in donor and acceptor materials in organic photovoltaics: Tetrabenzoporphyrin and silylmethyl[60] fullerene", *Chem. Phys. Lett.*, 2014, **598**, 81–85 (see p. 134).

(154) S. Hullavarad, N. Hullavarad, D. Look, and B. Claflin, "Persistent Photoconductivity Studies in Nanostructured ZnO UV Sensors." *Nanoscale Res. Lett.*, 2009, **4**, 1421–7 (see pp. 140, 141).

(155) K. Liu, M. Sakurai, and M. Aono, "ZnO-based ultraviolet photodetectors." *Sensors*, 2010, **10**, 8604–34 (see pp. 140, 154).

(156) W. Yan, N. Mechau, H. Hahn, and R. Krupke, "Ultraviolet photodetector arrays assembled by dielectrophoresis of ZnO nanoparticles." *Nanotechnology*, 2010, **21**, 115501 (see p. 140).

(157) A. Puetz, F. Steiner, J. Mescher, M. Reinhard, N. Christ, D. Kutsarov, H. Kalt, U. Lemmer, and A. Colsmann, "Solution processable, precursor based zinc oxide buffer layers for 4.5% efficient organic tandem solar cells", *Org. Electron.*, 2012, **13**, 2696–2701 (see p. 140).

(158) S. O'Brien, M. G. Nolan, M. Çopuroglu, J. A. Hamilton, I. Povey, L. Pereira, R. Martins, E. Fortunato, and M. Pemble, "Zinc oxide thin films: Characterization and potential applications", *Thin Solid Films*, 2010, **518**, 4515–4519 (see pp. 140, 142).

(159) C. Busch, R. Theissmann, S. Bubel, G. Schierning, and R. Schmechel, "Influence of the annealing atmosphere on solution based zinc oxide thin film transistors", *MRS Proc.*, 2011, **1359**, pages (see pp. 140–142).

(160) R. Theissmann, S. Bubel, M. Sanlialp, C. Busch, G. Schierning, and R. Schmechel, "High performance low temperature solution-processed zinc oxide thin film transistor", *Thin Solid Films*, 2011, **519**, 5623–5628 (see pp. 140, 142, 143).

(161) Y.-H. Lin, H. Faber, K. Zhao, Q. Wang, A. Amassian, M. McLachlan, and T. D. Anthopoulos, "High-Performance ZnO Transistors Processed Via an Aqueous Carbon-Free Metal Oxide Precursor Route at Temperatures Between 80-180 °C." *Adv. Mater.*, 2013, **25**, 4340–6 (see pp. 140–142).

(162) S. Walther, S. Schäfer, M. Jank, H. Thiem, W. Peukert, L. Frey, and H. Ryssel, "Influence of annealing temperature and measurement ambient on TFTs based on gas phase synthesized ZnO nanoparticles", *Microelectron. Eng.*, 2010, **87**, 2312–2316 (see p. 140).

(163) S. Bubel and R. Schmechel, "Mechanical layer compaction for dispersion processed nanoparticulate zinc oxide thin film transistors", *Microelectron. Eng.*, 2012, **96**, 36–39 (see p. 140).

(164) Y.-H. Lin, H. Faber, S. Rossbauer, and T. D. Anthopoulos, "Solution-processed ZnO nanoparticle-based transistors via a room-temperature photochemical conversion process", *Appl. Phys. Lett.*, 2013, **102**, 193516 (see pp. 140, 141).

(165) J. I. Sohn, W.-K. Hong, M. J. Lee, T. Lee, H. Sirringhaus, D. J. Kang, and M. E. Welland, "The influence of surface chemical dynamics on electrical and optical properties of ZnO nanowire field effect transistors." *Nanotechnology*, 2009, **20**, 505202 (see p. 140).

(166) F. Chaabouni, M. Abaab, and B. Rezig, "Metrological characteristics of ZNO oxygen sensor at room temperature", *Sensors Actuators B Chem.*, 2004, **100**, 200–204 (see p. 140).

(167) S.-W. Fan, A. K. Srivastava, and V. P. Dravid, "UV-activated room-temperature gas sensing mechanism of polycrystalline ZnO", *Appl. Phys. Lett.*, 2009, **95**, 142106 (see pp. 140, 141).

(168) M. S. White, D. C. Olson, S. E. Shaheen, N. Kopidakis, and D. S. Ginley, "Inverted bulk-heterojunction organic photovoltaic device using a solution-derived ZnO underlayer", *Appl. Phys. Lett.*, 2006, **89**, 143517–3 (see p. 141).

(169) C.-H. Hsieh, Y.-J. Cheng, P.-J. Li, C.-H. Chen, M. Dubosc, R.-M. Liang, and C.-S. Hsu, "Highly efficient and stable inverted polymer solar cells integrated with a cross-linked fullerene material as an interlayer." *J. Am. Chem. Soc.*, 2010, **132**, 4887–93 (see p. 141).

(170) A. Manor, E. A. Katz, T. Tromholt, and F. C. Krebs, "Electrical and Photo-Induced Degradation of ZnO Layers in Organic Photovoltaics", *Adv. Energy Mater.*, 2011, **1**, 836–843 (see p. 141).

(171) A. Manor, E. A. Katz, T. Tromholt, and F. C. Krebs, "Enhancing functionality of ZnO hole blocking layer in organic photovoltaics", *Sol. Energy Mater. Sol. Cells*, 2012, **98**, 491–493 (see p. 141).

(172) T. Kuwabara, T. Nakashima, T. Yamaguchi, and K. Takahashi, "Flexible inverted polymer solar cells on polyethylene terephthalate substrate containing zinc oxide electron-collection-layer prepared by novel sol-gel method and low-temperature treatments", *Org. Electron.*, 2012, **13**, 1136–1140 (see p. 141).

(173) J. Bao, I. Shalish, Z. Su, R. Gurwitz, F. Capasso, X. Wang, and Z. Ren, "Photoinduced oxygen release and persistent photoconductivity in ZnO nanowires." *Nanoscale Res. Lett.*, 2011, **6**, 404 (see p. 141).

(174) Y. Shapira, S. Cox, and D. Lichtman, "Chemisorption, photodesorption and conductivity measurements on ZnO surfaces", *Surf. Sci.*, 1976, **54**, 43–59 (see p. 141).

(175) S. Lany and A. Zunger, "Anion vacancies as a source of persistent photoconductivity in II-VI and chalcopyrite semiconductors", *Phys. Rev. B*, 2005, **72**, 035215 (see p. 141).

(176) C. G. Van de Walle, "Hydrogen as a Cause of Doping in Zinc Oxide", *Phys. Rev. Lett.*, 2000, **85**, 1012–1015 (see pp. 141, 151).

(177) M.-H. Du and K. Biswas, "Anionic and Hidden Hydrogen in ZnO", *Phys. Rev. Lett.*, 2011, **106**, 115502 (see p. 141).

(178) Y. K. Su, S. M. Peng, L. W. Ji, C. Z. Wu, W. B. Cheng, and C. H. Liu, "Ultraviolet ZnO nanorod photosensors." *Langmuir*, 2010, **26**, 603–6 (see pp. 142, 158).

(179) S. Bubel and M. L. Chabinyc, "Model for determination of mid-gap states in amorphous metal oxides from thin film transistors", *J. Appl. Phys.*, 2013, **113**, 234507 (see pp. 142, 160).

(180) S. Bubel, S. Meyer, F. Kunze, and M. L. Chabinyc, "Ionic Liquid Gating Reveals Trap-Filled Limit Mobility in Low Temperature Amorphous Zinc Oxide", 2013 (see p. 142).

(181) S. Bubel, S. Meyer, and M. L. Chabinyc, "Reliability of Ionic Liquid Gated Metal Oxides and Gold Leaching", *IEEE T. Device. Mat. Re.*, 2013 (see p. 143).

(182) S. Sze and K. Ng, *Physics of semiconductor devices*, Wiley, 2006 (see p. 145).

(183) E. H. Nicollian, M. H. Hanes, and J. R. Brews, "Using the MIS capacitor for doping profile measurements with minimal interface state error", *IEEE Trans. Electron Devices*, 1973, **20**, 380–389 (see p. 147).

(184) P. Erhart and K. Albe, "Diffusion of zinc vacancies and interstitials in zinc oxide", *Appl. Phys. Lett.*, 2006, **88**, 201918 (see p. 151).

(185) M. Burkhardt, W. Liu, C. G. Shuttle, K. Banerjee, and M. L. Chabinyc, "Top illuminated inverted organic ultraviolet photosensors with single layer graphene electrodes", *Appl. Phys. Lett.*, 2012, **101**, 033302 (see pp. 153, 154).

(186) X. Gong, M. Tong, Y. Xia, W. Cai, J. S. Moon, Y. Cao, G. Yu, C.-L. Shieh, B. Nilsson, and A. J. Heeger, "High-detectivity polymer photodetectors with spectral response from 300 nm to 1450 nm." *Science (80-.).*, 2009, **325**, 1665–7 (see p. 154).

(187) K. Liu, J. Ma, J. Zhang, Y. Lu, D. Jiang, B. Li, D. Zhao, Z. Zhang, B. Yao, and D. Shen, "Ultraviolet photoconductive detector with high visible rejection and fast photoresponse based on ZnO thin film", *Solid. State. Electron.*, 2007, **51**, 757–761 (see p. 157).

(188) J. Reemts and A. Kittel, "Persistent photoconductivity in highly porous ZnO films", *J. Appl. Phys.*, 2007, **101**, 013709 (see p. 158).

(189) R. A. Street, T. N. Ng, R. A. Lujan, I. Son, M. Smith, S. Kim, T. Lee, Y. Moon, and S. Cho, "Sol-Gel Solution-Deposited InGaZnO Thin Film Transistors." *ACS Appl. Mater. Interfaces*, 2014, **6**, 4428–37 (see p. 160).

(190) S. Bubel, N. Mechau, and R. Schmechel, "Electronic properties of polyvinylpyrrolidone at the zinc oxide nanoparticle surface", *J. Mater. Sci.*, 2011, **46**, 7776–7783 (see p. 160).

(191) S. van Bavel, E. Sourty, G. de With, K. Frolic, and J. Loos, "Relation between Photoactive Layer Thickness, 3D Morphology, and Device Performance in P3HT/PCBM Bulk-Heterojunction Solar Cells", *Macromolecules*, 2009, **42**, 7396–7403 (see p. 167).

(192) S. E. Shaheen, C. J. Brabec, N. S. Sariciftci, F. Padinger, T. Fromherz, and J. C. Hummelen, "2.5% efficient organic plastic solar cells", *Appl. Phys. Lett.*, 2001, **78**, 841–843 (see p. 167).

(193) C. Kitamura, S. Tanaka, and Y. Yamashita, "Design of Narrow-Bandgap Polymers. Syntheses and Properties of Monomers and Polymers Containing Aromatic-Donor and o -Quinoid-Acceptor Units", *Chem. Mater.*, 1996, **8**, 570–578 (see p. 167).

(194) J.-L. Bredas, "Relationship Between Band-Gap and Bond Length Alternation in Organic Conjugated Polymers", *J. Chem. Phys.*, 1985, **82**, 3808–3811 (see p. 167).

(195) F. Wudl, M. Kobayashi, and A. J. Heeger, "Poly(isothianaphthene)", *J. Org. Chem.*, 1984, **49**, 3382–3384 (see p. 167).

(196) M. Pomerantz, B. Chaloner-Gill, L. O. Harding, J. J. Tseng, and W. J. Pomerantz, "Poly(2,3-dihexylthieno[3,4-b]pyrazine). A new processable low band-gap polyheterocycle", *J. Chem. Soc. Chem. Commun.*, 1992, 1672 (see p. 167).

(197) J. Hou, H.-Y. Chen, S. Zhang, R. I. Chen, Y. Yang, Y. Wu, and G. Li, "Synthesis of a low band gap polymer and its application in highly efficient polymer solar cells." *J. Am. Chem. Soc.*, 2009, **131**, 15586–7 (see pp. 167, 175).

(198) T.-Y. Chu, J. Lu, S. Beaupré, Y. Zhang, J.-R. Pouliot, S. Wakim, J. Zhou, M. Leclerc, Z. Li, J. Ding, and Y. Tao, "Bulk Heterojunction Solar Cells Using Thieno[3,4-c]pyrrole-4,6-dione and Dithieno[3,2-b:2',3'-d]silole Copolymer with a Power Conversion Efficiency of 7.3%", *J. Am. Chem. Soc.*, 2011, **133**, 4250–4253 (see pp. 167, 175).

(199) T. Okamoto, K. Kudoh, A. Wakamiya, and S. Yamaguchi, "General synthesis of extended fused oligothiophenes consisting of an even number of thiophene rings." *Chem. - A Eur. J.*, 2007, **13**, 548–56 (see p. 168).

(200) X.-C. Li, H. Sirringhaus, F. Garnier, A. B. Holmes, S. C. Moratti, N. Feeder, W. Clegg, S. J. Teat, and R. H. Friend, "A Highly π-Stacked Organic Semiconductor for Thin Film Transistors Based on Fused Thiophenes", *J. Am. Chem. Soc.*, 1998, **120**, 2206–2207 (see p. 168).

(201) M. He and F. Zhang, "Synthesis and structure of alkyl-substituted fused thiophenes containing up to seven rings." *J. Org. Chem.*, 2007, **72**, 442–51 (see pp. 168, 169).

(202) J. Li, H.-S. Tan, Z.-K. Chen, W.-P. Goh, H.-K. Wong, K.-H. Ong, W. Liu, C. M. Li, and B. S. Ong, "Dialkyl-Substituted Dithienothiophene Copolymers as Polymer Semiconductors for Thin-Film Transistors and Bulk Heterojunction Solar Cells", *Macromolecules*, 2011, **44**, 690–693 (see pp. 168, 169).

(203) M. Helgesen, S. A. Gevorgyan, F. C. Krebs, and R. A. J. Janssen, "Substituted 2,1,3-Benzothiadiazole- And Thiophene-Based Polymers for Solar Cells - Introducing a New Thermocleavable Precursor", *Chem. Mater.*, 2009, **21**, 4669–4675 (see p. 168).

(204) Y. Li, H. Li, B. Xu, Z. Li, F. Chen, D. Feng, J. Zhang, and W. Tian, "Molecular structure-property engineering for photovoltaic applications: Fluorene-acceptor alternating conjugated copolymers with varied bridged moieties", *Polymer (Guildf).*, 2010, **51**, 1786–1795 (see p. 168).

(205) C. H. Woo, P. M. Beaujuge, T. W. Holcombe, O. P. Lee, and J. M. J. Fréchet, "Incorporation of Furan into Low Band-Gap Polymers for Efficient Solar Cells", *J. Am. Chem. Soc.*, 2010, **132**, 15547–15549 (see p. 168).

(206) S. Zhang, Y. Guo, H. Fan, Y. Liu, H.-Y. Chen, G. Yang, X. Zhan, Y. Liu, Y. Li, and Y. Yang, "Low bandgap π-conjugated copolymers based on fused thiophenes and benzothiadiazole: Synthesis and structure-property relationship study", *J. Polym. Sci. Part A Polym. Chem.*, 2009, **47**, 5498–5508 (see p. 170).

(207) A. V. Patil, W.-H. Lee, E. Lee, K. Kim, I.-N. Kang, and S.-H. Lee, "Synthesis and Photovoltaic Properties of a Low-Band-Gap Copolymer of Dithieno[3,2- b :2',3'-d]thiophene and Dithienylquinoxaline", *Macromolecules*, 2011, **44**, 1238–1241 (see p. 170).

(208) J. Hwang, E.-G. Kim, J. Liu, J.-L. Brédas, A. Duggal, and A. Kahn, "Photoelectron Spectroscopic Study of the Electronic Band Structure of Polyfluorene and Fluorene-Arylamine Copolymers at Interfaces", *J. Phys. Chem. C*, 2007, **111**, 1378–1384 (see p. 172).

(209) G. Jo, S.-I. Na, S.-H. Oh, S. Lee, T.-S. Kim, G. Wang, M. Choe, W. Park, J. Yoon, D.-Y. Kim, Y. H. Kahng, and T. Lee, "Tuning of a graphene-electrode work function to enhance the efficiency of organic bulk heterojunction photovoltaic cells with an inverted structure", *Appl. Phys. Lett.*, 2010, **97**, 213301 (see p. 175).

(210) U. Zhokhavets, T. Erb, G. Gobsch, M. Al-Ibrahim, and O. Ambacher, "Relation between absorption and crystallinity of poly(3-hexylthiophene)/fullerene films for plastic solar cells", *Chem. Phys. Lett.*, 2006, **418**, 347–350 (see pp. 176, 177).

(211) J. C. Duda, P. E. Hopkins, Y. Shen, and M. C. Gupta, "Exceptionally Low Thermal Conductivities of Films of the Fullerene Derivative PCBM", *Phys. Rev. Lett.*, 2013, **110**, 015902 (see p. 188).